Technische Universität Dresden

Design of a Dual Band Local Positioning System

Niko Joram

der Fakultät Elektrotechnik und Informationstechnik
der Technischen Universität Dresden
zur Erlangung des akademischen Grades

Doktoringenieur
(Dr.-Ing.)

genehmigte Dissertation

Vorsitzender:	Prof. Dr. techn. Klaus Janschek
Gutachter:	Prof. Dr. sc. techn. Frank Ellinger
	Prof. Dr. sc. techn. Jan Hesselbarth

Tag der Einreichung:	30. Januar 2015
Tag der Verteidigung:	11. September 2015

Danksagung

An dieser Stelle möchte ich mich bei allen Personen bedanken, die diese Arbeit in den letzten Jahren unterstützt haben.

Mein besonderer Dank gilt Prof. Dr. sc. techn. Frank Ellinger, der mich zur Arbeit auf dem Gebiet der integrierten Hochfrequenzschaltungen motiviert hat und es mir ermöglicht hat, meine Dissertation an seinem Lehrstuhl zu bearbeiten.

Sehr verbunden bin ich meinen Mitstreitern Jens Wagner und Belal Al-Qudsi, die sich stets Zeit für umfangreiche Fachdiskussionen genommen haben und mich bei allen wissenschaftlichen, technischen und administrativen Belangen im Projekt unschätzbar unterstützt haben.

Markus Schulz, Elena Sobotta, Axel Strobel und Robert Wolf, meinen Kollegen im Büro, sowie Bastian Lindner, Anja Muthmann, Stefan Schumann und Uwe Mayer danke ich für das kreative Arbeitsklima und die vielen aufschlussreichen fachlichen und privaten Gespräche.

Ich danke Tom Drechsel, Mohammed El-Shennawy, Marco Gunia und Prof. Dr. Udo Jörges für die aufmerksame Durchsicht der Arbeit und die hilfreichen Kommentare und Diskussionen, die zur Verbesserung des Manuskripts beigetragen haben.

Der Gemeinde Eichigt im Vogtland danke ich für die unkomplizierte Bereitstellung der Messszenarien für das Positionierungssystem.

Von Herzen danke ich meinen Eltern, die mich immer unterstützt haben.

Zusammenfassung

Die vorliegende Arbeit befasst sich mit dem Entwurf eines robusten lokalen Positionierungssystems (LPS), welches in den lizenzfreien Frequenzbereichen für industrielle, wissenschaftliche und medizinische Zwecke (*industrial, scientific, medical*, ISM) bei 2,4 GHz und 5,8 GHz arbeitet. Die Positionsbestimmung beruht auf dem Prinzip des frequenzmodulierten Dauerstrichradars (*frequency modulated continuous wave*, FMCW-Radar), welches hochfrequente Rampensignale für Laufzeitmessungen und damit Abstandsmessungen benutzt.

Im Gegensatz zu aktuellen Arbeiten auf diesem Gebiet benutzt das vorgestellte System Daten aus beiden Frequenzbändern zur Erhöhung der Genauigkeit und Präzision sowie Verbesserung der Robustheit. Ein Prototyp des kompletten Systems bestehend aus Basisstationen und mobilen Stationen wurde entworfen. Fast die gesamte analoge hochfrequente Signalverarbeitungskette wurde als anwendungsspezifische integrierte Schaltung realisiert. Verglichen mit Systemen aus Standardkomponenten erlaubt dieser Ansatz die Miniaturisierung der Systemkomponenten und die Einsparung von Leistung. Schlüsselkomponenten wurden mit Konzepten für mehrbandige oder breitbandige Schaltungen entworfen. Dabei wurden Sender und Empfänger bestehend aus rauscharmem Verstärker, Mischer und Frequenzsynthesizer mit breitbandiger Frequenzrampenfunktion implementiert. Außerdem wurde ein Leistungsverstärker für die gleichzeitige Nutzung der beiden definierten Frequenzbänder entworfen.

Um Spezifikationen für den Schaltungsentwurf zu erhalten, wurden in der Fachliteratur vernachlässigte Nichtidealitäten von FMCW-Radarsystemen modelliert. Dazu gehören Signalverzerrungen durch Kompression oder Intermodulation, der Einfluß der automatischen Verstärkungseinstellung sowie schmalbandige Störer und Nebenschwingungen. Die Ergebnisse der Modellierung wurden benutzt, um eine Spezifikation für den Schaltungsentwurf zu erhalten.

Die Schätzung der Position aus gemessenen Abständen wurde über eine erweiterte Version des Gittersuchalgorithmus erreicht. Dieser nutzt die Abstandsmessdaten aus beiden Frequenzbändern. Der Algorithmus ist so entworfen, dass er effizient in einem eingebetteten System implementiert werden kann.

Messungen zeigen eine maximale Reichweite des Systems von mindestens 245 m. Die Genauigkeit von Abstandsmessungen im Freiland beträgt 8,2 cm. Positionsmessungen wurden unter Verwendung beider Einzelbänder durchgeführt und mit den Ergebnissen des Zweiband-Gittersuchalgorithmus verglichen. Damit konnte eine starke Verbesserung der Positionsgenauigkeit erreicht werden. Die Genauig-

keit in einem Innenraum mit einer Grundfläche von 276 m^2 kann verbessert werden von 1,27 m bei 2,4 GHz und 1,86 m bei 5,8 GHz zu nur 0,38 m im Zweibandverfahren. Das entspricht einer Verbesserung um einen Faktor von mindestens 3,3. In einem größeren Außenszenario mit einer Fläche von 4,8 km^2 verbessert sich die Genauigkeit um einen Faktor von mindestens 2,8 von 1,88 m bei 2,4 GHz und 5,93 m bei 5,8 GHz auf 0,68 m bei Nutzung von Daten aus beiden Frequenzbändern.

Abstract

This work presents a robust dual band local positioning system (LPS) working in the 2.4 GHz and 5.8 GHz industrial science medical (ISM) bands. Position measurement is based on the frequency-modulated continuous wave (FMCW) radar approach, which uses radio frequency (RF) chirp signals for propagation time and therefore distance measurements.

Contrary to state of the art LPS, the presented system uses data from both bands to improve accuracy, precision and robustness. A complete system prototype is designed consisting of base stations and tags encapsulating most of the RF and analogue signal processing in custom integrated circuits. This design approach allows to reduce size and power consumption compared to a hybrid system using off-the-shelf components. Key components are implemented using concepts, which support operation in multiple frequency bands, namely, the receiver consisting of a low noise amplifier (LNA), mixer, frequency synthesizer with a wide band voltage-controlled oscillator (VCO) having broadband chirp generation capabilities and a dual band power amplifier.

System imperfections occurring in FMCW radar systems are modeled. Effects neglected in literature such as compression, intermodulation, the influence of automatic gain control, blockers and spurious emissions are modeled. The results are used to derive a specification set for the circuit design.

Position estimation from measured distances is done using an enhanced version of the grid search algorithm, which makes use of data from multiple frequency bands. The algorithm is designed to be easily and efficiently implemented in embedded systems.

Measurements show a coverage range of the system of at least 245 m. Ranging accuracy in an outdoor scenario can be as low as 8.2 cm. Comparative dual band position measurements prove an effective outlier filtering in indoor and outdoor scenarios compared to single band results, yielding in a large gain of accuracy. Positioning accuracy in an indoor scenario with an area of 276 m^2 can be improved from 1.27 m at 2.4 GHz and 1.86 m at 5.8 GHz to only 0.38 m in the dual band case, corresponding to an improvement by at least a factor of 3.3. In a large outdoor scenario of 4.8 km^2, accuracy improves from 1.88 m at 2.4 GHz and 5.93 m at 5.8 GHz to 0.68 m with dual band processing, which is a factor of at least 2.8.

Contents

1 Introduction

1.1 Motivation

Since the beginning of time people yearn to know their own locations. During the Middle Ages mariners used the stars as references for navigating their ships across the vastness of the oceans. Travelers oriented towards landmarks such as mountains or rivers to find their way home.

Shifting these scenes to modern times, it is observed that the scenarios did not change much. Where people in the past struggled to cross the primeval forests without getting lost, today they are equally fighting to get their bearings in the urban jungle to find the next restaurant or cash point. Moreover, the very principle of location finding, relating oneself to references, remains unchanged. The only minor difference is that mankind is now able to use artificial stars.

The satellite-based global positioning system (GPS) became operational in the 1990s. At first, accurate service was only available to the military. For civilian use, the signal was purposely degraded limiting the accuracy to around 100 m, making it unpractical for modern navigation purposes. In the year 2000, this selective availability was deactivated, paving the way for the widespread use of GPS in car and pedestrian navigation, reaching accuracies around 10 m.

A major drawback of GPS is the limited availability inside buildings due to the weak satellite signals. But with the increasing complexity of buildings with the most prominent example being airports and malls, there is also demand for indoor localization. The first widely available services also available indoors came up in the 1990s and were based on cellular networks with the granularity of a cell size ranging from less than 100 m in urban areas to some kilometers in rural areas [BFH+96]. With the emerging of ubiquitous wireless local area network (WLAN) coverage after the year 2000, signal strength-based localization approaches were introduced, increasing the accuracy to values around 10 m [DS03]. It has to be noted that most indoor systems also work outdoors, which allows to increase the accuracy of locations beyond that of GPS in certain areas with special infrastructure for localization. Modern solutions using special infrastructure can reach accuracies below 1 m [Ubi14, Zig14]. However, indoor environments are usually challenging, because the probability of non-line-of-sight conditions is high and radio frequency (RF) based localization systems suffer from multipath propagation and fading, decreasing the system performance. Contrary to that, the demand for accuracy is usually higher indoors, because areas are more confined.

To overcome these problems there is on-going research on using multiple data sources to enhance indoor localization performance. One approach is to chart WLAN access points in areas of public interest for location estimation, called finger printing. Since 2001, a large database is built containing locations of countless wireless access points [WiG14]. The *European Integration Project MAGELLAN* [MAG14] researches on seamless integration of indoor and outdoor localization techniques, such as GPS together with approaches based on signal strength or cellular networks. However, those approaches are usually based on existing fixed infrastructure with a large number of nodes.

Obtaining multiple data is also possible from the hardware side of existing localization devices. It was already demonstrated that adding hardware for the measurement of the angle of arrival of RF localization signals can greatly improve accuracy [Gie10]. Improvements in positioning performance were also shown by adding data from readily available inertial sensors such as accelerometers and gyroscopes [AQEJE14*].

This thesis presents the design of a local positioning system with another promising data source which is the use of information from multiple frequency bands. Free space and different obstacles such as various types of walls or windows attenuate and reflect RF signals in different frequency bands differently [ARUS+03]. Having a multi band system allows the selection of the data from the band with best signal quality. Another advantage, especially with today's crowded radio frequency bands, is the resilience towards interferers which can disturb the system in a certain band, but not in another. In a nutshell, redundancy is added to the system, which can improve the robustness in complex indoor environments and allows the use in security-sensitive applications.

1.2 Scope of Application

This work was done in the scope of an European integration project entitled *A holistic approach towards the development of the first responder of the future*, with the acronym E-SPONDER [VGC+10]. The goal of the E-SPONDER project is the development of technologies to provide first responders with information and communication support during large-scale crisis events.

There were several partners involved dealing with the different aspects of the holistic approach, such as

- *EXUS, Greece* was coordinating the project and provides back end software,
- *University of Modena e Reggio Emilia, Italy* deals with network structures for connection of the different parts of the E-SPONDER system,
- *CrisisPlan, Netherlands* is a end-user providing system specifications and a connection of the technical staff to the users,

- *CEREN, France* is another end-user,
- *PROSYST Software, Germany* develops the middle-ware between sensors and user application,
- *Immersion, France* contributes the 3D visualization of the first responder location in the command centers,
- *Rose Vision, Spain* wants to standardize the developed technologies and works on logistics of first responder operations,
- *National Technical University of Athens, Greece* implements the hardware for the network between the users of E-SPONDER,
- *CSEM, Switzerland* provides biomedical sensors and other hardware for the first responders,
- *Smartex, Italy* integrates developed hardware into the garment of first responders,
- *Technische Universität Dresden, Germany* develops a local positioning system to track all involved crisis personnel,
- *YellowMap, Germany* contributes maps and point of interest services for the location visualization,
- *Panou, Greece* is a security and telecommunications specialist, who develops the mobile operations center.

During crisis situations, one important aspect is to continuously track the movements of all involved emergency personnel like fire fighters, police men or paramedics at any time. Since the scenarios vary widely, ranging from airplane crashes, collapsing buildings during earthquakes to fires, satellite-based systems like GPS cannot always be used. Especially for tracking indoors or in complicated urban environments, a dedicated local positioning system (LPS) is necessary to cover vital areas.

The E-SPONDER system consists of three components: a remote emergency operations control center (EOC), on-site mobile emergency operations control centers (MEOCs) and first responder units (FRUs). All of the components are connected by a wireless incident area network to allow information propagation from the operation centers to the first responders and back. The LPS mobile station, which is to be tracked, is integrated into a wireless body area network at the FRU along with biomedical and environmental sensors. Furthermore, since the positioning system is local, several base stations (BS) need to be set up around the incident area to provide reference points. Fig. 1.1 shows how the LPS integrates into the E-SPONDER system.

There are several specifications, which the LPS needs to fulfill to be applicable in the described scenarios:

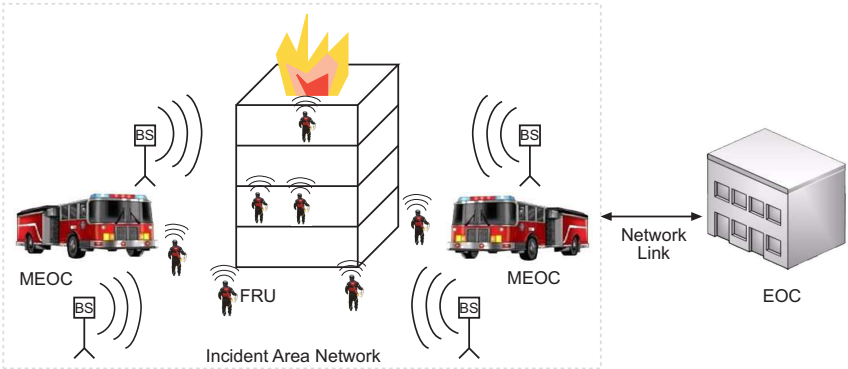

Figure 1.1: Overview of the LPS within the E-SPONDER system

- *3-D Localization:* For effective crisis management, it is necessary to know the altitude of a first responder, which may correspond to a story in a building.
- *Robustness:* Due to the diverse nature of crisis situations, the LPS has work under many different environmental conditions, while still having to provide reliable position information. Typically, multipath propagation can be expected.
- *Real-time Capability:* Movements have to be tracked without excessive delay. An update rate of less than one second is specified, which corresponds to the update rate of a standard GPS receiver.
- *Scalability:* The sizes of crisis events are variable. For managing a forest fire, it may be necessary to have several ten up to a hundred first responders on duty. The system performance must not be influenced by the number of mobile stations. As a consequence, the system has to use an approach similar to GPS, where the mobile stations determine their positions without having to transmit signals to the infrastructure. The propagation of the determined position is then done by the incident area network, which is not part of this thesis.
- *Coverage and Accuracy:* A range of at least $d_{0,\max} = 300\,\mathrm{m}$ with an accuracy of one meter is specified.
- *Deployable Infrastructure:* The LPS base stations have to be set up fast in the event of a crisis. They have to be completely wireless. The battery has to last for at least eight hours of continuous operation.
- *License-free Operation:* To comply with regulations, the system has to work

in a license-free industrial science medical (ISM) band. However, for operation during emergencies, permits, e.g. for increased output power, could be obtained.

1.3 Objectives and Structure

This work presents a structured approach for the design of local positioning systems using the frequency-modulated continuous wave (FMCW) principle. The key points of the investigation are as follows.

- *Theory:* Important effects, which can be observed in hardware implementations, like distortion, noise and interference are modeled and used to determine the parameters for the system components to fulfill the set specifications.
- *Design:* Methods for the design of all major components of a positioning system are presented. The designs are verified by integrated circuit implementations. The main focus lies on concepts, which are capable to support multi or broad band operation. A fully integrated transceiver chip including a complete multi-channel dual-band localization system testbed is developed, which combines all analogue building blocks and digital post-processing.
- *Verification:* Signal processing algorithms for synchronization and position estimation are developed and applied for the verification of the performance of the developed system using data from multiple frequency bands.

The focus of this thesis is on circuit and system design. It is not intended to provide a thorough discussion on signal processing and position estimation algorithms. However, since it is necessary for verification, state-of-the-art algorithms will be applied and referenced, but detailed only as much as necessary for the overall understanding.

The thesis is structured as follows. After presenting the scope of application in the current chapter, the fundamentals of localization systems are discussed in chapter 2, followed by a classification and market overview.

Chapter 3 is dedicated to the system theory of frequency-modulated continuous wave (FMCW)-based localization systems, providing a translation from system specifications to circuit specifications. Furthermore it describes a basic synchronization algorithm for two stations. Then, the implementation and verification of a test system is detailed, consisting of an analog front end with off-the-shelf components and a digital back end, which implements the synchronization algorithm. This chapter is concluded with an overview of the system specifications and derived circuit specifications.

In chapter 4, the design of integrated circuits and their assembly to a dual-band localization system, consisting of base stations and tags, is described in detail.

Major components and their design are presented including a low-noise amplifier, mixer, power amplifier and phase-locked loop.

Chapter 5 presents measurement results of the developed system in different scenarios. The thesis is concluded by a summary and an outlook to further areas of work to improve the system.

2 Fundamentals of Localization

2.1 System Classification

Localization is the process of determining the physical positions of targets with a specific degree of accuracy in indoor or outdoor environments [LT09]. Local positioning refers to localization within a confined area using local infrastructure, which is the LPS. There are several technologies used for localization:

- *Optical localization* is mainly applied in geographical surveys using total stations. It is based on light being sent out by a station and reflected at a target. The station evaluates the time of flight (ToF) and phase shift of the reflected signal to determine the distance. It allows very high accuracy with the drawbacks of expensive and bulky equipment as well as the inability to operate in non-line-of-sight environments.
- *Ultra sound based localization* uses sound signals with frequencies in the range of several ten kilohertz, also evaluating the ToF. The most popular application is the use in car parking sensors. The components are cheap and the system simple to implement. Because of the low propagation speed in the range of 340 m/s, accuracy of the distance measurement can be in the millimeter range. Major disadvantages are the low range, the inability of the signal to penetrate obstacles and the strong temperature dependency of the propagation speed.
- *Localization using inertial measurement units* has recently become popular because of cheap available accelerometers, gyroscopes and magnetometers implemented as microelectromechanical systems (MEMS). Inertial localization systems use a process known as dead reckoning. Based on a starting point, e.g. from a GPS measurement, the system tracks its location from this point using attitude and acceleration information [AQEJE14*]. Applications include aviation navigation but also personal navigation devices, where the systems are employed to bridge times, where the GPS signal is not available. However, accuracy is limited by accumulating errors.
- *Radio location systems* are another large class. There are ToF based systems which are also known as radars, but also approaches that relate the distance to a target to a received signal strength indicator (RSSI) or include the angle of arrival (AoA) of the signal in the location estimation process. Radio frequency signals can penetrate non-metallic obstacles and the influence of temperature, humidity or dust is negligible, which makes this class of

systems an excellent choice for robust localization. Disadvantageous is the limited accuracy resulting from the high propagation speed of approximately $3 \cdot 10^8$ m/s and the fact that radio channels suffer from multipath-induced fading.

The system developed in this thesis uses the radar approach because of its robustness and the good range. The measurement principle is based on the fact that electromagnetic waves travel at a certain propagation speed and the signal arrives at the target after the ToF, which is then related to the distance between the signal source and the target. There are two radar approaches, which are distinguished in literature: the primary or reflective radar and the secondary or one-way radar [KQ99].

- A typical implementation of a *reflective radar* is a transceiver station, which can transmit and receive signals at the same time. The radar target is usually passive and just reflects the signals sent out by the station. This type of radar is well known through its applications as a ship or aircraft radar. A main advantage of the reflective radar is the simple implementation in hardware, since there is only one transceiver and no active target. Major drawbacks include the high required antenna isolation between the transmit and receive paths and therefore the problem of crosstalk and also a limited range or high required transmit power, since the signal reflection from the passive target has to be strong enough to be detectable by the transceiver. Furthermore, without extra hardware effort (like in active reflector topologies [SE11]) there is no way to easily identify different targets.
- A *secondary or one-way radar system* consists of base stations and mobile stations. Depending on the signaling protocol, the mobile station needs to be a complete transceiver or a receiver only. In any case, signal processing in the radar target is necessary. A prominent example is the GPS, where the mobile station is a receiver only. A key advantage of the one-way system is the increased range with the same signal power compared to the reflective radar, since the signal only travels one way between sender and target. Another benefit is the possibility to identify the targets, because the secondary station contains active hardware and there has to be a signaling protocol. Subsequently, transmission and reception of signals occurs in different time slots and does not have to be simultaneous. On the other hand, the radar target needs additional hardware to implement the radar signal processing and protocol, which increases its size and power consumption.

Another system classification is by the employed signal modulation scheme.

- *Pulse modulation* is done by encoding the signal into short, low power pulses which occupy a certain bandwidth. This modulation scheme is used in ultra wideband (UWB) systems, which can have bandwidths of several gigahertz. A large bandwidth allows a high range resolution as discussed in section 3.2.

However, UWB regulations severely limit the allowed transmit power, which in turn limits the range of such systems and its ability to work in areas with obstacles. Advantageous is the low power consumption.

- *Frequency modulation*, with the most famous system being FMCW radar, uses frequency chirps with a certain bandwidth. The bandwidth is usually confined by regulations to several tens of megahertz in bands below 10 GHz. Hence, for sub-10 GHz systems, range resolution is behind pulse based systems. However, the allowed transmit power in this bands is in the order of several tens of milliwatts, allowing a large range. When using bands with larger center frequencies around 60 GHz to 80 GHz, the range is reduced, but the bandwidth and therefore range resolution increases. Receivers for frequency modulated signals are well researched in literature and therefore easy to implement.

Regarding the specification set in section 1.2, a secondary radar system using FMCW is chosen for the design. Especially the demand for real-time capability and scalability make primary radars such as the mentioned active reflector system unfeasible, since the radar target always needs to transmit data back to the fixed station. Thus, the position update rate will decrease with every added mobile station. FMCW furthermore allows a large range with the possibility to penetrate non-metallic obstacles while having a moderate range resolution.

2.2 Time of Flight Location Measurement Schemes

There are three basic location measurement schemes described in literature, which can be implemented together with a hardware capable of measuring ToF [Gie10, VWG+03, LT09]. In this section, a brief overview of those schemes is given to motivate the decision which one to implement in the system to be developed.

Time of Arrival (ToA) In the simplest case it is assumed that all involved hardware, mobile stations and base stations alike, are perfectly synchronized and the time instance of any signal transmission is known. A signaling scheme could be that each base station transmits a signal in a predefined order, which is received by a mobile station. The mobile stations does not need to transmit. The ToA is then equal to the ToF and directly relates to the distance between the mobile and a certain base station.

The result in the mobile station is then a distance vector with one component for each base station. The location of the mobile then has to be calculated from this distance vector. Geometrically speaking, it means to find the intersection of circles around the base stations in a 2D scenario, as shown in Fig. 2.1, or spheres in 3D. Since the single distance measurements are prone to statistical errors, the circles will not intersect all in one point, but rather leave an area, where the mobile

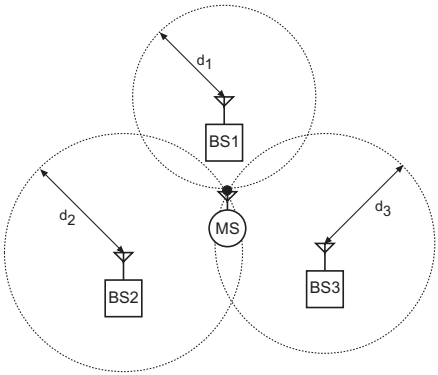

Figure 2.1: Position estimation using RToF or ToA with three base stations

target is probably located. This is the main reason, why a symbolic solution of the intersection problem is not feasible in real implementations. A more practical way is to formulate an error minimization problem, which is done in section 4.8.3 in the frame of a grid search algorithm for position estimation.

However, because of the prerequisite that all involved stations, especially the mobile, have to be synchronized, the time of arrival scheme is rarely applied in actual implementations.

Time Difference of Arrival (TDoA) The TDoA scheme does not require all units to be synchronized as ToA but only the base stations, though the signaling scheme is the same. Base stations transmit signals to the mobile subsequently. Since the mobile is not synchronous to the infrastructure, the measured ToFs do not directly relate to distances, but pseudo ranges. Evaluated are, as the name suggests, pairs of measured time differences between the different base stations. Geometrically, the problem can be considered as intersection of hyperbolas in 2D, as presented in Fig. 2.2, or hyperboloids in 3D. The estimation of the position in a real implementation can again be done similar to ToA.

Since the mobile is passive and not synchronized, TDoA systems allow for an unlimited number of mobile stations without impairing the system update rate. The most prominent example of such a system is GPS.

Round Trip Time of Flight (RToF) The result of the RToF scheme is again a distance vector like in ToA with the same geometrical interpretation. However, for RToF only the two stations just involved in a measurement have to be synchronized coarsely at a time. The signaling scheme is as follows. The mobile

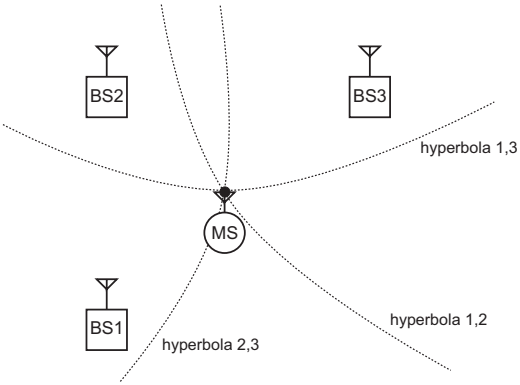

Figure 2.2: Position estimation using TDoA with three base stations

station transmits a signal to a base station, which calculates a pseudo range. The base station transmits a signal back to the mobile station, yielding another pseudo range. From both pseudo ranges, the distance between the two stations can be calculated. The synchronization and distance calculation is detailed in section 3.6. This two-way signaling scheme is repeated for every base station. It is also the major drawback of RToF, because with every added mobile station, the system update rate decreases. Advantageous is, that implementation and position estimation is simpler than with TDoA. The RToF scheme can be applied in TDoA systems to synchronize the base stations.

According to the specifications from section 1.2, the use of TDoA will be favorable to accommodate the need for scalability. However, the developed hardware shall be as flexible as possible to allow the use of any of the above schemes. For the verification of the hardware, RToF is better suited than TDoA because of the simpler protocol, the ability to measure distances wirelessly and directly and the smaller dependency of the location error on geometric conditions [Gie10].

2.3 Performance Measures

Precision and Accuracy The locations measured by a local positioning system exhibit errors, as any measuring device does. The definitions for precision and accuracy basically follow established literature on electronic distance and position measurement systems [Str13, Gie10].

The measuring error d_e is the distance of the position $\underline{m} = (x_\mathrm{m}, y_\mathrm{m}, z_\mathrm{m})$ mea-

sured by the system to the true position $\underline{r} = (x_0, y_0, z_0)$.

$$d_\mathrm{e} = \sqrt{(x_\mathrm{m} - x_0)^2 + (y_\mathrm{m} - y_0)^2 + (z_\mathrm{m} - z_0)^2} \tag{2.1}$$

For a distance measurement, the sign of the error can be of importance, so for the one-dimensional case, the distance error is defined as

$$d_\mathrm{e} = d_\mathrm{m} - d_0. \tag{2.2}$$

The standard deviation σ_p of a series of N measurements characterizes the precision or repeatability of a single measurement within defined, constant conditions. An example is a measurement series within one scenario, e.g. in a certain room. For a 3D localization system, the standard deviation of each of the three components of the measurement series has to be determined. It can be estimated by

$$\underline{\sigma_\mathrm{p}} \approx \left(\frac{1}{N-1} \cdot \sum_{i=1}^{N} (\underline{m}_i - \overline{\underline{m}})^{\circ 2} \right)^{\circ \frac{1}{2}}, \tag{2.3}$$

with $\underline{m}_i$ being a single 3D measurement and $\overline{\underline{m}}$ being a vector with the mean values for the complete series. The $\circ$ represents the Hadamard notation for component-wise square and root of a vector. This definition, although rarely used, can provide meaningful insights into error sources. For example, the height information is sometimes imprecise, because the base station setup has too little altitude difference.

To compare different systems, the definition of a one-dimensional standard deviation is useful. It seems reasonable to consider the single components as single measurements, which leads to

$$\sigma_\mathrm{p} \approx \sqrt{\frac{1}{N-1} \cdot \sum_{i=1}^{N} [(x_{\mathrm{m},i} - \overline{x_\mathrm{m}})^2 + (y_{\mathrm{m},i} - \overline{y_\mathrm{m}})^2 + (z_{\mathrm{m},i} - \overline{z_\mathrm{m}})^2]}. \tag{2.4}$$

The total precision of the system for comparison is then defined as the mean precision for measurements in M different scenarios.

$$\overline{\sigma_\mathrm{p}} = \frac{1}{M} \sum_{j=1}^{M} \sigma_{\mathrm{p,j}} \tag{2.5}$$

It has to be noted from (2.3), that the standard deviation or precision does not give any information on the relation of the measurement to the true reference position. This relation is established by the accuracy of the system, which is for

a defined scenario given by

$$\sigma_{\mathrm{a}} \approx \sqrt{\frac{1}{N-1} \cdot \sum_{i=1}^{N} [(x_{\mathrm{m},i} - x_{0,i})^2 + (y_{\mathrm{m},i} - y_{0,i})^2 + (z_{\mathrm{m},i} - z_{0,i})^2]}. \tag{2.6}$$

Analogous to the total system precision, the total system accuracy is defined as the mean accuracy for measurements in M different scenarios.

$$\overline{\sigma_{\mathrm{a}}} = \frac{1}{M} \sum_{j=1}^{M} \sigma_{\mathrm{a,j}} \tag{2.7}$$

Resolution Another important system parameter is resolution. It describes the separability of two radar targets in terms of a minimum target distance, where both can still be detected. Resolution in a radar system is degraded by multipath propagation of the signal, which overlaps with the wanted line-of-sight signal and increases the location uncertainty. Since the formalization of the system resolution is dependent on its architecture, it will be detailed in section 3.2.

Coverage Coverage of a localization system is the area, in which mobile stations can be localized by the system. It is limited by regulations, the allowed transmit power and the modulation scheme. Furthermore, the scenario will have a severe impact since it may contain obstacles like walls, which attenuate signals. However, coverage can be increased by using additional anchor nodes and combining them in a network. Details on coverage under the condition of additive white Gaussian noise and free space path loss can be found in section 3.4.1.

Deployment The time and infrastructure necessary to set up the system is important for ad-hoc applications like the E-SPONDER system. A static system can be designed to rely on infrastructure such as Ethernet for communication and protocol handling between the base stations. In general, this allows very good overall system performance, since the medium for data exchange has a predictable latency and quality of service. Furthermore, a connection to a power grid can be foreseen, which relaxes power management. Calculation of the position can be done on a server in the network, removing processing load from the stations.

An ad-hoc system on the other hand has to rely on battery power and a wireless channel for communication. All calculations and signal processing has to be done within the stations, which calls for an elaborate power management. A method for quick setup has to be implemented to provide the base stations with their current reference position, e.g. by using integrated GPS modules. Since synchronization of the units is also done wirelessly, accuracy and precision of such systems is usually behind static ones.

Scalability and Update Rate The number of addressable mobile stations and the rate with which positions are provided are interrelated. In a radar system, update rate strongly depends if there is a two-way communication between the nodes. Using a two-way communication, update rate is decreased proportional to the number of mobile stations to be addressed. For one-way signaling, update rate is only decreased starting from a certain number of mobile stations, which is reached when the positions calculated in the mobiles cannot be forwarded by the network anymore due to capacity limitations.

Robustness Robustness describes the ability of a system to handle difficult situations, while still providing useful output. For a positioning system, a difficult situation could be a complex scenario with lots of reflections and attenuation or, related to that, a loss of contact to one or several of the base stations. Robustness of a system can be increased by adding redundancy, such as more base stations or, as described in this work, use multiple frequency bands.

2.4 Commercial Radio Frequency Localization Systems

Table 2.1 gives an overview of localization systems based on radio frequency signals, which are currently on the market. Unless otherwise noted, the parameters are taken from the specification sheets provided by the manufacturers.

A well-known localization system on the market is the *Ubisense 7000 series*. It uses UWB pulses in the range of 6 GHz to 8 GHz to measure ToF and, ultimately, TDoA. It provides a high update rate with good accuracy. The major disadvantage is the fixed infrastructure, which uses cables for synchronizing the base stations. Furthermore, locations are not determined by the mobile units, but by a centralized localization server instead.

The German company *ZigPos* manufactures a system based on the ZigBee IEEE 802.15.4 standard using signal phase measurements to determine locations with accuracies of several tens of centimeters. It supports up to 255 stations according to the standard, which might be a limiting factor in large-scale crisis scenarios. Major advantages are the completely wireless infrastructure and the possibility of having an integrated sensor network with communications and multi-hop capabilities.

The *nanoLOC* system from *Nanotron* uses a chirp spread spectrum (CSS) modulation for distance measurements in the 2.4 GHz ISM band. The fact sheet from the manufacturer states accuracies in the centimeter range, however, the author's own measurements showed values in the meter range. The measurement was done in a classroom approximately five by five meters using four nanoLOC anchors and one mobile. The system is based on a RToF scheme with two-way ranging between the mobile and the base stations, which limits the update rate and scalability. All

system components are completely wireless.

The *Symeo LPR-2D* uses the FMCW principle at the ISM band at 5.8 GHz, which is also applied for the system developed in this thesis. It reaches very good accuracy below 10 cm making use of directional antennas and phased array technology with AoA evaluation. The high update rate allows the use in real time applications, such as crane tracking in mining operations. The stations are wireless and thus easily deployable.

For the sake of completeness, the overview also includes the currently most popular localization system, which is the satellite based GPS. An accuracy for the system of around 8 m is stated with a precision of 4 m, however, it strongly depends on atmospheric conditions and the surroundings of the receiver. In dense urban areas, it may increase to several tens of meters due to signal reflections from buildings. Furthermore, the latitude and longitude values are usually more accurate than altitude. The most obvious advantage of GPS is the localization in a global scale and the availability of low cost receivers. Disadvantageous is, that due to the weak signals, the system does not work inside buildings. To enhance the rather coarse accuracy of GPS, a method called differential GPS can be employed. It makes use of an infrastructure of GPS reference stations with fixed global coordinates. Since their coordinates are known, the error imposed on the satellite signals due to atmospheric conditions can be calculated. The reference stations then forward the correction data to differential GPS receivers via a communications link. Typical accuracies are in the order of 0.2 m [Lei15].

Manufacturer	**Ubisense**	**ZigPos**	**Nanotron**	**Symeo**	**NAVSTAR**
Name	7000 series	eeRTLS	nanoLOC	LPR-2D	GPS
Reference	[Ubi14]	[Zig14]	[Nan14]	[Sym14]	[NAV14]
Technology	UWB, TDoA with AoA	ZigBee, IEEE 802.15.4	Chirp Spread Spectrum, RToF	FMCW, TDoA and AoA	Code Multiplex
Band	6 GHz - 8.5 GHz	2.4 GHz	2.4 GHz - 2.48 GHz	5.725 GHz - 5.875 GHz	1.575 GHz, 1.227 GHz
Accuracy / m	0.3	0.3	4[1]	0.1	8, 0.2 with DGPS
Update Rate	33.75 Hz	10 Hz	3 Hz[1]	25 Hz	1 Hz
Range / m	160	n/a	n/a	400	n/a
Comm. channel	✓	✓	✓	×	×
Infrastructure	fixed, cabled	wireless	wireless	wireless	satellite
Remarks	location server based		test with 4 anchors and 1 mobile	directional antennas, phased array	

1 author's measurement

Table 2.1: Comparison of state-of-the-art radio frequency localization systems

3 FMCW Ranging and Synchronization

3.1 Ranging Basics

This section shall provide an introduction to the FMCW ToF measurement principle according to [Gie10, Str13]. It is based on the reflective radar front end model shown in Fig. 3.1(a). At suitable points during the derivations, the model will be extended to the two-way radar.

The basic ideal reflective radar front end consists of a chirp generator, transmit and receive antennas, a signal multiplier or mixer, which multiplies received and transmitted signals, and a signal processing block containing filtering and calculation of a spectral representation of the base band signal, from which the distance to the target can be determined.

During transmission, a linear frequency chirp with bandwidth B_{fm}, starting frequency ω_0 and duration T_{fm} as depicted in Fig. 3.1(b) is generated. The instantaneous angular frequency $\omega(t)$ is a linear function of time.

$$\omega(t) = \omega_0 + \mu' t \tag{3.1}$$

The transmitting signal is then described by

$$s_{\mathrm{tx}}(t) = A_{\mathrm{tx}} \cdot \cos\left(\int \omega(t)\mathrm{d}t\right) = A_{\mathrm{tx}} \cdot \cos\left(\omega_0 t + \frac{\mu'}{2}t^2 + \varphi_{\mathrm{tx}}\right), \tag{3.2}$$

with A_{tx} being the voltage amplitude of the transmitted signal. The chirp gradient μ characterizes the slope of the chirp whereas μ' is used in conjunction with the angular frequency ω_0. φ_{tx} describes an arbitrary starting phase.

$$\mu = B_{\mathrm{fm}}/T_{\mathrm{fm}} \tag{3.3}$$

$$\mu' = 2\pi\mu \tag{3.4}$$

After being sent, the chirp is propagated in the medium with speed c, and reflected back from an obstacle to the transceiver. The passed time for the signal to arrive again at the transceiver then equals the ToF τ, which is calculated considering the round trip time to the obstacle and back and depending on their distance d_0 to

$$\tau = \frac{2d_0}{\mathrm{c}}. \tag{3.5}$$

The station receives a delayed replica of the transmitted chirp with changed signal

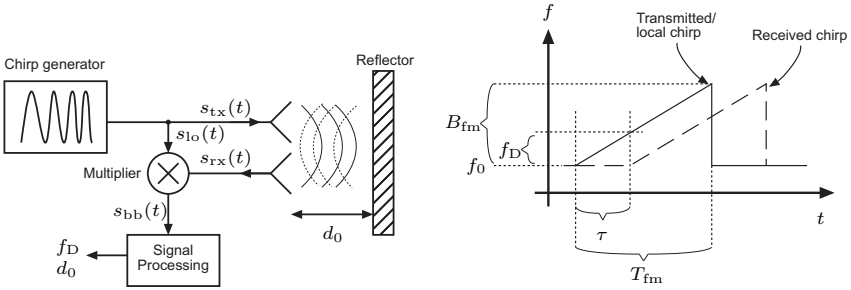

(a) Block diagram (b) Chirp signals

Figure 3.1: Block diagram and chirp signals of a reflective FMCW radar system

amplitude and phase.

$$s_{\mathrm{rx}}(t) = A_{\mathrm{rx}} \cdot \cos\left(\omega_0(t-\tau) + \frac{\mu'}{2}(t-\tau)^2 + \varphi_{\mathrm{rx}}\right). \tag{3.6}$$

The amplitude A_{rx} of the received signal incorporates path loss as well as antenna gains. In the receiver, the transmitted and reflected chirps are mixed. It is assumed, that the transmitted signal $s_{\mathrm{tx}}(t)$ drives the mixer into saturation at its local oscillator port, represented by signal $s_{\mathrm{lo}}(t)$, such that the output amplitude of the mixer only depends on the product of its voltage conversion gain a_{mix} and the amplitude of the received signal. The resulting signal is

$$\begin{aligned} s_{\mathrm{bb}}(t) =& s_{\mathrm{lo}}(t) \cdot s_{\mathrm{rx}}(t) \\ =& \frac{1}{2} \cdot a_{\mathrm{mix}} \cdot A_{\mathrm{rx}} \cdot \left[\cos\left(\mu'\tau \cdot t + \omega_0\tau - \frac{1}{2}\mu'\tau^2 + \varphi_{\mathrm{tx}} - \varphi_{\mathrm{rx}}\right)\right. \\ &\left. + \cos\left(-\mu'\tau \cdot t + 2\omega_0 t + \mu' t^2 - \omega_0\tau + \frac{1}{2}\mu'\tau^2 + \varphi_{\mathrm{rx}} + \varphi_{\mathrm{tx}}\right)\right]. \end{aligned} \tag{3.7}$$

The base band signal $s_{\mathrm{bb}}(t)$ contains two frequency components after down conversion, a constant angular beat frequency $\mu'\tau$ and another chirp starting at $2\omega_0 - \mu'\tau$ with a gradient of $2\mu'$. By applying a suitable low pass filter F with cut-off frequency ω_{g} and unity gain in pass band, the chirp is eliminated and the

resulting signal only contains the beat frequency and a phase term φ_{filt}.

$$s_{\text{filt}}(t) = s_{\text{bb}}(t)|_F = \underbrace{\frac{a_{\text{mix}} \cdot A_{\text{rx}}}{2}}_{A_{\text{filt}}} \cdot \cos\left(\mu'\tau \cdot t + \underbrace{\omega_0\tau - \frac{1}{2}\mu'\tau^2 + \varphi_{\text{tx}} - \varphi_{\text{rx}}}_{\varphi_{\text{filt}}}\right) \tag{3.8}$$

In the further course, the beat frequency will be referred to as ω_{D} or f_{D}.

$$\begin{aligned} \omega_{\text{D}} &= \mu' \cdot \tau \\ f_{\text{D}} &= \mu \cdot \tau \end{aligned} \tag{3.9}$$

It is directly related to the ToF and therefore distance d_0 between the stations. This relation can be expressed using (3.5) as

$$d_0 = f_{\text{D}} \cdot \frac{\text{c}}{2\mu}. \tag{3.10}$$

For further analyses, the spectral representation of the filtered base band signal will be needed. It can be calculated using the Fourier transform. First, a rectangular window function is applied to limit the signal to $0 \leq t \leq T_{\text{fm}}$.

$$s_{\text{filt,rect}}(t) = s_{\text{filt}}(t) \cdot \text{rect}\left(\frac{t}{T_{\text{fm}}} - \frac{1}{2}\right) \tag{3.11}$$

The Fourier transform of the rect function calculates to

$$\mathcal{F}\left\{\text{rect}\left(\frac{t}{T_{\text{fm}}} - \frac{1}{2}\right)\right\} = \text{Rect}\left(f\right) = T_{\text{fm}} \cdot \text{si}\left(\pi T_{\text{fm}} f\right) \cdot \exp\left(-\text{j}\pi f T_{\text{fm}}\right). \tag{3.12}$$

The filtered base band signal $s_{\text{filt}}(t)$ transforms to

$$\begin{aligned} &\mathcal{F}\left\{s_{\text{filt}}(t)\right\} = S_{\text{filt}}(f) \\ &= \frac{A_{\text{filt}}}{2}\left[\exp(-\text{j}\varphi_{\text{filt}}) \cdot \delta\left(f + \frac{\mu'\tau}{2\pi}\right) + \exp(\text{j}\varphi_{\text{filt}}) \cdot \delta\left(f - \frac{\mu'\tau}{2\pi}\right)\right]. \end{aligned} \tag{3.13}$$

Multiplying the rectangular window function with the filtered base band signal in time domain corresponds to a convolution in frequency domain, which is easily

calculated using the sifting property of the Dirac delta.

$$\begin{aligned} &S_{\text{rect}}(f) = S_{\text{filt}}(f) * \text{Rect}\,(f) \\ &= \frac{A_{\text{filt}}}{2}\Big[\exp(-\text{j}\varphi_{\text{filt}}) \cdot T_{\text{fm}} \cdot \text{si}\left(\pi T_{\text{fm}}\left(f + \frac{\mu'\tau}{2\pi}\right)\right) \cdot \exp\left(-\text{j}\pi T_{\text{fm}}\left(f + \frac{\mu'\tau}{2\pi}\right)\right) + \\ &\quad \exp(\text{j}\varphi_{\text{filt}}) \cdot T_{\text{fm}} \cdot \text{si}\left(\pi T_{\text{fm}}\left(f - \frac{\mu'\tau}{2\pi}\right)\right) \cdot \exp\left(-\text{j}\pi T_{\text{fm}}\left(f - \frac{\mu'\tau}{2\pi}\right)\right)\Big] \end{aligned} \tag{3.14}$$

The resulting spectrum contains two side bands. Without loss of generality, the signal can be reduced to the upper side band for further investigations.

$$\begin{aligned} &S_{\text{rect,up}}(f) = \\ &\frac{A_{\text{filt}}T_{\text{fm}}}{2} \cdot \exp(\text{j}\varphi_{\text{filt}}) \cdot \exp\left(-\text{j}\pi T_{\text{fm}}\left(f - \frac{\mu'\tau}{2\pi}\right)\right) \cdot \text{si}\left(\pi T_{\text{fm}}\left(f - \frac{\mu'\tau}{2\pi}\right)\right). \end{aligned} \tag{3.15}$$

The spectrum is now translated from a frequency spectrum to a distance spectrum. According to (3.10), the frequency in the base band is a function of distance d.

$$f(d) = \mu \cdot \frac{2d}{\text{c}} \tag{3.16}$$

Using (3.5) and (3.16), the distance spectrum of the downconverted signal with rectangular window for a reflective radar is

$$\begin{aligned} &S_{\text{rect,up}}(d) = \\ &\frac{A_{\text{filt}}T_{\text{fm}}}{2} \cdot \exp(\text{j}\varphi_{\text{filt}}) \cdot \exp\left(-\text{j}2\pi\frac{B_{\text{fm}}}{\text{c}}(d - d_0)\right) \cdot \text{si}\left(2\pi\frac{B_{\text{fm}}}{\text{c}}(d - d_0)\right). \end{aligned} \tag{3.17}$$

Analogous to (3.17), the distance spectrum for a one-way radar using $\tau_{\text{one-way}} = \tau/2 = d_0/\text{c}$ yields

$$\begin{aligned} &S_{\text{rect,up}}(d) = \\ &\frac{A_{\text{filt}}T_{\text{fm}}}{2} \cdot \exp(\text{j}\varphi_{\text{filt}}) \cdot \exp\left(-\text{j}2\pi\frac{B_{\text{fm}}}{\text{c}} \cdot \frac{d - d_0}{2}\right) \cdot \text{si}\left(2\pi\frac{B_{\text{fm}}}{\text{c}} \cdot \frac{d - d_0}{2}\right). \end{aligned} \tag{3.18}$$

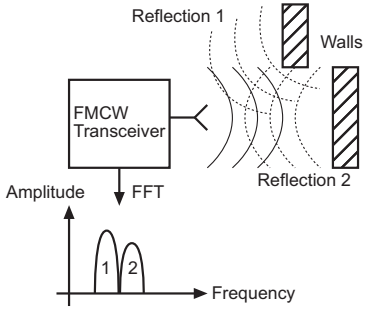

Figure 3.2: Multipath propagation and spectral effect

3.2 Range Resolution

3.2.1 Rectangular Window

The range resolution ΔR is defined as the minimum distance between two radar targets (i.e. paths), where they can still be separated. It is an important performance measure of a radar system, especially in heavy multipath scenarios, where the second target is an unwanted reflection and the main target still needs to be detected. Fig 3.2 depicts a scenario with two reflections from different walls, giving two spectral peaks. When the distance of the walls approaches each other, the ToF of both reflections becomes equal, making both targets inseparable.

Assuming two radar targets which are located symmetrically around $d = 0$ and separated in distance by Δd, the resulting distance spectrum can be derived from (3.17) as

$$\begin{aligned} &S_{\mathrm{dual}}(d, \Delta d) = \\ &A_1 \cdot \exp(\mathrm{j}\varphi_{\mathrm{filt1}}) \cdot \exp\left(-\mathrm{j}2\pi \frac{B_{\mathrm{fm}}}{\mathrm{c}}(d - \Delta d/2)\right) \cdot \mathrm{si}\left(2\pi \frac{B_{\mathrm{fm}}}{\mathrm{c}}(d - \Delta d/2)\right) + \\ &A_2 \cdot \exp(\mathrm{j}\varphi_{\mathrm{filt2}}) \cdot \exp\left(-\mathrm{j}2\pi \frac{B_{\mathrm{fm}}}{\mathrm{c}}(d + \Delta d/2)\right) \cdot \mathrm{si}\left(2\pi \frac{B_{\mathrm{fm}}}{\mathrm{c}}(d + \Delta d/2)\right) \end{aligned} \tag{3.19}$$

It is furthermore assumed, that the summation of both paths is most constructive with equal phases and amplitudes, leading to the worst-case range resolution. Therefore, the phase term can be set to 0 for both targets without loss of generality and the amplitude $A_1 = A_2$. Moreover, it is observed that the unshifted sinc function has zeros at $d = \pm \mathrm{c}/2B_{\mathrm{fm}}$. Thus, it is concluded that for $\Delta d > \mathrm{c}/B_{\mathrm{fm}}$, there will be no significant interference between the two main lobes. Due to the overlapping side lobes of each sinc function, $S_{\mathrm{dual}}(d)$ will alternate between local

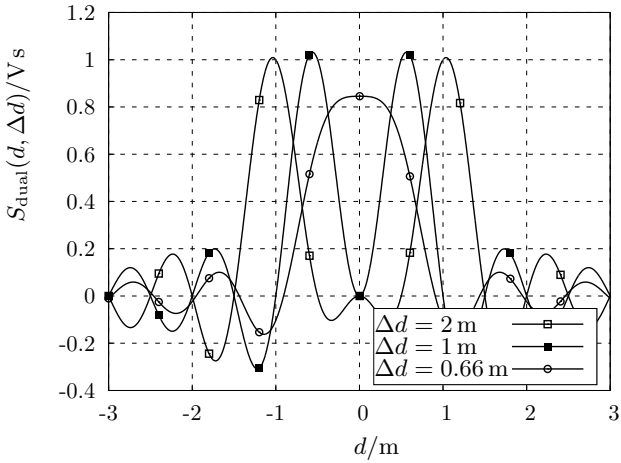

Figure 3.3: $S_{\mathrm{dual}}(d, \Delta d)$ for different distances between the paths, $\mathrm{c}/B_{\mathrm{fm}} = 1\,\mathrm{m}$

maximum and local minimum at $d = 0$ when Δd decreases. It can be shown, that for $\Delta d = \mathrm{c}/B_{\mathrm{fm}}$ the spectrum has a local minimum at $d = 0$.

However, when Δd is further reduced and approaches ΔR, both main lobes will merge to one and the local minimum at $d = 0$ will change to a local maximum, with the two targets becoming inseparable. Mathematically, this happens when

$$\frac{\partial^2}{\partial \mathrm{d}^2} S_{\mathrm{dual}}(d, \Delta R)\bigg|_{d=0} \stackrel{!}{=} 0. \tag{3.20}$$

Fig. 3.3 illustrates these findings. Solving (3.20) for ΔR results in the range resolution. By doing a polynomial series of $S_{\mathrm{dual}}(d, \Delta d)$ at $d = 0$ and truncating after d^2, the second derivative only depends on Δd. Unfortunately, the zero problem is transcendental, therefore (3.20) is solved numerically.

$$\Delta R_{\mathrm{reflective}} \approx 0.66 \cdot \frac{\mathrm{c}}{B_{\mathrm{fm}}} \tag{3.21}$$

Equation (3.21) represents the worst-case range resolution for a reflective radar in a scenario with two targets equal in phase and amplitude using a rectangular window. A similar calculation can be done for a one-way radar using (3.18), where the range resolution can by approximated by

$$\Delta R_{\text{one-way}} = 2 \cdot \Delta R_{\mathrm{reflective}} \approx 1.32 \cdot \frac{\mathrm{c}}{B_{\mathrm{fm}}} \tag{3.22}$$

Name	Highest side lobe / dB	Worst case processing loss / dB	$\Delta R_{\text{reflective}}/(\text{c}/B_{\text{fm}})$ / m
Rectangular	-13	3.92	0.66
Hamming	-43	3.10	0.84
Chebyshev ($-60\,\text{dB}$)	-60	3.23	0.89
Blackman	-58	3.47	0.96

Table 3.1: Comparison of key parameters for important window functions

From the results it is observed that increasing the bandwidth or decreasing the propagation speed enhances the range resolution. Furthermore, the range resolution of a reflective radar (as used e.g. in the RToF scheme) is better than that of a one-way radar (as used e.g. in the TDoA scheme).

A detailed derivation and investigation of the range resolution for different amplitude ratios can be found in [WSJ+11*].

3.2.2 Windowing and Discrete Fourier Transform

To determine a suitable window function for the use in a FMCW system, several parameters have to be observed. [Har78] provides a comprehensive guide to window functions and criteria for selecting a good window. For a FMCW radar system, the list can be narrowed down to the following parameters:

- Separability of two tones or worst case range resolution, as demonstrated in section 3.2.1.
- Suppression of side lobes, which occur due to spectral leakage because of the Fourier transform of finite time signals. Side lobes impair the detection of a wanted small signal in the presence of a large interferer. This case occurs when the line-of-sight path is attenuated by an obstacle and a stronger multipath component is also received.
- Worst case processing loss due to the amplitude reduction of the data near the borders of the window and the possibility, that frequencies may lie between two bins in a discrete Fourier Transform (DFT). This effect can reduce the dynamic range of the digital processing chain.

Table 3.1 compares four important window functions. The normalized range resolution $\Delta R_{\text{reflective}}/(\text{c}/B_{\text{fm}})$ was calculated numerically following the procedure from section 3.2.1. The other parameters were taken from [Har78]. The comparison shows that although the rectangular window has the best range resolution, it also suffers from the lowest side lobe suppression and the worst processing loss. Both, the Chebyshev and the Blackman window exhibit a very high side lobe

suppression with low processing loss, but also approximately 50 % drop in range resolution. The Hamming window therefore seems a good compromise for the use in the system. It shows the lowest loss and moderate side lobe suppression, while still having a high range resolution.

Furthermore, consider the fact, that it is not possible to calculate a continuous time Fourier transform in the signal processing block, but rather a DFT, since the measured signal will be sampled by an analog-to-digital converter (ADC) with sampling rate f_s. To simplify the implementation and speed up the calculation, it is reasonable to implement the DFT using the Fast Fourier Transform (FFT) algorithm. The FFT is a special implementation of the DFT, working only with binary sample lengths of $\mathrm{NFFT} = 2^n, n \in \mathbb{N}$. If fed with a real signal as in the current system, the FFT delivers a symmetric spectrum with frequencies ranging from $-f_\mathrm{s}/2 \ldots f_\mathrm{s}/2$. Thus, the width of one frequency bin equals

$$\Delta f = \frac{f_\mathrm{s}}{\mathrm{NFFT}}. \tag{3.23}$$

This frequency bin size can be translated into a distance bin size Δr, which results for a one-way radar in

$$\Delta r = \frac{\mathrm{c}\Delta f}{\mu}. \tag{3.24}$$

The length of the FFT has to be chosen such that the resulting discrete amplitude spectrum can be perfectly reconstructed. According to [Sha49], any function limited to the bandwidth $f_\mathrm{g} \leq f_\mathrm{s}/2$ and the time T_fm can be specified by giving NFFT samples, where

$$\mathrm{NFFT} \geq 2T_\mathrm{fm} f_\mathrm{g}. \tag{3.25}$$

For a chirp duration of 2.5 ms and a base band cut-off frequency of 3 MHz, $\mathrm{NFFT} \geq 15\,000$, with the next binary size being $2^{14} = 16384$. For a sampling frequency of 10 MHz and chirp bandwidth of 150 MHz the resulting distance bin size would be 3.05 m. However, the exact maximum in the spectrum can be detected according to the sampling theorem when using a suitable interpolation method. Since the spectrum is sinc-shaped, sinc interpolation would be the algorithm of choice. However, to reduce complexity of calculation, the simpler parabolic interpolation of the main lobe only has also proven effective [Str13].

Finally it is observed, that the number of measured samples is $T_\mathrm{fm} \cdot f_\mathrm{s} = 25000$, which is larger than the minimum necessary FFT sample size. Considering noise, it would be beneficial to include all measured samples in the calculation. Therefore, the FFT length is increased to the next binary size of $2^{15} = 32768$. The surplus samples are set to zero (zero padding).

3.3 Frequency Band Selection

To determine which frequency bands are suitable for a LPS, several constraints need to be considered. As determined in the previous section, a large chirp bandwidth is crucial for multipath separability. Also, frequency bands with higher center frequency usually offer larger bandwidths. Opposed to that, path loss increases for higher frequencies, thereby limiting the range of the system and decreasing the signal-to-noise ratio (SNR). Hence, staying below 10 GHz poses a suitable compromise between range and bandwidth since two large license-free ISM bands at 2.4-2.4835 GHz with 83.5 MHz and 5.725-5.875 GHz with 150 MHz bandwidth are available according to the *Electronic Communications Committee (ECC) Recommendation 70-03* [Ele13]. *Federal Communications Commission (FCC) Part 18* [Fed14] even allows 100 MHz bandwidth in the 2.4 GHz band, which will be used for the design. Since the system is to be fully configurable, bandwidths can be switched according to the local regulations.

Because the targeted range is low and so are the transmit powers, the system can be classified as short range device (SRD). SRDs describe RF devices having low capability of interfering with other radio equipment. The ECC recommendation defines the powers for SRDs in the specified ISM bands as 20 dBm equivalent isotropically radiated power (EIRP) at 2.4 GHz and 14 dBm EIRP at 5.8 GHz.

3.4 System Imperfections

3.4.1 Thermal Noise

In this section, an investigation is done on how accurate a range can be estimated using the FMCW one-way radar system in the presence of thermal noise, but neglecting multipath propagation.

The lower bound of the variance of any unbiased estimator for a certain parameter in a system is expressed by the Cramér-Rao lower bound (CRLB). In a FMCW radar system, the distance has to be estimated from the base band beat frequency. Given a noisy signal, the variance of the estimated distance has a theoretical lower limit, which will be derived in the following section. The derivation from [RB74] for frequency estimation is extended to range estimation.

Assume a base band signal similar to (3.8) with added white Gaussian noise,

$$s_{\mathrm{filt,n}}(t) = s_{\mathrm{filt}}(t) + w(t) = A_{\mathrm{filt}} \cos(\mu' \frac{d_0}{\mathrm{c}} t + \varphi) + w(t), \tag{3.26}$$

where $w(t)$ is a realization of a normally distributed process with $\mathcal{N}(0, \sigma_w^2)$. Using this model, a SNR can be calculated, which is the power of the signal divided by noise power. Noise power can be calculated using the Fourier transform of the autocorrelation of the Gaussian noise process, which is constant at σ_w^2. Thus,

SNR can be defined as

$$\mathrm{SNR} = \frac{A_{\mathrm{filt}}^2}{\sigma_w^2}. \tag{3.27}$$

Assume further that the signal is observed using N samples, which were obtained with sampling rate $T_{\mathrm{s}} = 1/f_{\mathrm{s}}$. Then the sampling vector is $\underline{X}$ and its elements are

$$\underline{X} = [X_0, X_1, \ldots, X_{N-1}], \tag{3.28}$$

$$X_n = s_{\mathrm{filt}}(t_n) + w(t_n), \tag{3.29}$$

where t_n is the n-th sample taken, thus $t_n = nT_{\mathrm{s}}$.

The probability density function of the multivariate normal distribution for $\underline{X}$ with the unknown parameter d_0 simplifies to

$$f(\underline{X}; d_0) = \frac{1}{\sqrt{(2\pi\sigma_w^2)^N}} \exp\left(-\frac{1}{2\sigma_w^2}\sum_{n=0}^{N-1}(X_n - \mu_n)^2\right), \tag{3.30}$$

assuming the individual samples are uncorrelated[1]. Consequently, the mean value yields

$$\mu_n = A_{\mathrm{filt}} \cos(\mu' \frac{d_0}{\mathrm{c}} t_n + \varphi). \tag{3.31}$$

The Cramér-Rao lower bound for the estimator of d_0 is the inverse of the Fisher information $\mathcal{J}$.

$$\mathrm{var}(d_0)_{\mathrm{th}} \geq \mathcal{J}^{-1} \tag{3.32}$$

If the second derivative with respect to d_0 of the natural log probability density function exists, then $\mathcal{J}$ evaluates to

$$\mathcal{J} = -\mathrm{E}\left[\frac{\partial^2}{\partial d_0^2} \ln f(\underline{X}; d_0)\right], \tag{3.33}$$

where $\mathrm{E}[\cdot]$ is the expectation. Substitution with (3.30) yields

$$\mathcal{J} = \frac{A_{\mathrm{filt}}^2 \mu'^2 T_{\mathrm{s}}^2}{\mathrm{c}^2 \sigma_w^2} \sum_{n=0}^{N-1} n^2 \sin^2(\mu' \frac{d_0}{\mathrm{c}} n T_{\mathrm{s}} + \varphi). \tag{3.34}$$

For large N, the sum can be simplified to $(1/6)N^3$, such that the Cramér-Rao lower bound for the one-way radar calculates as

$$\mathrm{var}(d_0)_{\mathrm{th}} \geq \mathcal{J}^{-1} \approx \frac{6\mathrm{c}^2}{\mu'^2 T_{\mathrm{s}}^2 N^3 \mathrm{SNR}}, \tag{3.35}$$

1 The covariance matrix then simplifies to $1/\sigma_w^2 \cdot \mathcal{I}$, with $\mathcal{I}$ being the identity matrix

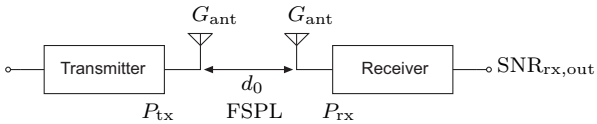

Figure 3.4: Block diagram for estimation of receiver SNR

together with the SNR definition from (3.27). Replacing $\mu' = 2\pi B_{\text{fm}}/T_{\text{fm}}$ and considering the fact, that the number of samples $N = T_{\text{fm}}/T_{\text{s}}$, the bound can be rewritten as

$$\text{var}(d_0)_{\text{th}} \geq \frac{6\text{c}^2 T_{\text{s}}}{(2\pi)^2 B_{\text{fm}}^2 T_{\text{fm}} \text{SNR}}. \tag{3.36}$$

Since the distance estimation is done in the receiver, the SNR of the receiver shall furthermore be derived with the help of the model from Fig. 3.4.

The best possible SNR can be achieved when assuming free space between transmitter and receiver. Free space path loss can be approximated as [Fri46]

$$\text{FSPL} = \left(\frac{4\pi d_0 f_0}{\text{c}}\right)^2. \tag{3.37}$$

Note that this number represents attenuation. Taking into account the transmitted power P_{tx} and two antennas with a gain of G_{ant} each, and neglecting the transmitted noise because it is below the channel noise, the received power is

$$P_{\text{rx}} = P_{\text{tx}} G_{\text{ant}}^2 \text{FSPL}^{-1}. \tag{3.38}$$

The SNR at the receiver output is now written depending on its noise factor and SNR at the input, which is equivalent to the noise factor definition using noise temperatures,

$$F_{\text{rx}} = \frac{\text{SNR}_{\text{rx,in}}}{\text{SNR}_{\text{rx,out}}} = \frac{\frac{P_{\text{rx}}}{P_{\text{nrx}}}}{\text{SNR}_{\text{rx,out}}} = \frac{T_0 + T_{\text{rx}}}{T_0}, \tag{3.39}$$

where $T_0 \approx 290\,\text{K}$ and T_{rx} is the noise temperature of the receiver. Using the fact, that noise power can be approximated as

$$P_{\text{nrx}} \approx \text{k} T_0 B_{\text{noise}}, \tag{3.40}$$

the SNR at the receiver output can be rewritten as

$$\text{SNR}_{\text{rx,out}} = \frac{P_{\text{tx}} G_{\text{ant}}^2 \text{FSPL}^{-1}}{T_0 F_{\text{rx}} \text{k} f_{\text{g}}} = \frac{\text{c}^2 P_{\text{tx}} G_{\text{ant}}^2}{(4\pi)^2 d_0^2 f_0{}^2 T_0 F_{\text{rx}} \text{k} f_{\text{g}}}, \tag{3.41}$$

using the base band bandwidth f_{g} as the noise bandwidth.

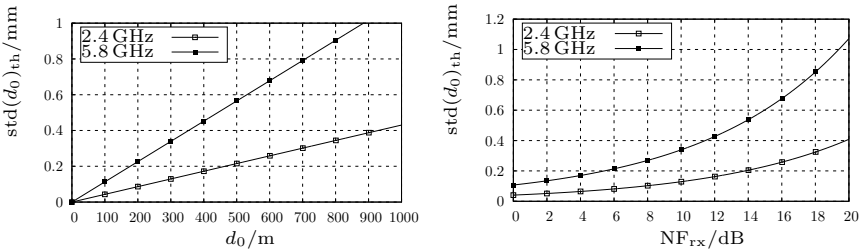

(a) CRLB versus distance (b) CRLB versus noise figure

Figure 3.5: Minimum standard deviation of distance estimation in ISM bands

Having the SNR of the receiver, the lower bound for the precision of the distance estimation in a one-way radar can be calculated as a function of the system parameters. Substituting (3.41) in (3.36) and extracting the square root yields the standard deviation

$$\mathrm{std}(d_0)_{\mathrm{th}} = \sqrt{\mathrm{var}(d_0)_{\mathrm{th}}} \geq \sqrt{\frac{24 T_{\mathrm{s}} d_0^2 f_0{}^2 T_0 F_{\mathrm{rx}} \mathrm{k} f_{\mathrm{g}}}{B_{\mathrm{fm}}^2 T_{\mathrm{fm}} P_{\mathrm{tx}} G_{\mathrm{ant}}^2}}. \tag{3.42}$$

It can be seen, that parameters distance and carrier frequency linearly increase the standard deviation, while sampling time or base band cut-off frequency contribute with their square root. Furthermore, the estimation will be more precise, when the chirp bandwidth or time and transmit power are increased, which is clear from common sense.

Fig. 3.5 shows the minimum standard deviation versus distance and versus receiver noise figure for the two ISM bands at 2.4 GHz and 5.8 GHz. The plots assume the following parameter set: $f_{\mathrm{s}} = 10\,\mathrm{MHz}, d_0 = 300\,\mathrm{m}, \mathrm{NF}_{\mathrm{rx}} = 10\,\mathrm{dB}, f_{\mathrm{g}} = 5\,\mathrm{MHz}, G_{\mathrm{ant}} = 3$. For the 2.4 GHz band, $B_{\mathrm{fm}} = 100\,\mathrm{MHz}, T_{\mathrm{fm}} = 1.66\,\mathrm{ms}, P_{\mathrm{tx}} = 100\,\mathrm{mW}$ and for the 5.8 GHz band $B_{\mathrm{fm}} = 150\,\mathrm{MHz}, T_{\mathrm{fm}} = 2.5\,\mathrm{ms}, P_{\mathrm{tx}} = 25\,\mathrm{mW}$. For receiver noise figures of less than 8 dB, $\mathrm{std}(d_0)_{\mathrm{th}}$ stays below 0.5 mm. This very good result proves the common understanding, that frequency estimation is not affected very much by thermal noise.

It has to be noted that the CRLB just derived is a theoretical limit of the variance of the range estimation in the presence of thermal noise only. A real system will also exhibit other effects, such as quantization or phase noise, which will add to the statistical error, as well as systematic errors such as synchronization offsets. Those effects will be detailed in the following sections.

3.4.2 Compression and Intermodulation

Important linearity measures of analog signal processing front ends are the compression and intermodulation intercept points [Ell07].

Compression is a reduction of the gain of a circuit, which should be constant in the ideal case. It occurs in operation areas, where the large signal transfer function starts to roll off, often close to the borders of the supply voltages. This effect causes the signal to clip and harmonics being created. It is often described with the 1-dB compression point, which is the vector $(\mathrm{IP}_{1\mathrm{dB}}, \mathrm{OP}_{1\mathrm{dB}})$. It depicts at which input power and output power the gain of the circuit has dropped by 1 dB compared to an ideal constant gain.

Obviously, the radar signal is not impaired by a front end just exhibiting compression behavior, as long as the received signal power stays within defined bounds. Assuming free space path loss using (3.37) and a minimum distance of 1 m between transmitter and receiver, the input-referred compression point of the receiver in dBm has to be

$$\frac{\mathrm{IP}_{1\mathrm{dB}}}{\mathrm{dBm}} > 10\log\frac{P_{\mathrm{tx}}}{\mathrm{mW}}\mathrm{dBm} - 20\log\frac{1\,\mathrm{m}}{\mathrm{m}}\mathrm{dB} - 20\log\frac{f_0}{\mathrm{Hz}}\mathrm{dB} - 20\log\left(\frac{4\pi}{\mathrm{c}/(\mathrm{m/s})}\right)\mathrm{dB}. \tag{3.43}$$

At $f_0 = 5.725\,\mathrm{GHz}$ and $P_{\mathrm{tx}} = 25\,\mathrm{mW}$, $\mathrm{IP}_{1\mathrm{dB}} > -33\,\mathrm{dBm}$.

Another important effect is intermodulation, which is the generation of spurious beat tones due to a non-linear transfer function when the circuit is fed with a composition of multiple tones. Especially third order intermodulation distortion is a widely used measure to describe the linearity of a circuit, because the generated spurs occur closely to the wanted fundamentals [San99]. To test a circuit for intermodulation distortion, two tones with frequencies f_1, f_2 and equal amplitudes are applied and the amplitude ratio between the intermodulation products at $2f_1 - f_2, 2f_2 - f_1$ and the fundamentals are recorded. This amplitude ratio will be named IM3. To characterize the amount of intermodulation distortion, the third order intermodulation intercept point $(\mathrm{IIP}_{\mathrm{IM3}}, \mathrm{OIP}_{\mathrm{IM3}})$ is used. It is an extrapolated point, where the power of the fundamental and the power of the third order intermodulation products would be equal.

Assume the radar receives a line-of-sight signal along with one multipath signal, which are separated in distance by Δd. Usually the multipath reflection has only little more delay than the line-of-sight signal, which results in two closely spaced beat tones in the base band spectrum. Further assume, that the receiver shows third order intermodulation distortion. Then, the distance spectrum contains components with $\pm\Delta d/2$, corresponding to the received signals, and $\pm 3\Delta d/2$, corresponding to the third order intermodulation products.

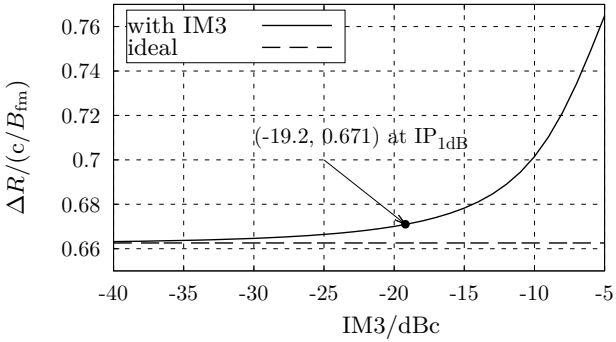

Figure 3.6: Normalized range resolution for reflective radar versus IM3

Analogous to (3.19), the distance spectrum with rectangular windowing can be expressed as

$$
\begin{aligned}
&S_{\mathrm{IM3}}(d, \Delta d) = \\
&A_{\mathrm{rx}} \exp(\mathrm{j}\varphi_{\mathrm{filt1}}) \exp\left(-\mathrm{j}2\pi \frac{B_{\mathrm{fm}}}{\mathrm{c}}(d - \Delta d/2)\right) \mathrm{si}\left(2\pi \frac{B_{\mathrm{fm}}}{\mathrm{c}}(d - \Delta d/2)\right) \\
&+ A_{\mathrm{rx}} \exp(\mathrm{j}\varphi_{\mathrm{filt2}}) \exp\left(-\mathrm{j}2\pi \frac{B_{\mathrm{fm}}}{\mathrm{c}}(d + \Delta d/2)\right) \mathrm{si}\left(2\pi \frac{B_{\mathrm{fm}}}{\mathrm{c}}(d + \Delta d/2)\right) \\
&+ a_{\mathrm{IM3}} A_{\mathrm{rx}} \exp(\mathrm{j}\varphi_{\mathrm{IM3,1}}) \exp\left(-\mathrm{j}2\pi \frac{B_{\mathrm{fm}}}{\mathrm{c}}(d - 3\Delta d/2)\right) \mathrm{si}\left(2\pi \frac{B_{\mathrm{fm}}}{\mathrm{c}}(d - 3\Delta d/2)\right) \\
&+ a_{\mathrm{IM3}} A_{\mathrm{rx}} \exp(\mathrm{j}\varphi_{\mathrm{IM3,2}}) \exp\left(-\mathrm{j}2\pi \frac{B_{\mathrm{fm}}}{\mathrm{c}}(d + 3\Delta d/2)\right) \mathrm{si}\left(2\pi \frac{B_{\mathrm{fm}}}{\mathrm{c}}(d + 3\Delta d/2)\right)
\end{aligned}
\tag{3.44}
$$

As during derivation of the range resolution in section 3.2.1, the amplitudes of both received signals are assumed equal to A_{rx}. Furthermore, the amplitudes of the intermodulation products are scaled with factor a_{IM3}. The amplitude ratio IM3 then equals

$$\mathrm{IM3} = 20 \log a_{\mathrm{IM3}}\ \mathrm{dBc}. \tag{3.45}$$

Due to the complexity of the model, the calculation of the range resolution is again done numerically. The normalized range resolution for different intermodulation ratios is plotted in Fig. 3.6 for a reflective radar along with the ideal range resolution without intermodulation distortion. The relation between $\mathrm{IIP}_{\mathrm{IM3}}$ and

IM3 is given as [San99]

$$\frac{\mathrm{IIP_{IM3}}}{\mathrm{dBm}} = \frac{P_{\mathrm{rx}}}{\mathrm{dBm}} - \frac{\mathrm{IM3/dBc}}{2}, \tag{3.46}$$

where P_{rx} is the power of one of the received signals. Using the often-cited relation that the $\mathrm{IIP_{IM3}}$ is 9.6 dB higher than $\mathrm{IP_{1dB}}$ [San99], the range resolution penalty can be estimated, when the receiver is operated at 1 dB gain compression, using

$$\frac{\mathrm{IIP_{IM3}}}{\mathrm{dBm}} - \frac{\mathrm{IP_{1dB}}}{\mathrm{dBm}} = -\frac{\mathrm{IM3/dBc}}{2} \stackrel{!}{=} 9.6 \rightarrow \mathrm{IM3} = -19.2\,\mathrm{dBc}. \tag{3.47}$$

From Fig. 3.6, a normalized range resolution of 0.671 can be read for this location.

It can be concluded, that intermodulation distortion does not severely affect range resolution of the radar as long as the amplitude ratio stays below around $-20\,\mathrm{dBc}$.

3.4.3 Automatic Gain Control

The automatic gain control (AGC) loop is part of the signal processing in a radio frequency receiver. Its purpose is to equalize amplitude changes, which occur for example because of fading or movement, and ensure that the ADC always gets maximum level. It consists of a variable gain amplifier (VGA) and a detector, usually a square-and-filter circuit using a diode and a capacitor with a much lower cut-off frequency than the expected signals to determine the envelope of the signal. The envelope is then compared to a reference signal. The resulting difference is integrated and fed as a control signal to the VGA, which multiplies the input signal with the control signal. When the AGC loop has settled, the control voltage of the VGA follows the inverse envelope of the incoming signal. In hardware, the inversion could be implemented as a VGA with inverted control characteristic (i.e. higher control voltage results in lower gain). A basic block diagram is shown in Fig. 3.7.

For a FMCW radar system, this procedure brings problems in terms of range resolution. Assume a signal with two closely spaced frequency components ω_1, ω_2 in time domain (e.g. a line-of-sight and a multipath signal). The envelope signal is then periodically changing amplitude from zero to maximum. The AGC loop will try to equalize the amplitude of the signal by following the envelope and thus change the signal and its spectrum. To determine the resulting spectrum, the input signal is assumed to be

$$V_{\mathrm{i}}(t) = A_{\mathrm{LOS}} \cos(\omega_1 t) + a_{\mathrm{MP}} A_{\mathrm{LOS}} \cos(\omega_2 t). \tag{3.48}$$

When the AGC loop has not yet locked, the envelope calculates as

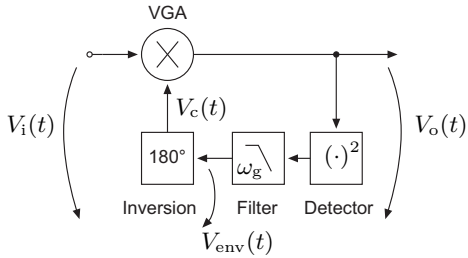

Figure 3.7: AGC loop model

$$V_\mathrm{env}(t) = \left.\frac{V_\mathrm{i}(t)^2}{V_0}\right|_{\omega<\omega_\mathrm{g}} = \frac{1}{2V_0}\left(A_\mathrm{LOS}^2 + a_\mathrm{MP}^2 A_\mathrm{LOS}^2\right) + a_\mathrm{MP} A_\mathrm{LOS}^2 \cos(\omega_1 - \omega_2)t, \tag{3.49}$$

applying the detector, the low pass filter and using a normalization voltage V_0 (which is a property of the detector). It is assumed that $\omega_\mathrm{g} \ll \omega_1, \omega_2$. The signal controlling the VGA needs to be inverse to the envelope to equalize amplitude changes. For the given input signal, this can be modeled as a phase shift by 180°. As a result, the control signal calculates as

$$V_\mathrm{c}(t) = \underbrace{\frac{1}{2V_0}\left(A_\mathrm{LOS}^2 + a_\mathrm{MP}^2 A_\mathrm{LOS}^2\right)}_{A_0} - \underbrace{\frac{a_\mathrm{MP} A_\mathrm{LOS}^2}{V_0}}_{A_1} \cos(\omega_1 - \omega_2)t. \tag{3.50}$$

A graph showing examples of all relevant signals for base band frequencies of 1 MHz and 1.1 MHz is presented in Fig. 3.8.

The VGA multiplies the control signal normalized to a voltage V_1 with the input signal, yielding for the output signal

$$\begin{aligned} V_\mathrm{o}(t) &= \frac{V_\mathrm{c}(t) \cdot V_\mathrm{i}(t)}{V_1} \\ &= \frac{1}{V_1}\left(A_0 A_\mathrm{LOS} - \frac{A_1 a_\mathrm{MP} A_\mathrm{LOS}}{2}\right)\cos\omega_1 t + \frac{1}{V_1}\left(A_0 a_\mathrm{MP} A_\mathrm{LOS} - \frac{A_1 A_\mathrm{LOS}}{2}\right)\cos\omega_2 t \\ &- \frac{A_1 A_\mathrm{LOS}}{2V_1}\cos\left(2\omega_1 - \omega_2\right)t - \frac{A_1 a_\mathrm{MP} A_\mathrm{LOS}}{2V_1}\cos\left(2\omega_2 - \omega_1\right)t \end{aligned} \tag{3.51}$$

It can be seen that the output signal of the VGA still contains both input components, but also third order intermodulation products around both carriers, which are smaller in magnitude.

As investigated in section 3.4.2, intermodulation should not severely impair

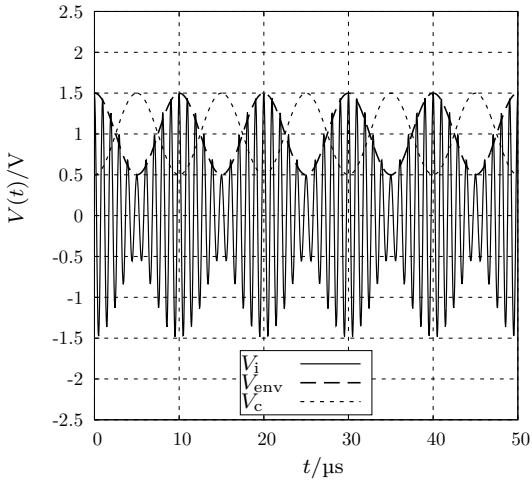

Figure 3.8: AGC signal examples in multipath scenario

range resolution. However, to mitigate problems, it is beneficial to design the AGC with a rather low cut-off frequency. This in turn makes a calibration phase necessary before transmitting a chirp signal to prevent distorting the received signal while the AGC is still trying to lock. Another possibility is to use the calibration phase to determine the gain value of the VGA and deactivate the AGC loop during the actual transmission, leaving the determined gain setting unchanged.

3.4.4 Blockers

Due to the specification for the system to work in the ISM bands, it has to be investigated how the radar performance is influenced by other narrow band sytems operating nearby. Because of the increasing use of wireless communications in home appliances, e.g. wireless thermometers or remote controls, or data services like WLAN, the utilization of the ISM bands is constantly increasing as well.

In this section, a single tone blocker and its processing by the FMCW system is examined. It is assumed, that the blocker is present during the whole chirp duration and it is narrow in bandwidth. The received blocker signal can be described as

$$s_{\mathrm{B}}(t) = A_{\mathrm{B}} \cos\left(\omega_{\mathrm{B}} t + \varphi_{\mathrm{B}}\right). \tag{3.52}$$

The blocker signal enters the FMCW receive path and is mixed with the transmitted chirp signal (3.2), resulting in

$$\begin{aligned} s_{\mathrm{bb,B}}(t) &= s_{\mathrm{lo}}(t) \cdot s_{\mathrm{B}}(t) \\ &= \frac{a_{\mathrm{mix}} A_{\mathrm{B}}}{2} \Bigg[\cos\left((\omega_0 + \omega_{\mathrm{B}})t + \frac{\mu'}{2} t^2 + \varphi_{\mathrm{rx}} + \varphi_{\mathrm{B}} \right) \\ &\quad + \cos\left((\omega_0 - \omega_{\mathrm{B}})t + \frac{\mu'}{2} t^2 + \varphi_{\mathrm{rx}} - \varphi_{\mathrm{B}} \right) \Bigg]. \end{aligned} \tag{3.53}$$

The result shows two chirp signals being created in base band with starting frequencies $\omega_0 \pm \omega_{\mathrm{B}}$. Assuming that the blocker and the chirp starting frequency are very similar, the chirp with the sum frequency is out of band, while at least part of the chirp with the difference frequency falls in the base band bandwidth. Applying the base band filter F with cut-off frequency ω_{g} as in (3.8) thus only leaves the chirp starting with $\omega_0 - \omega_{\mathrm{B}}$.

$$s_{\mathrm{bb,B}}(t) = \frac{a_{\mathrm{mix}} A_{\mathrm{B}}}{2} \cos\left((\omega_0 - \omega_{\mathrm{B}})t + \frac{\mu'}{2} t^2 + \varphi_{\mathrm{rx}} - \varphi_{\mathrm{B}} \right) \Bigg|_F \tag{3.54}$$

Fig. 3.9 shows a graphical representation of how the chirp signal in the base band is created. In the time domain signal, it can be seen that the resulting chirp is superimposed on the base band beat signal, which has a constant frequency. Because of the base band filter, only frequency components from the chirp in the range $0 \leq \omega \leq \omega_{\mathrm{g}}$ fall in the base band bandwidth. An instantaneous base band frequency of zero is reached at the time when $\omega_0 = \omega_{\mathrm{B}}$. Consequently it depends on the frequency ω_{B}, at which time the band-limited blocker chirp appears in the base band signal. However, all blockers with $\omega_0 - \omega_{\mathrm{g}} \leq \omega_{\mathrm{B}} \leq \omega_0 + B_{\mathrm{fm}} + \omega_{\mathrm{g}}$ affect the base band signal.

The appearance of the blocker chirp in the base band can be interpreted as

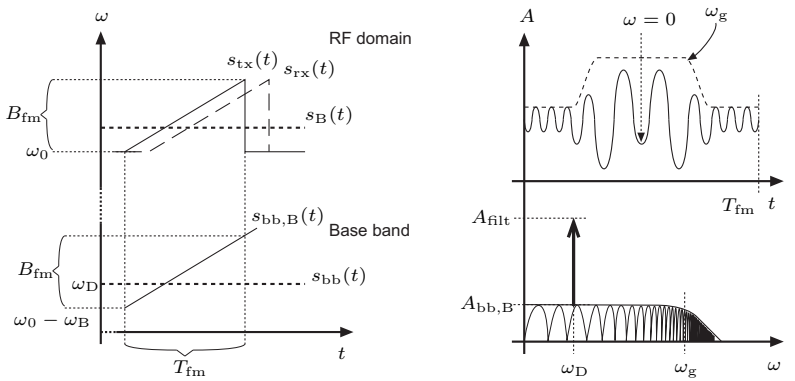

(a) Blocker downconversion (b) Time/frequency domain signals

Figure 3.9: Blocker downconversion and time/frequency domain representation of base band signals

decreasing the SNR of the wanted base band signal with frequency ω_D. To determine the amount of degradation, it is necessary to determine the amplitude $A_{bb,B}$ in the spectrum. This, in turn, is done by determining the Fourier transform of the chirp. To simplify the derivation, the chirp signal is considered as the real part of a complex signal

$$s_{bb,B}(t) = \Re\left(s_{bb,B,c}(t)\right) = \Re\left(\frac{a_{mix}A_B}{2}\mathrm{e}^{-\mathrm{j}\left(\omega_0 t+(\mu'/2)t^2\right)}\right). \tag{3.55}$$

The Fourier transform then calculates as

$$S_{bb,B,c}(\omega) = \frac{a_{mix}A_B}{2}\int_{-\infty}^{\infty}\mathrm{e}^{-\mathrm{j}\left(\omega_0 t+(\mu'/2)t^2\right)}\mathrm{e}^{-\mathrm{j}\omega t}\mathrm{d}t. \tag{3.56}$$

By completing the square in the exponent, the integrand can be rewritten.

$$S_{bb,B,c}(\omega) = \frac{a_{mix}A_B}{2}\int_{-\infty}^{\infty}\mathrm{e}^{-\mathrm{j}\left[\left(t\sqrt{\mu'/2}+\frac{\omega_0+\omega}{2\sqrt{\mu'/2}}\right)^2-\frac{(\omega_0+\omega)^2}{2\mu'}\right]}\mathrm{d}t \tag{3.57}$$

The integral can be transformed to a Fresnel integral by substitution of the term in the square,

$$x = t\sqrt{\mu'/2} + \frac{\omega_0+\omega}{2\sqrt{\mu'/2}}, \tag{3.58}$$

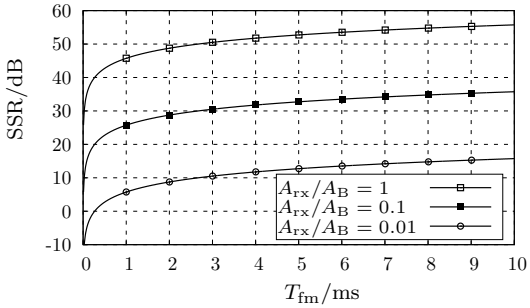

Figure 3.10: Signal-to-side lobe ratio for different ratios of $A_{\mathrm{rx}}/A_{\mathrm{B}}$, $B_{\mathrm{fm}} = 150\,\mathrm{MHz}$

leading to

$$S_{\mathrm{bb,B,c}}(\omega) = \frac{a_{\mathrm{mix}} A_{\mathrm{B}}}{2} \sqrt{\frac{2}{\mu'}} \mathrm{e}^{\mathrm{j}\frac{(\omega_0+\omega)^2}{2\mu'}} \int_{-\infty}^{\infty} \mathrm{e}^{-\mathrm{j}x^2} \mathrm{d}x. \tag{3.59}$$

Solving the Fresnel integral results in

$$S_{\mathrm{bb,B,c}}(\omega) = \frac{a_{\mathrm{mix}} A_{\mathrm{B}}}{2} \sqrt{\frac{\pi}{\mu'}} (1-\mathrm{j}) \mathrm{e}^{\mathrm{j}\frac{(\omega_0+\omega)^2}{2\mu'}}. \tag{3.60}$$

Until now, the chirp signal was assumed to be infinite in time. However, in the real system, the chirp duration is limited to T_{fm}. Therefore, the convolution of $S_{\mathrm{bb,B,c}}(\omega)$ with a rect function needs to be calculated. This was done numerically, resulting in a sinc-shaped function with constant amplitude, but with decreasing distance of its zeros versus frequency (corresponding to the chirp). Assuming a single side band representation of the signal, the amplitude of the chirp spectrum at $\omega = 0$ was calculated as

$$A_{\mathrm{bb,B}} = \frac{a_{\mathrm{mix}} A_{\mathrm{B}}}{T_{\mathrm{fm}} \sqrt{\mu}}. \tag{3.61}$$

Using the amplitude of the filtered base band signal from (3.8), the signal-to-side lobe ratio (SSR) between the wanted signal and the blocker contribution can be formed.

$$\mathrm{SSR} = 20 \log \left(\frac{A_{\mathrm{rx}} T_{\mathrm{fm}} \sqrt{\mu}}{2 A_{\mathrm{B}}} \right) \mathrm{dB} \tag{3.62}$$

The course of SSR in decibels is plotted in Fig. 3.10 for different ratios of $A_{\mathrm{rx}}/A_{\mathrm{B}}$ assuming $B_{\mathrm{fm}} = 150\,\mathrm{MHz}$. For increased resilience in case of a blocker having the same amplitude as the wanted signal it is beneficial to choose $T_{\mathrm{fm}} > 2.5\,\mathrm{ms}$, which yields $\mathrm{SSR} \approx 10\,\mathrm{dB}$.

3.4.5 Spurious Emissions

The chirp signal in modern FMCW transceivers is generated by a phase-locked loop (PLL). Depending on the architecture of the PLL, it generates different spurious emissions next to the wanted carrier, which influence the performance of the radar system. Assuming a state-of-the-art fractional-N PLL, there are three basic spur mechanisms [SNK13].

- *Reference spurs* are tones, which appear at spacings from the carrier, which are multiples of the reference frequency f_{ref} of the PLL. They can be caused by the feed-through of the reference signal through the phase detector and charge pump due to mismatches in the charge pump or by switching noise from the reference oscillator, which couples to the control signal of the RF oscillator.
- *Fractional spurs* appear at certain frequency offsets less than f_{ref} from the carrier. The cause is usually the periodicity of switching between different division ratios in the frequency divider to get the fractional ratio. Since for every channel the periodicity of those switching sequences can be different, fractional spurs appear at different carrier offsets depending on the channel.
- *Integer boundary spurs* occur at offsets which correspond to difference frequencies between integer multiples of f_{ref} and the carrier frequency. Those spurs can be seen especially at channel settings which use almost integer division ratios, because the named difference frequency then falls inside the loop bandwidth.

As a conclusion for FMCW radar systems, it can be stated, that since fractional spurs occur at different offsets for every channel and integer boundary spurs only occur at certain channels, they also contribute only low energy to the base band spectrum. Thus, they are neglected in the following investigation.

Reference spurs, however, may have an impact on the base band spectrum, because they are always present. For the reflective radar, transmitted and reflected spur characteristics are equal. For the one-way radar, it is assumed that the same PLL is used in both stations, therefore the spur characteristics are also equal.

Assume for the signal at the LO port of the mixer to be superimposed by a symmetric reference spur signal,

$$s_{\mathrm{lo,s}}(t) = a_{\mathrm{mix}} \cos\left(\omega_0 t + \frac{\mu'}{2} t^2\right) + a_{\mathrm{mix}} a_{\mathrm{s}} \cos\left((\omega_0 \pm \omega_{\mathrm{s}}) t + \frac{\mu'}{2} t^2\right), \tag{3.63}$$

with reference spur frequency $\omega_{\mathrm{s}} = n \cdot 2\pi f_{\mathrm{ref}}, n \in \mathbb{N}^+$ and relative spur amplitude a_{s}.

No.	Frequency ω	Amplitude A	Phase φ
1	$\mu'\tau$	$\frac{1}{2}a_{\mathrm{mix}}A_{\mathrm{rx}}$	$\omega_0\tau - \frac{\mu'}{2}\tau^2$
2	$\mu'\tau - \omega_{\mathrm{s}}$	$\frac{1}{2}a_{\mathrm{mix}}a_{\mathrm{s}}A_{\mathrm{rx}}$	$(\omega_0 + \omega_{\mathrm{s}})\tau - \frac{\mu'}{2}\tau^2$
3	$\mu'\tau + \omega_{\mathrm{s}}$	$\frac{1}{2}a_{\mathrm{mix}}a_{\mathrm{s}}A_{\mathrm{rx}}$	$(\omega_0 - \omega_{\mathrm{s}})\tau - \frac{\mu'}{2}\tau^2$
4	$\mu'\tau + \omega_{\mathrm{s}}$	$\frac{1}{2}a_{\mathrm{mix}}a_{\mathrm{s}}A_{\mathrm{rx}}$	$\omega_0\tau - \frac{\mu'}{2}\tau^2$
5	$\mu'\tau$	$\frac{1}{2}a_{\mathrm{mix}}a_{\mathrm{s}}^2A_{\mathrm{rx}}$	$(\omega_0 + \omega_{\mathrm{s}})\tau - \frac{\mu'}{2}\tau^2$
6	$\mu'\tau + 2\omega_{\mathrm{s}}$	$\frac{1}{2}a_{\mathrm{mix}}a_{\mathrm{s}}^2A_{\mathrm{rx}}$	$(\omega_0 - \omega_{\mathrm{s}})\tau - \frac{\mu'}{2}\tau^2$
7	$\mu'\tau - \omega_{\mathrm{s}}$	$\frac{1}{2}a_{\mathrm{mix}}a_{\mathrm{s}}A_{\mathrm{rx}}$	$\omega_0\tau - \frac{\mu'}{2}\tau^2$
8	$\mu'\tau - 2\omega_{\mathrm{s}}$	$\frac{1}{2}a_{\mathrm{mix}}a_{\mathrm{s}}^2A_{\mathrm{rx}}$	$(\omega_0 + \omega_{\mathrm{s}})\tau - \frac{\mu'}{2}\tau^2$
9	$\mu'\tau$	$\frac{1}{2}a_{\mathrm{mix}}a_{\mathrm{s}}^2A_{\mathrm{rx}}$	$(\omega_0 - \omega_{\mathrm{s}})\tau - \frac{\mu'}{2}\tau^2$

Table 3.2: Base band frequency components after mixing of spurious chirps

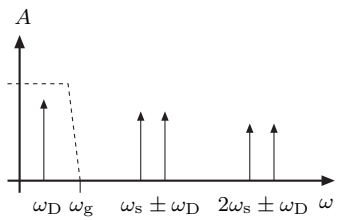

Figure 3.11: Spectral components of base band signal considering reference spurs

The received signal by the radar system then is

$$s_{\mathrm{rx,s}}(t) = A_{\mathrm{rx}} \cos\left(\omega_0(t-\tau) + \frac{\mu'}{2}(t-\tau)^2\right) + a_{\mathrm{s}}A_{\mathrm{rx}} \cos\left((\omega_0 \pm \omega_{\mathrm{s}})(t-\tau) + \frac{\mu'}{2}(t-\tau)^2\right). \tag{3.64}$$

Mixing of both signals results in several frequency components being created in the base band, which are summarized in Table 3.2. Fig. 3.11 shows the single sideband base band spectrum and the resulting frequency components. There are three components, 1, 5 and 9, which overlap to form the beat frequency ω_{D}. To predict the total amplitude, all three components need to be summed up considering their phase. The amplitude of a sum of three harmonic signals with different amplitudes and phases can be determined easiest using the Fourier

transform to calculate the amplitude spectrum. The result for the amplitude A_D of the wanted beat signal is

$$A_\mathrm{D} = \frac{a_\mathrm{mix} A_\mathrm{rx}}{2} \left(2a_\mathrm{s}^2 \cos(\omega_\mathrm{s}\tau) + 1\right). \tag{3.65}$$

It is noteworthy that the amplitude modulates with frequency ω_s versus τ. That means that there will be cases, when a received multipath signal could have a larger amplitude as the line-of-sight signal, leading to a wrong distance when using a maximum detector and spur levels are very high.

Furthermore, the spur contribution scales with the square of the relative spur amplitude and has the ability to cancel the wanted signal completely. Since the minimum value of the cosine term is -1, A_D can reach zero for certain τ when $a_\mathrm{s} = 1/\sqrt{2}$, corresponding to a spur level of $-3\,\mathrm{dBc}$. Of course this is an impractical specification. For a tolerable amplitude change of maximum $1\,\%$, $a_\mathrm{s} = 1/(10\sqrt{2})$, corresponding to a spur level of $-23\,\mathrm{dBc}$, which can be reached easily by state-of-the-art off-the-shelf PLL chips.

Also, specifications for the PLL reference frequency together with the base band filter cut-off frequency can be derived. To filter the components at $\omega_\mathrm{s} \pm \omega_\mathrm{D}$ and $2\omega_\mathrm{s} \pm \omega_\mathrm{D}$, the inequality

$$f_\mathrm{ref} > f_\mathrm{g} + f_\mathrm{D,max} \tag{3.66}$$

needs to be fulfilled, where $f_\mathrm{D,max}$ denotes the maximum base band beat frequency to be expected, which depends on the maximum measurement distance the system was specified for.

3.4.6 Quantization

Quantization in ADCs is the rounding error introduced by approximating a continuous input amplitude with discrete values. Usually, the condition of full-scale sinusoidal excitation can be assumed since the ideal base band beat signal is sinusoidal and the AGC in the system ensures maximum level.

A common way of modeling an n-bit ADC is to add a certain noise level to the signal due to the quantization error. The result is a signal-to-noise ratio, which can be calculated as [Man12]

$$\mathrm{SNR}_\mathrm{qn,dB} \approx n \cdot 6.02\,\mathrm{dB} + 1.76\,\mathrm{dB}. \tag{3.67}$$

An example would be an 8 bit ADC having $\mathrm{SNR}_\mathrm{qn,dB} \approx 50\,\mathrm{dB}$. $\mathrm{SNR}_\mathrm{qn,dB}$ increases by around 6 dB with every added bit. Increasing the number of bits to reach a better $\mathrm{SNR}_\mathrm{qn,dB}$ increases system complexity, size, power consumption and calculation time in the digital signal processing hardware, such as the FFT block and the detector. Thus, a suitable compromise has to be found.

However, it has also been shown, that modeling the quantization as noise is

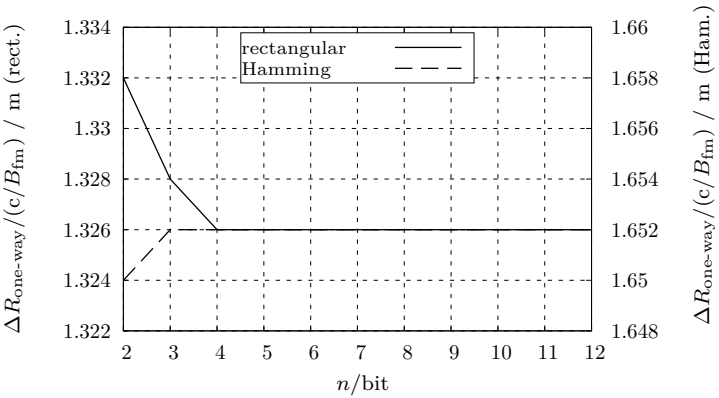

Figure 3.12: Range resolution for one-way radar versus number of ADC bits

limited to large n, where the probability density function of the quantization error represents a uniform distribution [PA04]. For small n, the signal suffers from deterministic distortion, which generates spurious frequencies and therefore limits spurious free dynamic range (SFDR). SFDR is the ratio of the root mean square values of the carrier tone to the highest spurious component. SFDR for a full scale single tone excitation using a typical 8 bit ADC is around 50 dBc to 60 dBc (e.g. *Analog Devices AD9280*), for a 12 bit ADC it amounts to around 90 dBc (e.g. *Analog Devices AD9235*). Quantization spurs of a single tone signal are usually harmonics and thus far away from the carrier in the context of FMCW signal processing. However, in case of multipath propagation, at least two tones will be processed, creating multiple spurs and mixing products. Therefore, besides the consideration of $\mathrm{SNR}_{\mathrm{qn,dB}}$, also spurs must be investigated. The influence of quantization noise together with phase noise and thermal noise on the radar performance is detailed in the following section.

Fig. 3.13 shows an example spectrum for a multipath scenario with two quantized beat tones at around 1 MHz using Hamming windowing. For the 4 bit ADC, spurious levels are high at around 25 dBc for the two-tone signal. According to [PA04], a value of around 36 dBc is to be expected for a single tone. Hence, multipath scenarios will degrade SFDR. For the 8 bit ADC, spurious levels are at 39 dBc and therefore almost below the side lobe level caused by the FFT with windowing.

Numeric simulations were carried out, determining the range resolution in the presence of an ideal quantizer. The results are plotted in Fig. 3.12. It can be seen that the range resolution, at least in the two-tone scenario, is not seriously affected by quantization. For a rectangular window it slightly increases for quantizers with

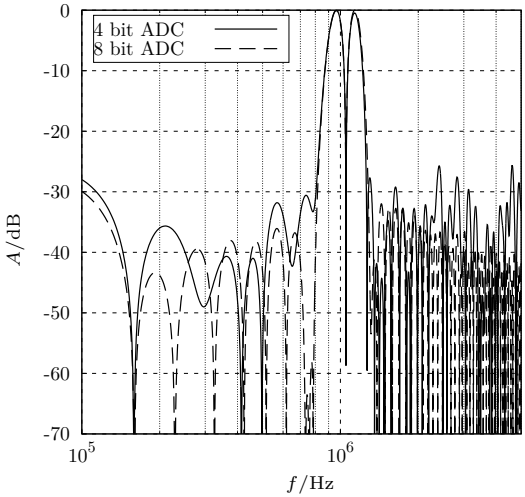

Figure 3.13: Example spectra for a multipath scenario with quantization spurs

less than 4 bit, where for the Hamming window, range resolution is almost equal to the theoretical value for all bit numbers starting from three. This favorable behaviour is due to the fact, that the spurs with highest energy for sinusoidal signals form around the harmonics of the fundamental input component, which is sufficiently far away from the line-of-sight signal and prevent the side lobes of the spurs from interfering.

As a conclusion, an ADC with at least 8 bit is chosen for the system because the expected SFDR would be below the side lobe levels of the calculated FFT and it provides some safety margin for more realistic multipath scenarios with several reflections.

3.4.7 Phase Noise

Phase noise is the short-term, random fluctuation over time of the phase $\varphi(t)$ of a signal. Empirically, it is clear that phase noise may have a stronger impact on the performance of a FMCW radar than thermal noise, since the measurement method is based on frequency estimation, which is directly affected by phase variation.

Some previous publications have dealt with the influence of phase noise on FMCW ranging performance. [SSJ+08] describes the minimum variance for frequency and delay estimation using a conversion of phase noise to additive complex

white Gaussian noise, discovering that up to a certain thermal SNR level, which corresponds to a certain distance, the ranging performance is dominated by phase noise. The resulting thermal SNR was in the order of 20 dB, corresponding to distances in the order of 100 m for a system at 5.8 GHz. [ESV12] uses a conversion from phase noise to period jitter to derive a SNR corresponding to phase noise, which is used to derive the CRLB. Furthermore, quantization noise was included. This work arrives at similar results as the one cited before. [Gie10] uses a method to derive the ranging error instead of the minimum ranging variance.

This work adapts the derivation from [ESV12] together with the determined thermal SNR from section 3.4.1 and quantization noise from section 3.4.6 to determine the ranging performance in the presence of phase noise and its dependency on different phase noise profiles. Since the system generates frequency chirps, phase noise may be different for different frequencies. However, since the bandwidth is quite confined, the phase noise characteristics at the chirp starting frequency will be used for the calculations.

Assume the following continuous wave voltage signal in the RF domain containing a time-varying phase $\varphi(t)$.

$$s_{\mathrm{cw}}(t) = A_{\mathrm{cw}} \cos\left(\omega_0 t + \varphi(t)\right) \tag{3.68}$$

This signal can be rewritten using trigonometric identities to

$$s_{\mathrm{cw}}(t) = A_{\mathrm{cw}} \left[\cos(\omega_0 t) \cos\varphi(t) - \sin(\omega_0 t) \sin\varphi(t)\right]. \tag{3.69}$$

Considering small phase fluctuations, the cosine term tends to one whereas the sine term tends to $\varphi(t)$, yielding

$$s_{\mathrm{cw}}(t) \approx A_{\mathrm{cw}} \cos\omega_0 t - A_{\mathrm{cw}} \varphi(t) \sin\omega_0 t. \tag{3.70}$$

Thus, phase fluctuations caused by phase noise can be converted to an amplitude modulation and therefore increase in noise level. This in turn allows the translation into a SNR and permits the calculation of the CRLB similar to the derivation in section 3.4.1. Furthermore, the total CRLB can be calculated as the sum of the minimum variances of all contributions to SNR in the system, which is thermal noise, quantization noise and phase noise. Note that the contributions are uncorrelated. Hence,

$$\mathrm{var}(d_0) \geq \mathrm{var}(d_0)_{\mathrm{th}} + \mathrm{var}(d_0)_{\mathrm{qn}} + \mathrm{var}(d_0)_{\mathrm{pn}}. \tag{3.71}$$

As a next step, some definitions regarding phase noise, its power spectral density and the values measured by a spectrum analyzer are in order.

The power spectral density $\underline{S}_{\varphi}(f_{\mathrm{off}})$ of the varying phase $\varphi(t)$ is the Fourier transform of its autocorrelation function $r_{\varphi\varphi}(t)$. The unit of $\underline{S}_{\varphi}(f_{\mathrm{off}})$ is $\mathrm{rad}^2/\mathrm{Hz}$. Note that the variable f_{off} is the frequency offset from the carrier.

IEEE defined the phase noise power spectral density as a single side band spectrum denoted by $L_\varphi(f)$ as follows [IEE08].

$$L_\varphi(f_{\text{off}}) = \frac{\underline{S}_\varphi(f_{\text{off}})}{2} \tag{3.72}$$

Unfortunately, the standard does not define the conversion to the commonly used form using the unit dBc/Hz. To be consistent with units, the conversion rule is presumably

$$L_\varphi(f_{\text{off}})_{\text{dB}} = 10 \log \left[L_\varphi(f_{\text{off}}) \cdot \text{Hz} \right] \text{ dBc/Hz}, \tag{3.73}$$

and, in return,

$$\underline{S}_\varphi(f_{\text{off}}) = \frac{2}{\text{Hz}} \cdot 10^{\frac{L_\varphi(f_{\text{off}})_{\text{dB}}}{10} \cdot \text{Hz}}. \tag{3.74}$$

The suffix dBc/Hz denotes that the magnitude of the spectrum was converted to decibels. To form the common logarithm it is necessary to multiply $L_\varphi(f_{\text{off}})$ with Hz. Then, to keep $L_\varphi(f_{\text{off}})_{\text{dB}}$ as a power spectral density, it is again divided by Hz. In the following derivations, measured phase noise profiles having the unit dBc/Hz will be used and it is important to point out, that the division by Hz has to be taken into account when converting between the different units.

To determine the ranging performance of the system, given phase noise measurements at different offset frequencies of the used synthesizer are taken. The measured phase noise profile can be converted to rms jitter, using the equations given in [Wal09, Max04].

$$J_{\text{rms}} = \frac{1}{2\pi f_0} \sqrt{\int_0^\infty \underline{S}_\varphi(f_{\text{off}}) \mathrm{d}f} = \frac{1}{2\pi f_0} \sqrt{\int_0^\infty \frac{2}{\text{Hz}} \cdot 10^{\frac{L_\varphi(f_{\text{off}})_{\text{dB}}}{10} \cdot \text{Hz}} \mathrm{d}f}. \tag{3.75}$$

Jitter is then down converted from RF domain to base band with the local oscillator frequency f_{LO}, since the frequency estimation is done there [ESV12].

$$J_{\text{rms,bb}} = J_{\text{rms}} \cdot \frac{\sqrt{{f_0}^2 + f_{\text{LO}}^2}}{f_0 - f_{\text{LO}}} \tag{3.76}$$

The base band jitter can then be translated to a SNR [Wal09], using

$$\text{SNR}_{\text{pn,dB}} = 20 \cdot \log \left(\frac{1}{2\pi (f_0 - f_{\text{LO}}) \cdot J_{\text{rms,bb}}} \right) \text{ dB}. \tag{3.77}$$

Together with the results for thermal noise from section 3.4.1 and 3.4.6, the minimum variance of the ranging yields

$$\text{var}(d_0) \geq \frac{6\text{c}^2 T_{\text{s}}}{(2\pi)^2 B_{\text{fm}}^2 T_{\text{fm}}} \cdot \left(\frac{1}{\text{SNR}_{\text{rx,out}}} + \frac{1}{\text{SNR}_{\text{qn}}} + \frac{1}{\text{SNR}_{\text{pn}}} \right). \tag{3.78}$$

Here an interesting observation can be made. Considering only phase noise, the distance variance is directly dependent on the integral of the phase noise power spectral density, a profile with 10 dB lower phase noise would translate to a factor 10 better variance or $\sqrt{10}$ better standard deviation.

The calculation was done exemplarily for the two phase noise profiles shown in Fig. 3.14, whose course roughly follows that of a typical RF synthesizer with a loop bandwidth around 100 kHz and the typical in-band suppression of the voltage-controlled oscillator (VCO) phase noise. Both profiles differ in noise levels by 10 dB.

Fig. 3.15 shows the calculated minimum standard deviation for the distance estimation for both profiles versus distance. The distance changes only the thermal part of the SNR, according to (3.41). Besides the total standard deviation, the single contributions from thermal noise, phase noise and quantization are also plotted. It can be seen, that the distance variation is dominated by phase noise up to a distance of around 100 m. For large distances, thermal noise determines the measurement. The impact of quantization noise was calculated for an 8 bit ADC, but the impact on the variance is negligible. For profile 1, which has around −75 dBc/Hz in-band phase noise, the minimum standard deviation in the phase-noise-dominated region is about 0.91 mm. Profile 2 shows −85 dBc/Hz, resulting in a standard deviation of 0.29 mm, showing the expected reduction by a factor of $\sqrt{10}$. Eventually, since the phase noise typically drops quite fast for offset frequencies out of the loop bandwidth, in-band phase noise up to several ten's of kilohertz can be considered most significant for ranging performance.

Typical state-of-the-art frequency synthesizers can reach phase noise levels of −75 dBc/Hz and below easily, see section 4.6.11. The standard deviation only gets significant in the centimeter range for in-band phase noise levels as high as −55 dBc/Hz. Thus, as a reasonable system specification, the synthesizer generating the chirp should have a phase noise performance of at least −70 dBc/Hz.

3.4.8 Non-linear Frequency Chirp

This section deals with the effects that non-linear frequency chirps will have on the ranging performance. Depending on the characteristics of the non-linear function superimposed on the ideal chirp, the base band spectrum will have added components of some kinds, which can be spurs or broadband disturbances as detailed in section 3.4.4. These disturbances will impair the range resolution of the radar system, if not kept low.

Literature describes several ways of producing linear frequency chirps. The output frequency is generated by a VCO in most cases, therefore one possibility would be to use a directly modulated VCO, which in turn needs linearization methods for the gain K_{VCO} [DSS06]. In this case, a simple linear voltage ramp

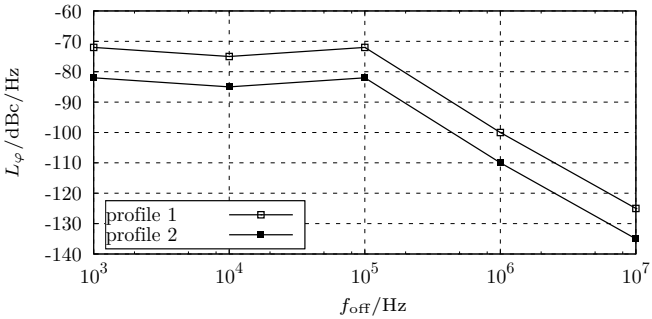

Figure 3.14: Two typical phase noise profiles for RF synthesizers with 10 dB difference

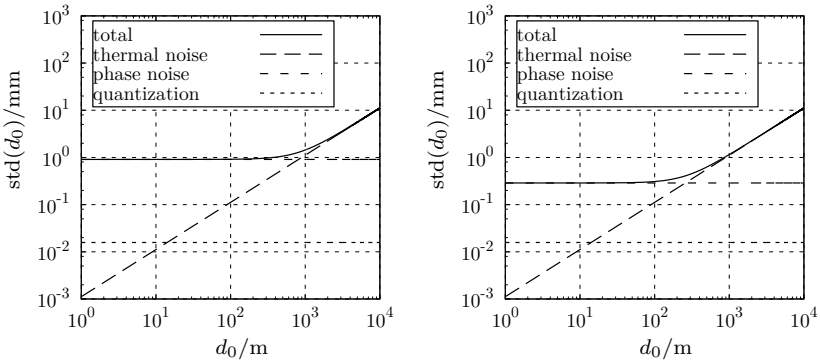

(a) Profile 1 (b) Profile 2

Figure 3.15: Minimum standard deviation for distance for both phase noise profiles at 5.725 GHz

applied to the tuning input would suffice.

Another common possibility is to stabilize the VCO using a PLL. This opens two possibilities: either the reference frequency can be modulated linearly, e.g. by using a programmable direct digital synthesis (DDS) generator [LGM+09], or the PLL frequency divider value can be decreased periodically, thus constantly increasing output frequency and producing the wanted chirp [WLS09]. Using the programmable divider approach is beneficial, since it saves the use of a large, power-consuming DDS and allows a higher level of integration.

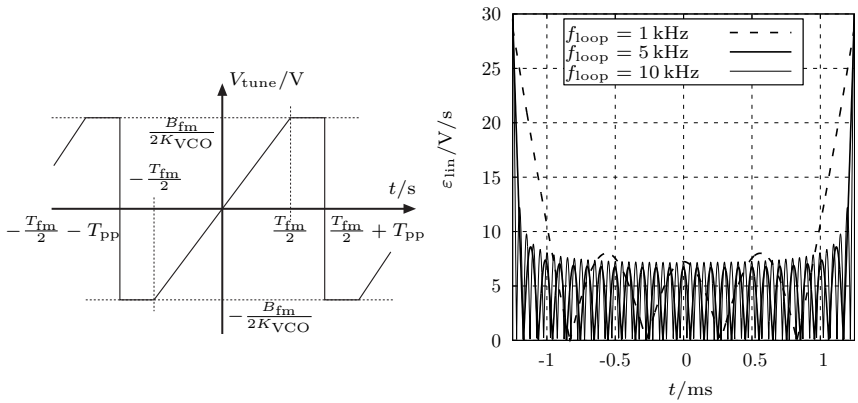

(a) Chirp model

(b) Linearity error

Figure 3.16: Chirp model for linearity investigations and linearity error due to band limitation

In the PLL-based approach, the chirp is the function which needs to pass the PLL loop in order to modulate the VCO. For a truly linear chirp, the PLL therefore must be able to track all frequency components contained in the chirp waveform. Since the chirp waveform includes discontinuities at the points where it starts and stops, its bandwidth will be infinite. The loop bandwidth of a real PLL however is limited, therefore it cannot track all of the frequency components of the chirp waveform, leading to linearity errors. In the following the effect of linearity errors on side lobe levels and range resolution will be investigated and a specification for the loop bandwidth will be derived.

The signal model used in the section is shown in Fig. 3.16(a). The chirp has a duration of T_{fm} and runs from $-T_{\text{fm}}/2$ to $T_{\text{fm}}/2$. Its amplitude $V_{\text{tune}}(t)$ is determined by the chirp bandwidth B_{fm} and the gain K_{VCO} of the VCO, which is for now assumed constant within the confined chirp bandwidth. Also included is a pre and post delay which amounts to T_{pp}. The function is assumed to continue periodically, modeling subsequent range measurements. The absolute linearity error ε_{lin} is then the derivative of $V_{\text{tune}}(t)$ subtracted by the ideal linear slope of $B_{\text{fm}}/(K_{\text{VCO}}T_{\text{fm}})$, yielding

$$\varepsilon_{\text{lin}} = \left| \frac{\partial V_{\text{tune}}(t)}{\partial t} - \frac{B_{\text{fm}}}{K_{\text{VCO}}T_{\text{fm}}} \right| . \tag{3.79}$$

One possibility to model the band limitation of the chirp signal by the PLL is using a Fourier series expansion of the chirp waveform. Examples of band limitation on the waveform are presented in Fig. 3.16(b) (for $B_{\mathrm{fm}} = 150\,\mathrm{MHz}, T_{\mathrm{fm}} = 2.5\,\mathrm{ms}, K_{\mathrm{VCO}} = 1\,\mathrm{GHz/V}, T_{\mathrm{pp}} = 10\,\mathrm{ms}$), showing a periodic linearity error, which subsides only partially with increasing loop bandwidth. This is due to the Gibbs-Wilbraham phenomenon, which states that the Fourier series approximation of a function will show ringing in the vicinity of discontinuities, that will not disappear completely even by adding more terms to the series [HH79]. This ringing can also be observed during measurements of the tuning voltage in a real system, which is described in section 4.6.10. Apart from changing the bandwidth, increasing the delay T_{pp} while keeping the bandwidth constant also decreases the error, especially in the vicinity of the discontinuities.

It should be noted that this model has certain limitations: the signal is assumed to be infinite in time whereas a real signal is time-limited. As a consequence, there is ringing present on the left and right side of discontinuities. In a real system, the ringing would only start after the discontinuity occurred. However, the insights gained using this model can be seen as a worst case estimation.

Since the chirp function is odd, the Fourier series only contains sine components.

$$V_{\mathrm{tune}}(t) = \sum_{k=1}^{k_{\mathrm{max}}} b_k \sin\left(2\pi k \frac{t}{T_{\mathrm{fm}} + 2T_{\mathrm{pp}}}\right) \tag{3.80}$$

The Fourier coefficients b_k calculate as

$$b_k = \frac{2}{T_{\mathrm{fm}} + 2T_{\mathrm{pp}}} \int_{-T_{\mathrm{pp}}-T_{\mathrm{fm}}/2}^{T_{\mathrm{fm}}/2+T_{\mathrm{pp}}} V_{\mathrm{tune}}(t) \sin\left(2\pi k \frac{t}{T_{\mathrm{fm}} + 2T_{\mathrm{pp}}}\right) \mathrm{d}t. \tag{3.81}$$

The corresponding loop bandwidth then calculates from k_{max}, resulting in

$$f_{\mathrm{loop}} = \frac{k_{\mathrm{max}}}{(2T_{\mathrm{pp}} + T_{\mathrm{fm}})}. \tag{3.82}$$

To determine the effect of the band-limited chirp on the system performance, the base band beat signal has to be calculated. This is done using the signal model analogous to section 3.1 with an instantaneous frequency

$$\omega(t) = \omega_0 + c(t) \tag{3.83}$$

where $c(t)$ is is the distorted linear frequency chirp with

$$c(t) = 2\pi K_{\mathrm{VCO}} \cdot V_{\mathrm{tune}}(t). \tag{3.84}$$

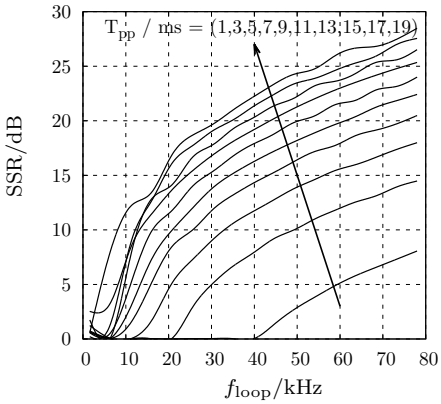

Figure 3.17: Signal-to-sidelobe ratio versus loop bandwidth for different pre/post delays, $T_{\mathrm{fm}} = 2.5\,\mathrm{ms}$, Hamming window

As a result, the transmitted signal is

$$s_{\mathrm{tx}}(t) = A_{\mathrm{tx}} \cdot \cos\left(\omega_0 t + \int_0^t c(t')\mathrm{d}t'\right). \tag{3.85}$$

Following the calculation procedure from section 3.1 and assuming any static phases to be zero, the filtered base band signal yields

$$s_{\mathrm{filt}}(t) = \frac{a_{\mathrm{mix}} \cdot A_{\mathrm{rx}}}{2} \cdot \cos\left(\underbrace{\int_0^t c(t')\mathrm{d}t'}_{\varphi_c(t)} - \underbrace{\int_0^{t-\tau} c(t')\mathrm{d}t'}_{\varphi_c(t-\tau)} + \omega_0\tau\right), \tag{3.86}$$

which shows that the base band beat frequency results from the difference of both, the original and the shifted modulated phases. It is furthermore assumed that the chirps of both stations, which are engaged in the ranging procedure, contain the same linearity errors since they are using equal PLLs.

The Fourier series model of the chirp from (3.80) is now inserted into (3.86) to form a numerical model, which is used to calculate the base band signal and its Fourier transform using the FFT algorithm. From this point, the effects on the ranging performance can be derived.

Fig. 3.17 shows the signal-to-side lobe ratio in decibels for the distance spectrum of a base band signal using band-limited chirps. As already discussed in sections 3.2.2 and 3.4.4, the side lobe level directly affects range resolution and,

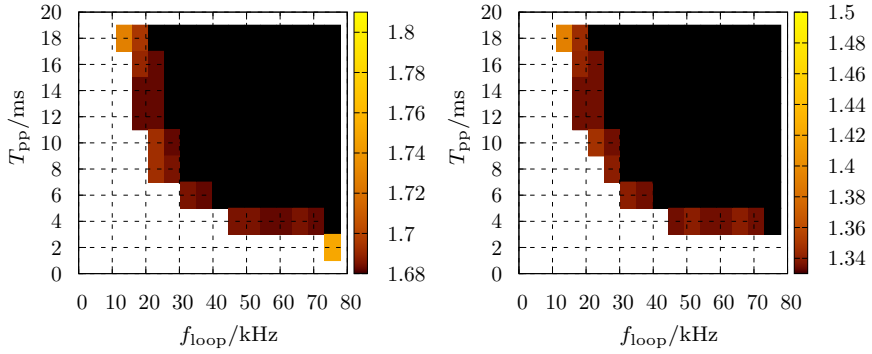

(a) $\Delta R_{\text{one-way}}/(c/B_{fm})$ / m, Hamming window

(b) $\Delta R_{\text{one-way}}/(c/B_{fm})$ / m, Rectangular window

Figure 3.18: Range resolution versus loop bandwidth for different pre/post delays, $T_{fm} = 2.5\,\text{ms}$

in case of broadband interferers, also degrades SNR. The plot shows SSR versus f_{loop} and versus pre and post delay T_{pp}. Naturally it is clear that for increasing delay the chirp will have less distortion, since the ringing caused by the jump discontinuity will have more time to decay. Moreover, for each delay there is a certain bandwidth, from which on SSR $> 0\,\text{dB}$ and a maximum detector would be able to recognize the line-of-sight path. Increasing the loop bandwidth will also reduce the side lobe level, because the amplitude of spurious signals which are generated due to the mixing of non-linear chirps decreases.

Fig. 3.18 shows a level plot of the range resolution $\Delta R_{\text{one-way}}/(c/B_{fm})$ versus f_{loop} and T_{pp} using Hamming or rectangular windowing during FFT and a maximum detector for line-of-sight detection. As for the SSR plot, also here there are white areas for low f_{loop} and low T_{pp}, where the line-of-sight could not be detected. Furthermore, there are border areas, where the signal was detected, but the range resolution is degraded due to a high SSR. Comparing the level plots for the two window function shows that they are very similar, while using the Hamming window the border line extends by a few detectable areas.

As a conclusion, it can be stated that a delay time of at least around 7 ms together with a loop bandwidth of at least 50 kHz needs to be used to not impair the range resolution and have some safety margin for the SSR. Together with a chirp duration of 2.5 ms, the chirp rate would be 1/16.5 ms or 60 chirps per second.

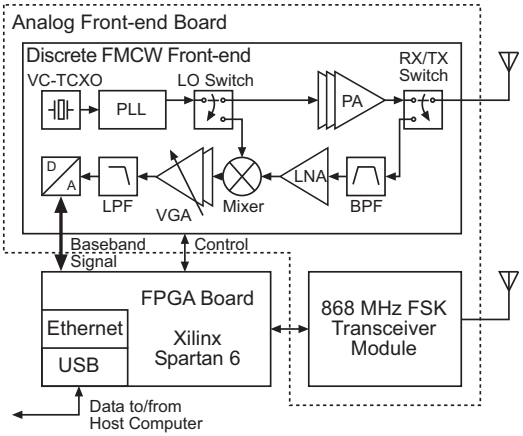

Figure 3.19: Block diagram of the discrete FMCW transceiver

3.5 Test System Design

3.5.1 Transceiver Architecture

Before designing integrated circuits for a dual band localization system, a discrete single-band FMCW front end using off-the-shelf high performance components was built to evaluate the system architecture, radar performance and post-processing algorithms [JWSE12a*]. It was decided to use the 5.8 GHz ISM band, because it allows high bandwidth and therefore better range resolution.

The chosen system architecture is shown in Fig. 3.19. A photograph of the hardware is depicted in Fig. 3.20. The task of the analog front end is to transmit and receive frequency chirps. As presented in the basics, it consists of a transmit and receive path, however in the implemented version they are switchable. Since a secondary radar topology was specified, it is not necessary to transmit and receive at the same time, therefore one antenna is sufficient.

It furthermore consists of an 868 MHz frequency shift keying (FSK) transceiver module and a *Xilinx Spartan 6* field-programmable gate array (FPGA) development board for signal processing, control of the front end and interfacing with a host computer via Ethernet and universal serial bus (USB) interface.

In transmit mode, the PLL forwards the chirp signal via the LO switch to the power amplifier (PA) and via the RX/TX switch to the antenna. In receive mode, the received signal from the antenna is propagated via the RX/TX switch, a band-pass filter (BPF) and low noise amplifier (LNA) to the mixer, which also

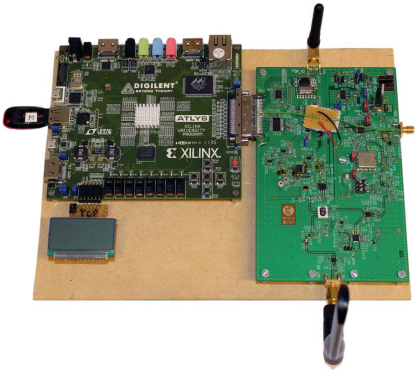

Figure 3.20: Hardware of the discrete FMCW transceiver, size 25 cm×19 cm×4 cm

gets the local chirp signal from the PLL via the LO switch.

It was decided to generate the chirp using a PLL rather than using a directly modulated VCO, because the chirp linearity is greatly improved. The chirp is created by the PLL *ADF4158* from *Analog Devices* [Ana13], which contains internal counters for easy frequency chirp generation. The reference frequency is provided by a voltage-controlled temperature-compensated crystal oscillator (VC-TCXO), which can be trimmed in frequency by the FPGA.

The receiver provides the down conversion of the received chirp with the local chirp to the base band. The base band consists of two cascaded amplifiers, one is a low-noise preamplifier stage with constant gain of 20 dB to compensate for the conversion loss of the mixer, the second one is a VGA with an adjustment range of 0 to 50 dB. After low-pass filtering, the signal is sampled using an 8 bit ADC.

The receiver can be considered a low intermediate frequency type. When the distance of two stations is low, it would mean getting a very low beat frequency in the range of several Hertz. However, when processing frequencies near zero in the base band, there are several problems arising. First, since the duration of the measurement cycle is in the order of milliseconds, only fractions of one period of the beat frequency would be generated, which would be problematic when calculating the Fourier Transform. Also, the building blocks either need the ability to be DC-coupled or large blocking capacitors need to be used. Lastly, the flicker noise corner of the used semiconductor components is usually in the range between 10 kHz to 100 kHz. Therefore, the system noise figure will be high at low base band frequencies. To avoid those problems, the beat frequency is increased by deliberately delaying the generation of the local chirp by a constant time. When using the two-way ranging algorithm (see section 3.6), this additional

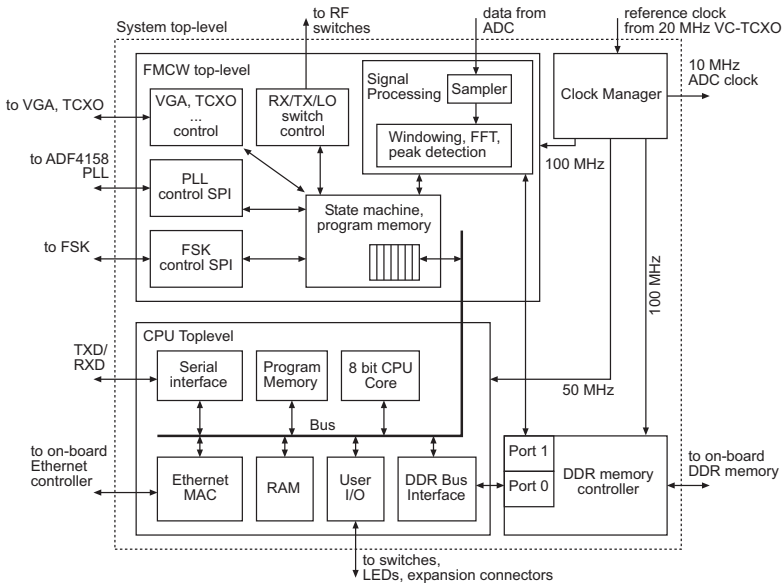

Figure 3.21: Block diagram of the digital back end

delay cancels out when calculating the distance. The minimum beat frequency was set to 1 MHz, generating enough periods for the digital processing and allowing the coupling of the stages with small capacitors in the nano-farads range.

The sample rate of the ADC was then set to 10 MHz to exceed the Nyquist-Shannon sampling theorem. It can be configured to up to 30 MHz.

The task of the FSK transceiver is to provide a data channel between different units to exchange protocol information and to allow synchronization.

3.5.2 Digital Back End

The main task of the digital back end is to process the sampled data from the ADC, calculate the FFT, estimate the peak in the spectrum and calculate the corresponding distance. Furthermore, it takes care of the control of all involved hardware.

The digital design is implemented using Verilog. Fig. 3.21 shows a block diagram. The digital design consists of two major parts, the FMCW top-level, which interfaces with the analog front end, and the CPU top-level, which provides the user interface to the system. Also, there is a double data rate (DDR)

memory controller, providing independent access ports to the external memory on the development board. Finally, a digital clock manager, driven by the 20 MHz VC-TCXO, creates and distributes clocks for all the building blocks.

For an evaluation platform as presented here, it would be beneficial to allow performing different ranging algorithms with the front end without the need to re-synthesize the FPGA design every time. Since ranging algorithms rely on a precise and deterministic timing, it is imperative to know the execution times and delays in the system. Furthermore, the internal clock frequency should be high to allow setting delays in the nanosecond scale. The use of microprocessors can hardly fulfill this requirement, so a custom batch processor architecture was implemented in FMCW top-level, providing defined execution times.

The batch processor consists of a program memory and a state machine to interpret the commands. Furthermore, each peripheral is separated into a module together with a state machine to manage the data and control flow. The user has a set of specific commands to control the peripherals, read from and write data to them or generate precise delays using timers and counters. The core and peripheral modules run at a clock frequency of 100 MHz.

The signal processing part contains a sampler, which fetches the values from the ADC and saves them to the DDR memory, so the signal can be processed later. A windowing and FFT block are used to calculate the spectrum. The spectrum is also stored in memory for later post-processing.

The second major part is the CPU top-level. It consists of an 8 bit CPU core with program and data RAM and several peripherals, which are interconnected using a bus. It is running on a 50 MHz clock. The task of the CPU is to provide a high-level programming interface and user interface for the system to test ranging and signal processing algorithms. It is based on the AVR architecture [Atm13] and therefore is supported by several tool chains including C compilers. The FMCW top-level is also connected to the bus and is mapped to the address space of the CPU for easy access.

A host computer is connected to the FMCW system via an USB-to-UART bridge or Ethernet. It can be used to control each of the front end components and for data exchange, e.g. for reading samples from the ADC.

3.6 Two-way Ranging and Synchronization

3.6.1 Overview

The algorithm presented in this section uses two FMCW units and is able to perform ToF and distance measurements between them. Because of the ToF determination, the algorithm can also be used to synchronize units. It is therefore the basis for more complex ranging protocols like RToF or TDoA, which rely on accurate synchronization.

3.6.2 System Imperfections

Accurately synchronizing two units before doing FMCW ranging is imperative to reach good accuracy. Also, the synchronization algorithm needs to be designed to be robust against system imperfections, since there are numerous error sources, which affect the accuracy of a FMCW-based measurement. The most important ones are listed below:

- Non-deterministic coarse synchronization offset $\Delta t_{12} = \tau_{12} + t_{\mathrm{FSK}}$, consisting of the ToF of the signal and a non-deterministic delay from the FSK transceiver.
- Frequency offset $2\Delta\omega$ between the clocks. This has impact on other system parameters:
  - Differences in the starting frequency ω_0 of the chirp,
  - differences in the chirp gradients μ_1, μ_2 because of the oscillators clocking the divider of the PLL to step the chirp frequency, resulting in a residual chirp in the base band and
  - differences in the timers used for the synchronization scheme, because of the oscillators clocking the timers and counters.
- Frequency drift between both clocks (mainly caused by temperature changes, should be slow compared to the duration of one measurement cycle).

3.6.3 Oscillator Alignment

The synchronization between two stations is done in multiple steps to ensure reliable distance measurements. The first step is to align the VC-TCXOs which generate the reference frequency. This step is necessary to ensure that the difference of the clock frequencies of both units is small enough to maintain a good match of the chirp generator and timers and therefore also chirp gradient μ. The alignment is performed in the following way:

- The reference station sends a continuous wave reference signal.
- The receiving station measures the frequency and checks, if it is too low or too high. It then runs a search algorithm, adjusts its VC-TCXO in the corresponding direction and repeats the measurement and check.
- When the frequency measured by the receiving station is within a defined error bound, the alignment is finished.

Using this approach, a frequency offset of only $\pm 100\,\mathrm{Hz}$ was measured in the RF domain at 5.8 GHz. Using a PLL multiplier of 290, the reference frequency itself is in the range of $20\,\mathrm{MHz} \pm 0.34\,\mathrm{Hz}$, corresponding to a magnitude of only 0.034 ppm. This offset should be low enough to not seriously affect the measurement, as long as the measurement cycle time is kept in the region of some milliseconds.

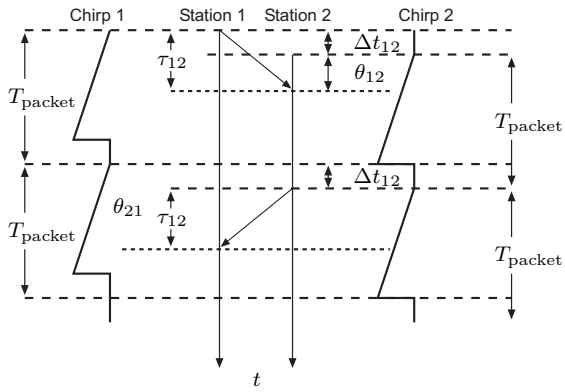

Figure 3.22: Fine synchronization scheme

3.6.4 Coarse Synchronization

When the oscillators are aligned, the next step is to perform a coarse synchronization of two units. The goal is to provide a starting time frame for fine synchronization and measurements. The accuracy of the coarse synchronization has to provide sufficient timing overlap of the received and local chirp to always get a beat frequency f_{D}, which is still in the base band bandwidth. Based on (3.9), the following relation is used to determine the necessary base band bandwidth.

$$f_{\mathrm{D}} = \mu \Delta t_{12} \tag{3.87}$$

The maximum offset time of the FSK transceiver used in the demonstrator was determined by experiments to be 50 µs, so the base band bandwidth was chosen to be 3 MHz assuming a chirp gradient of 150 MHz/2.5 ms.

3.6.5 Fine Synchronization

After the stations are coarsely synchronized, a fine synchronization is performed. The result of this step is the ToF or distance between the stations.

Fine synchronization is done by sending a chirp from the reference station 1 to the slave station 2, which measures a pseudo time of flight θ_{12}. Afterwards, the measurement cycle is repeated with both stations exchanged. Then the reference station 1 measures a pseudo time of flight θ_{21}. Out of both measured values, the real time of flight τ_{12} from station 1 to station 2 and therefore distance between the stations can be calculated.

Fig. 3.22 depicts the synchronization scheme. Timing synchronization is enclosed in time slots with the duration T_{packet}. The length of a time slot needs to accommodate the time of the chirp and processing time in the stations. The time bases of both stations differ by Δt_{12}, which is introduced by the coarse synchronization. A detailed description of the scheme is as follows:

- Station 1 starts sending a chirp to be received by station 2 at the beginning of the first time slot. After the coarse synchronization offset Δt_{12}, station 2 generates its own local chirp.
- The chirp from station 1 is received after the ToF τ_{12} and mixed with the local chirp of station 2. The pseudo time of flight $\theta_{12} = \tau_{12} - \Delta t_{12}$ is determined and sent via the FSK transceiver to station 1.
- At the beginning of the second time slot station 1 generates its local chirp. After Δt_{12} station 2 starts sending a chirp to be received by station 1.
- The chirp from station 2 is received by station 1 after the ToF τ_{12} and mixed with the local chirp of station 1. Another pseudo time of flight $\theta_{21} = \Delta t_{12} + \tau_{12}$ is determined. Since station 1 knows also the previously measured ToF from station 2, the real time of flight can be calculated as $\tau_{12} = (\theta_{12} + \theta_{21})/2$. The delay Δt_{12} can also be determined.

3.6.6 Error Analysis

The proposed synchronization scheme is now examined using FMCW signals and the robustness against the most important system imperfections, which are non-deterministic coarse synchronization offset and frequency offset, is analyzed.

The analysis is carried out in two steps, as is the fine synchronization scheme. Starting from the basic FMCW signals described by Eqs. (3.2) and (3.6), the resulting signal $s_{\text{mix2}}(t)$ in station two after mixing in the first step can be described as

$$\begin{aligned} s_{\text{mix2}}(t) &= s_{\text{tx1}}(t - \tau_{12}) \cdot s_{\text{lo2}}(t - \Delta t_{12}) \\ &= s_{\text{tx1}}(t - \tau_{12}) \cdot s_{\text{lo2}}(t - \tau_{12} - t_{\text{FSK}}). \end{aligned} \tag{3.88}$$

Phase terms and amplitude scaling factors can be neglected for the following investigation without loss of generality. The transmitted signal $s_{\text{tx1}}(t)$ from station 1 is shifted by the ToF, while the local chirp signal $s_{\text{lo2}}(t)$ from station 2 is shifted by the coarse synchronization offset. Applying a low pass filter F to remove the unwanted mixing product results in

$$\begin{aligned} s_{\text{mix2}}(t)|_F = \frac{1}{2}\cos\Big[&\omega_1(t - \tau_{12}) + \frac{\mu'}{2}(t - \tau_{12})^2 \\ &- \omega_2(t - \tau_{12} - t_{\text{FSK}}) - \frac{\mu'}{2}(t - \tau_{12} - t_{\text{FSK}})^2\Big]. \end{aligned} \tag{3.89}$$

The frequency difference $2\Delta\omega$ between the oscillators ω_1, ω_2 is modeled using the following substitutions

$$\begin{aligned} \omega_1 &= \omega_0 + \Delta\omega, \\ \omega_2 &= \omega_0 - \Delta\omega. \end{aligned} \tag{3.90}$$

As a result, one gets for the base band signal in station 2

$$s_{\text{filt2}}(t) = \frac{1}{2}\cos\left[t\underbrace{(2\Delta\omega + \mu' t_{\text{FSK}})}_{\omega_{\theta_{12}}} + \varphi_1\right]. \tag{3.91}$$

The constant phase φ_1 is a result of the mixing process and carries no distance information. The measured frequency $\omega_{\theta_{12}}$ corresponds to the pseudo time of flight θ_{12}, which obviously is not a function of the real time of flight.

In the second step of the synchronization scheme, station 1 mixes its local chirp with the received and delayed chirp from station 2. Note that the transmitted signal from station 2 is not only shifted by the ToF, but also by the coarse synchronization offset.

$$\begin{aligned} s_{\text{mix1}}(t) &= s_{\text{lo1}}(t) \cdot s_{\text{tx2}}((t - \Delta t_{12}) - \tau_{12}) \\ &= s_{\text{lo1}}(t) \cdot s_{\text{tx2}}(t - 2\tau_{12} - t_{\text{FSK}}) \end{aligned} \tag{3.92}$$

The calculation is performed similar to the first step. The resulting mixing product in station 1 after filtering calculates as

$$s_{\text{filt1}}(t) = \frac{1}{2}\cos\left[t\underbrace{(2\Delta\omega + 2\mu'\tau_{12} + \mu' t_{\text{FSK}})}_{\omega_{\theta_{21}}} + \varphi_2\right]. \tag{3.93}$$

The measured frequency in station 1 is now $\omega_{\theta_{21}}$. The real time of flight and therefore distance between the stations is now evaluated by subtracting the frequency measured in station 1 by the one measured in station 2.

$$\omega_{\theta_{21}} - \omega_{\theta_{12}} = 2\mu'\tau_{12} \rightarrow d_0 = \frac{\text{c}}{2\mu'}(\omega_{\theta_{21}} - \omega_{\theta_{12}}) \tag{3.94}$$

It can be seen from the previous equation that not only the non-deterministic coarse synchronization delay cancels out but also the frequency difference of both oscillators.

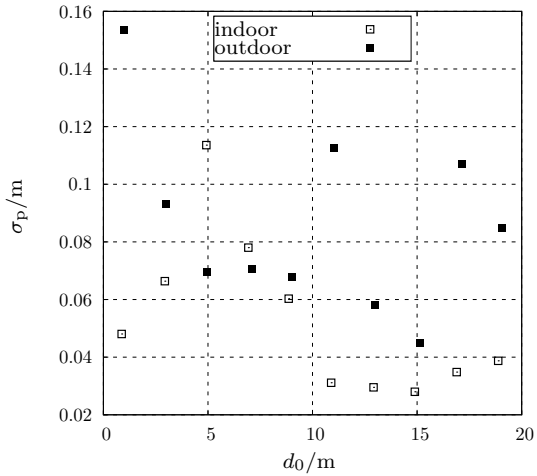

Figure 3.23: Precision for indoor and outdoor distance measurements

3.7 Test System Results

3.7.1 Measurement Setup

To verify the functionality of the test system, distance measurements between two units were done in indoor and outdoor scenarios using the two-way ranging algorithm. The units always kept a fixed height of 80 cm above ground while station 2 was moved away from station 1 for subsequent measurements. The distance measurement was verified using a laser distance meter with stated accuracy of ±1 mm. Distances were measured ranging from 1 m to 19 m with 2 m steps. For each step, at least 20 single measurements were performed. Then, the distance error d_e (mean value of the measurements d_m subtracted by the true distance d_0) were determined for both scenarios (Fig. 3.25) and the standard deviations were calculated (Fig. 3.23). To calibrate possible distance offsets due to board traces or phase responses of amplifier or mixer, the RF ports of the boards were connected together using a 30 dB attenuator to prevent saturation of the receiver. Then, the distance bias was recorded to be subtracted from the measurements later. It was determined that the bias is slightly temperature dependent, so for the indoor scenario at 25 °C, a bias of 3.07 m was determined, while for the outdoor scenario at 6 °C, 2.92 m were subtracted.

To interpret measurement results, it is also important to consider the most obvious sources of signal reflections, which is the floor and also possible nearby

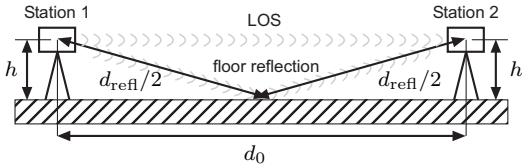

Figure 3.24: Effect of floor reflection in ranging

walls. Floor, wall or ceiling reflections become relevant starting from a certain distance between both stations depending on their height as shown in Fig. 3.24. The reflections appear as a systematic error by increasing the bias of the measurement. The critical distance can be calculated using a right-angled triangle with the catheti h, $d_0/2$ and hypotenuse $d_{\text{refl}}/2$, which is half the length of the floor reflection path. The reflected path becomes relevant, when its length approaches the line of sight (LOS) path with the added range resolution of the system, which is

$$d_{\text{refl}} \stackrel{!}{=} d_0 + \Delta R_{\text{one-way}}. \tag{3.95}$$

Again, it is assumed that both paths are equal in amplitude, which is the worst case. This relation translates to the distance d_0, where both lobes in the base band spectrum merge, yielding

$$d_0 = \frac{4h^2 - \Delta R^2_{\text{one-way}}}{2\Delta R_{\text{one-way}}}. \tag{3.96}$$

For the current system with 150 MHz bandwidth, the range resolution is 2.64 m. For usual station heights below 2 m, the floor reflection merges at a distance of less than 1.71 m and should have only little relevance. For one reason, the amplitude of the reflection is usually smaller then that of the LOS component. Secondly, the relevant distance is below the range of distances usually measured by the system. However, wall or ceiling reflections in indoor scenarios may be of relevance, e.g. in larger rooms or corridors scenario with a distance to a wall of approximately 3 m and above (corresponding to h in the model). Then the relevant distance would increase to 4.74 m.

3.7.2 Outdoor Scenario

The outdoor measurements were done on a lawn with the nearest walls from adjacent buildings being at least 10 m away from the stations. The board temperature was 6 °C. The maximum standard deviation of the measurement series is 15.4 cm, which is a good result and will also serve as a specification for the precision of

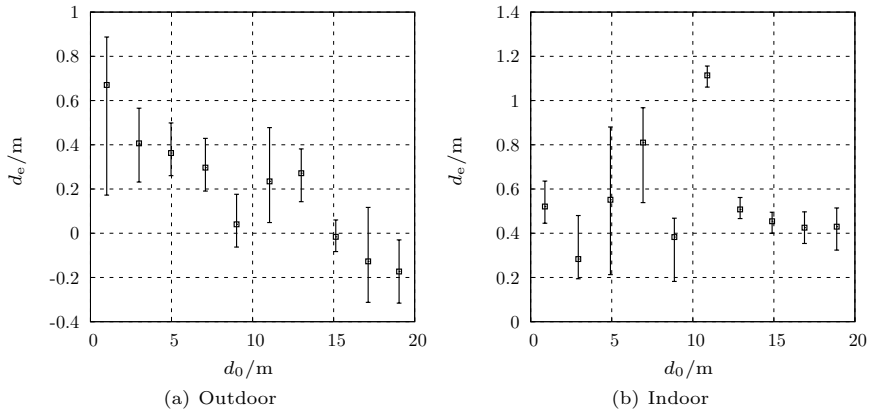

(a) Outdoor (b) Indoor

Figure 3.25: Measured distance error for outdoor and indoor scenarios

the integrated system to be designed. The absolute mean distance error outdoors amounts to 26 cm.

3.7.3 Indoor Scenario

The indoor scenario was a corridor with a length of 24.4 m, 3.2 m width and 3.4 m height, confined by doors on both ends. The board temperature was 25 °C. The maximum standard deviation for this measurement was 11.4 cm, which is comparable to the outdoor scenario. The mean distance error indoors amounts to 55 cm, which is double the outdoor error. Furthermore, it is always positive which indicates the superposition of multipath signals arriving later at the stations, thus shifting the beat frequency up in the spectrum.

3.8 Specification Summary

Table 3.3 gives an overview of the system and component specifications, which were derived in this chapter. This results will be used during circuit design, which is described in the following chapter.

Component	Parameter	Symbol	Specification
System	Min. distance	$d_{0,\mathrm{min}}$	1 m
	Max. distance	$d_{0,\mathrm{max}}$	300 m
	Update time	t_{upd}	<1 s
	Topology	-	Secondary Radar
	Accuracy	σ_{a}	<1 m indoors and outdoors
RF Front End	Noise figure	NF	<10 dB (whole receive path)
	Chirp starting frequency	f_0	2.4 GHz to 2.5 GHz (2.4 GHz band) 5.725 GHz to 5.875 GHz (5.8 GHz band)
	Bandwidth	B_{fm}	100 MHz (2.4 GHz band) 150 MHz (5.8 GHz band)
	Transmit power	P_{tx}	<20 dBm (2.4 GHz band) <14 dBm (5.8 GHz band)
	Compression Point	$\mathrm{IP}_{1\mathrm{dB}}$	>−33 dBm
	Intermodulation	IM3	<−20 dBc
Chirp Generator/ PLL	Chirp duration	T_{fm}	1.66 ms (2.4 GHz band) 2.5 ms (5.8 GHz band)
	Reference frequency	f_{ref}	20 MHz
	In-band phase noise	$L_{\varphi\,\mathrm{dB}}$	<−70 dBc/Hz
	Reference spur level	a_{s}	<−23 dBc
	Loop bandwidth	f_{loop}	>50 kHz
	Chirps per second	-	<60
Base band	Bandwidth	f_{g}	3 MHz
	ADC sampling rate	f_{s}	10 MHz
	ADC bits	n	8 bit
Digital Back End	FFT size	NFFT	$\geq 2^{15}$
	FFT window	-	Hamming
	Interpolation method	-	Parabolic

Table 3.3: Summary of the system specification

4 Dual-band Localization System

4.1 Motivation

Empirically, it seems clear that a system using multiple sources of data (i.e. measurements in different bands) to determine a parameter (i.e. distance or position) has advantages over a system using only a single data source. However, a formal motivation of the design process of a dual band LPS is necessary to get a qualitative statement on the improvement compared to a single band system.

To motivate the design, the derivation of the CRLB for distance estimation in the presence of thermal noise of a single band system from section 3.4.1 is extended to prove the enhanced distance estimation variance of a dual band system.

First, the observation vector from (3.29) is extended to include measurements from the low band and the high band.

$$\underline{X} = [X_{\mathrm{L},0}, X_{\mathrm{L},1}, \ldots, X_{\mathrm{L},N-1}, X_{\mathrm{H},0}, X_{\mathrm{H},1}, \ldots, X_{\mathrm{H},N-1}] \tag{4.1}$$

The signal model then is

$$\begin{aligned} s_{\mathrm{L}}(t) &= A_{\mathrm{L}} \cos\left(\mu'_{\mathrm{L}} \frac{d_0}{\mathrm{c}} t + \varphi_{\mathrm{L}}\right) + w_{\mathrm{L}}(t), \\ s_{\mathrm{H}}(t) &= A_{\mathrm{H}} \cos\left(\mu'_{\mathrm{H}} \frac{d_0}{\mathrm{c}} t + \varphi_{\mathrm{H}}\right) + w_{\mathrm{H}}(t). \end{aligned} \tag{4.2}$$

For each of the bands, a SNR can be defined similar to (3.27).

$$\begin{aligned} \mathrm{SNR}_{\mathrm{L}} &= \frac{A_{\mathrm{L}}^2}{\sigma_{\mathrm{L}}^2} \\ \mathrm{SNR}_{\mathrm{H}} &= \frac{A_{\mathrm{H}}^2}{\sigma_{\mathrm{H}}^2} \end{aligned} \tag{4.3}$$

Again it is assumed, that all random variables $X_i, i \in \mathbb{N}, 0 \leq i \leq 2N$ are uncorrelated, on the one hand because it is additive white Gaussian noise, on the other hand because the samples are observed in different frequency bands, namely samples $X_{\mathrm{L},i}$ in the low band and samples $X_{\mathrm{H},i}$ in the high band. A total of $2N$ samples are observed in both bands. The noise contributors are again normally distributed with $\mathcal{N}(0, \sigma_{\mathrm{L}}^2)$ and $\mathcal{N}(0, \sigma_{\mathrm{H}}^2)$, respectively. The covariance matrix $\mathcal{C}$ of

the observation vector $\underline{X}$ then simplifies to

$$\mathcal{C} = \begin{pmatrix} \sigma_{\mathrm{L}}^2 & 0 & \dots & \dots & \dots & 0 \\ 0 & \ddots & 0 & \ddots & \ddots & \vdots \\ \vdots & 0 & \sigma_{\mathrm{L}}^2 & 0 & \ddots & \vdots \\ \vdots & \ddots & 0 & \sigma_{\mathrm{H}}^2 & 0 & \vdots \\ \vdots & \ddots & \ddots & 0 & \ddots & 0 \\ 0 & \dots & \dots & \dots & 0 & \sigma_{\mathrm{H}}^2 \end{pmatrix}. \tag{4.4}$$

The probability density function of the multivariate normal distribution for vector $\underline{X}$ equals

$$f(\underline{X}; d_0) = \frac{1}{\sqrt{(2\pi)^{2N}\sigma_{\mathrm{L}}^N\sigma_{\mathrm{H}}^N}} \exp\left[-\frac{1}{2}\left(\frac{1}{\sigma_{\mathrm{L}}^2}\sum_{n=0}^{N-1}(X_{\mathrm{L},n} - \mu_{\mathrm{L},n})^2 + \frac{1}{\sigma_{\mathrm{H}}^2}\sum_{m=0}^{N-1}(X_{\mathrm{H},m} - \mu_{\mathrm{H},m})^2 \right)\right]. \tag{4.5}$$

To derive the CRLB, the Fisher information $\mathcal{J}$ is calculated.

$$\begin{aligned} \mathcal{J} =& -\mathrm{E}\left[\frac{\partial^2}{\partial d_0^2}\ln f(\underline{X}; d_0)\right] \\ =& -\mathrm{E}\left[-\frac{1}{2\sigma_{\mathrm{L}}^2}\frac{\partial^2}{\partial d_0^2}\sum_{n=0}^{N-1}(X_{\mathrm{L},n} - \mu_{\mathrm{L},n})^2\right] \\ & -\mathrm{E}\left[-\frac{1}{2\sigma_{\mathrm{H}}^2}\frac{\partial^2}{\partial d_0^2}\sum_{m=0}^{N-1}(X_{\mathrm{H},m} - \mu_{\mathrm{H},m})^2\right] \\ =& \mathcal{J}_{\mathrm{L}} + \mathcal{J}_{\mathrm{H}} \end{aligned} \tag{4.6}$$

Obviously the Fisher information is linear in case of a dual band system with uncorrelated samples. Consequently, the variance of the distance estimation for the dual band system fulfills

$$\mathrm{var}(d_{0,\mathrm{dual}}) \geq \frac{1}{\mathcal{J}_{\mathrm{L}} + \mathcal{J}_{\mathrm{H}}}. \tag{4.7}$$

With similar substitutions as in (3.36), the variance can be rewritten to

$$\mathrm{var}(d_{0,\mathrm{dual}}) \geq \frac{6\mathrm{c}^2 T_{\mathrm{s}}}{(2\pi)^2\left(B_{\mathrm{fm,L}}^2 T_{\mathrm{fm,L}}\mathrm{SNR_L} + B_{\mathrm{fm,H}}^2 T_{\mathrm{fm,H}}\mathrm{SNR_H}\right)} \tag{4.8}$$

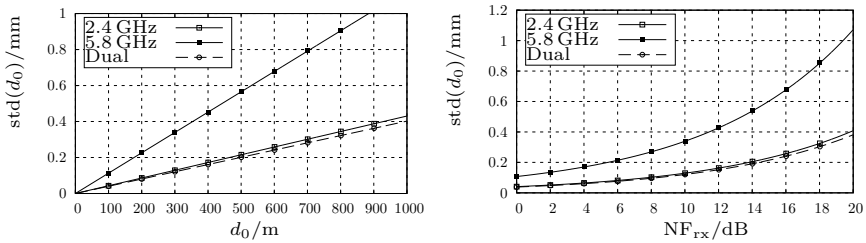

(a) CRLB versus distance

(b) CRLB versus noise figure

Figure 4.1: Minimum standard deviation of distance estimation in a dual band system considering thermal noise

This simple model shows the interesting fact, that when using an optimum estimator the variance for the dual band system is always as good as the best variance of both bands. If the SNR of the measurements of one of the bands is near zero, the minimum variance would be the same as if only the measurements of the other band were taken. Also, if the SNR in both bands is high, the variance even can get lower than the best single band variance. Fig. 4.1 compares the gained result with the bounds calculated in section 3.4.1. It shows a slightly lower standard deviation for the dual band measurement than the best single band measurement. For a very good SNR in both bands, the improvement can also be more significant. In turn, if one of the bands were impaired, e.g. due to adverse fading or attenuation in certain environments, the estimator would increase weight of the measurement result of the other band. This is especially expected to happen in densely covered outdoor scenarios or indoor scenarios. This fact also justifies the use of multiple bands as a multipath mitigation strategy.

The gained results motivate the design and evaluation of a local positioning hardware, which is capable of operating in multiple frequency bands. The position estimation method of the dual band system is detailed in section 4.8.3.

4.2 Semiconductor Technology

The design of the integrated circuits presented in this thesis was done using a silicon-germanium (SiGe) BiCMOS technology from IBM [IBM13]. It is a standard 180 nm CMOS process, which provides additional npn SiGe bipolar transistors. It features

- Seven metal layers, five metals with standard thickness and two thick metal layers, one of which uses copper instead of aluminum. This metal stack allows the fabrication of inductors with high quality factors and transmission lines.

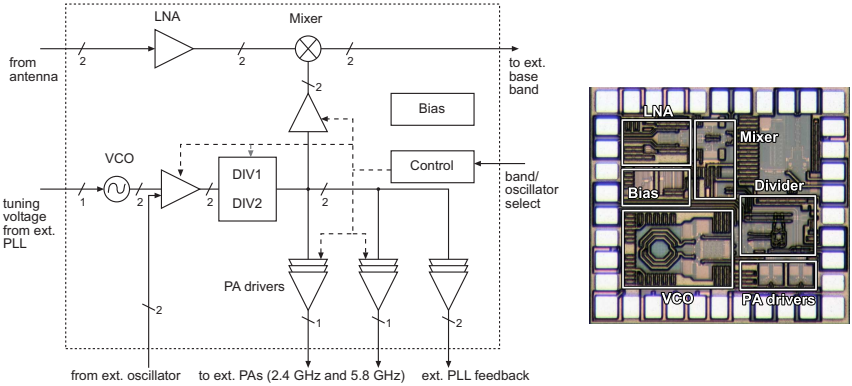

(a) Architecture (b) Micrograph

Figure 4.2: System chip first version, analog front end and oscillator

- Isolated p-well, e.g. to separate grounds of digital and analogue circuits
- nMOS and pMOS transistors with high speed for 1.8 V supply domain or high breakdown voltage for 3.3 V supply domain
- npn bipolar transistors with $f_{\mathrm{T,max}}$ of 60 GHz
- Hyperabrupt junction varactors, MOS varactors and Schottky barrier diodes
- Different types of polysilicon resistors and a back-end-of-line resistor between the first and second metal layer
- metal insulator metal (MIM) capacitors with different dielectrics and capacitances per area

The design strategies and circuits which are presented in the following sections can also be transferred to other semiconductor technologies with similar parameters.

4.3 System Overview

4.3.1 Integrated Front Ends

In the course of this work, three integrated circuits containing FMCW radar front ends were developed, with added features for each subsequent design iteration. All relevant building blocks of the front end chips and the rest of the system will be described in detail in the following sections.

Fig. 4.2 shows the architecture and a micrograph of the initial version of the system chip. Its die area amounts to $1.2 \times 1.1\,\mathrm{mm}^2$. It contains a fully differential receive path, consisting of a LNA and mixer. The base band processing (filter-

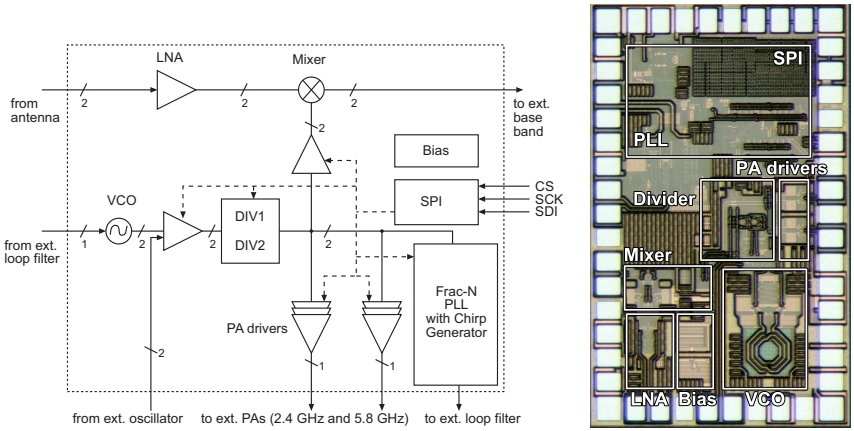

(a) Architecture (b) Micrograph

Figure 4.3: System chip second version, analog front end with PLL

ing, amplification and data conversion) is done off-chip. Furthermore, a VCO is included, which covers the band from approximately 4.8 GHz to 6 GHz. With a switchable divide-by-2, both target ISM bands can be served. It is also possible to switch to an external oscillator. The tuning voltage for the VCO is fed by an external PLL. The buffered and divided LO signal drives the mixer and three output drivers. Two of the output stages are designed to drive single-ended power amplifiers for transmission of the chirp signal, the other driver is used to provide a differential feedback signal to the external PLL. The dividers and drivers can be switched by a simple parallel digital control bus. Lastly, a self-biased proportional to absolute temperature (PTAT) reference current source is included, providing all the reference currents and voltages for the on-chip blocks and eliminating the need for any external bias other than supply voltage.

The second version of the system chip is presented in Fig. 4.3. It occupies an area of $1.8 \times 1.1\,\mathrm{mm}^2$, which is an increase of 50 % to the first version. The analog front end is the same as for the first version. A major added feature is a custom integrated fractional-N PLL, which is capable of generating automatic frequency sweeps. Moreover, the simple digital control from the first version was extended to a serial peripheral interface (SPI) bus. This approach reduces the number of pads, which are necessary for front end and PLL configuration, to only three.

Version three of the system chip is shown in Fig. 4.4. The chip area amounts to $3.15 \times 2.04\,\mathrm{mm}^2$. The LO path, mixer and PLL are similar to the second version.

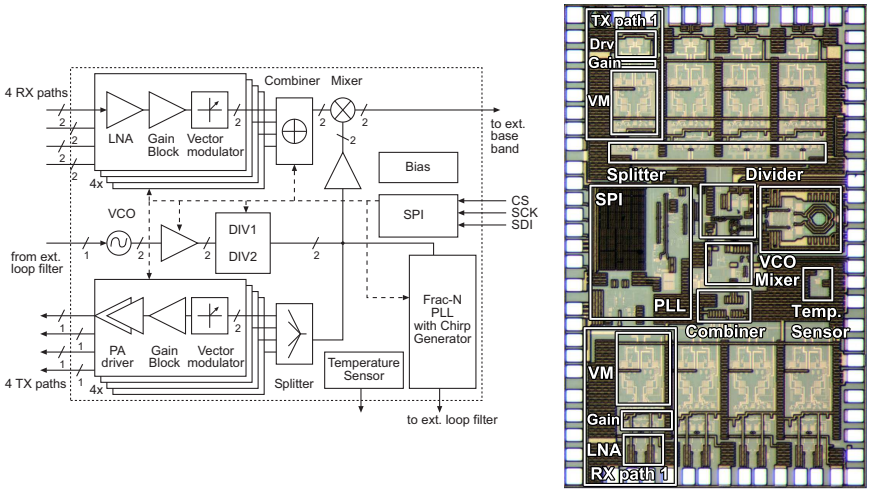

(a) Architecture (b) Micrograph

Figure 4.4: System chip third version, MIMO analog front end with PLL

The main feature of this integrated circuit is the addition of a 4-channel MIMO receive and transmit path. The design of the MIMO-specific components (vector modulators, combiner) was not a focus of this work. The gentle reader may want to refer to the works of *Wagner et al.*, e.g. [WMW+13*, EMW+10*], for further details. Another addition is a temperature sensor with analog output, because during the test of the hybrid system (section 3.7) it was determined, that the distance offset is temperature-dependent.

4.3.2 Complete System Architecture

The complete dual band localization system consists of mobile stations and base stations. Since a secondary radar topology was chosen according to the specifications, the mobile stations only receive signals from the base stations and calculate their own positions. This means that considerable processing power is necessary in the mobiles.

The architecture and a photograph of the developed mobile station are shown in Fig. 4.5. It consists of two connected printed circuit boards (PCBs), where one is the carrier board containing the analog front end and the other is the FPGA board, which performs the necessary digital base band, processing and control

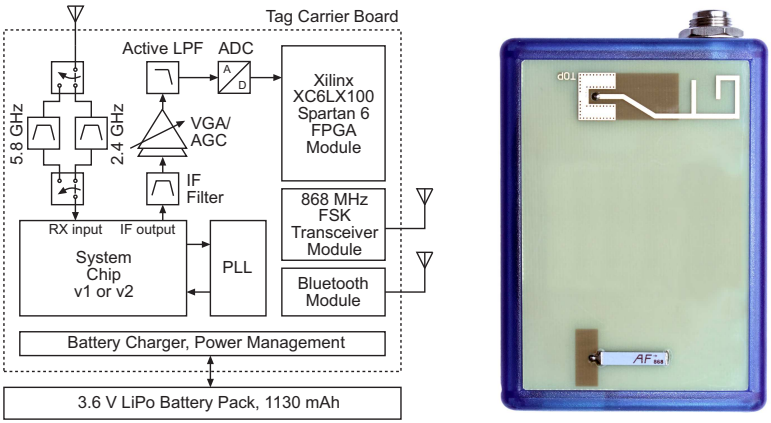

(a) Block Diagram (b) Photograph

Figure 4.5: Mobile tag architecture and photograph, size $65 \times 90 \times 28\,\mathrm{mm}^3$

functions. The analogue front end is designed to use the first or second version of the system chip. The photographed module uses the first version with external PLL. A dual-band receive chain is implemented, containing two switchable band-pass filters for both ISM bands. Furthermore, an IF filter, VGA, and ADC with anti-aliasing filter are added. The digital signal is then processed further in the FPGA using the digital back end described in section 3.5.2. Also the FSK module for communications and protocol handling between the modules as described with the test system is mounted on the carrier board.

To communicate with the FRU of the E-SPONDER system, a bluetooth module is included. Using the serial port profile, the calculated positioning data is transmitted as a text string with a constant update rate and received by the FRU, which can be the smart-phone of a first responder team member. From there, the data is forwarded through the E-SPONDER network. Power supply is provided by a 3.6 V LiPo battery, which is connected to an integrated charge and power management circuit. A battery extension with doubled capacity is also supported to allow a longer running time. It allows the module to be powered and charged by a wall supply. In operational mode with all sub-modules switched on, the tag consumes 1.3 W of electrical power. Most of the power budget is consumed by the FPGA module, which is around 1 W. Using the battery extension and normal operation within the system, the running time of the tag was tested to 2.5 hours.

The developed base station is depicted in Fig. 4.6. It uses the third version

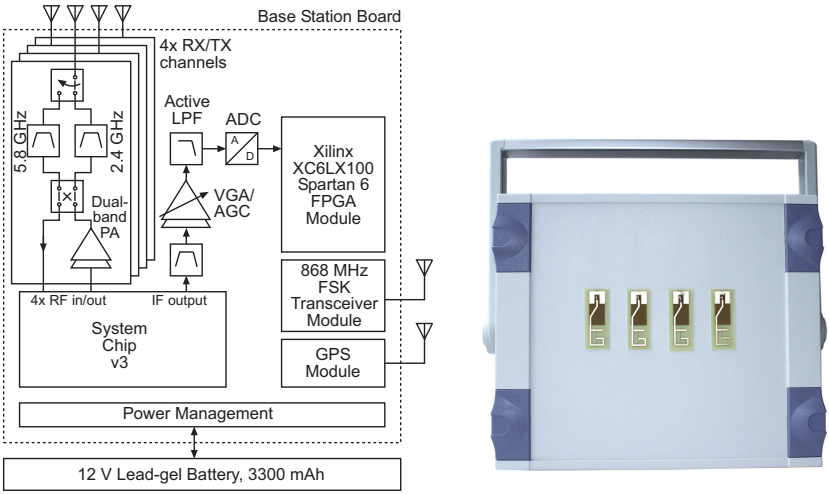

(a) Block Diagram (b) Photograph

Figure 4.6: Base station architecture and photograph, size $235 \times 195 \times 135\,\mathrm{mm}^3$

of the system chip to implement a multi-channel architecture. The front end architecture is similar to the mobile, except it has four channels which are capable of receiving and transmitting. A GPS module is added to provide a global position to the base station which is used to reference the local coordinate frame of the system to a global coordinate frame. As a result, the system can output local and global coordinates, which can be used directly by the E-SPONDER system. The system is powered by a high-capacity 12 V lead battery to provide energy autonomy for a long period. The base station consumes 3.36 W of electrical power when in transmit mode and all channels including power amplifiers are switched on. In normal operation, the running time was tested to at least 8 hours. An inside view of the base station is presented in Fig. 4.7.

The planar monopole antennas on the mobile and base stations for the FMCW front end were reused from [STHW+11]. Originally a design for WLAN applications, its resonances are designed at 2.4 GHz by the upper spiral part of the F-shape and 5.6 GHz by the lower bar. Thus, this antenna can also be easily trimmed to 5.8 GHz by doing pre and post fabrication trimming of the lower bar. The 868 MHz FSK module is connected to an off-the-shelf single SMD ceramic antenna element.

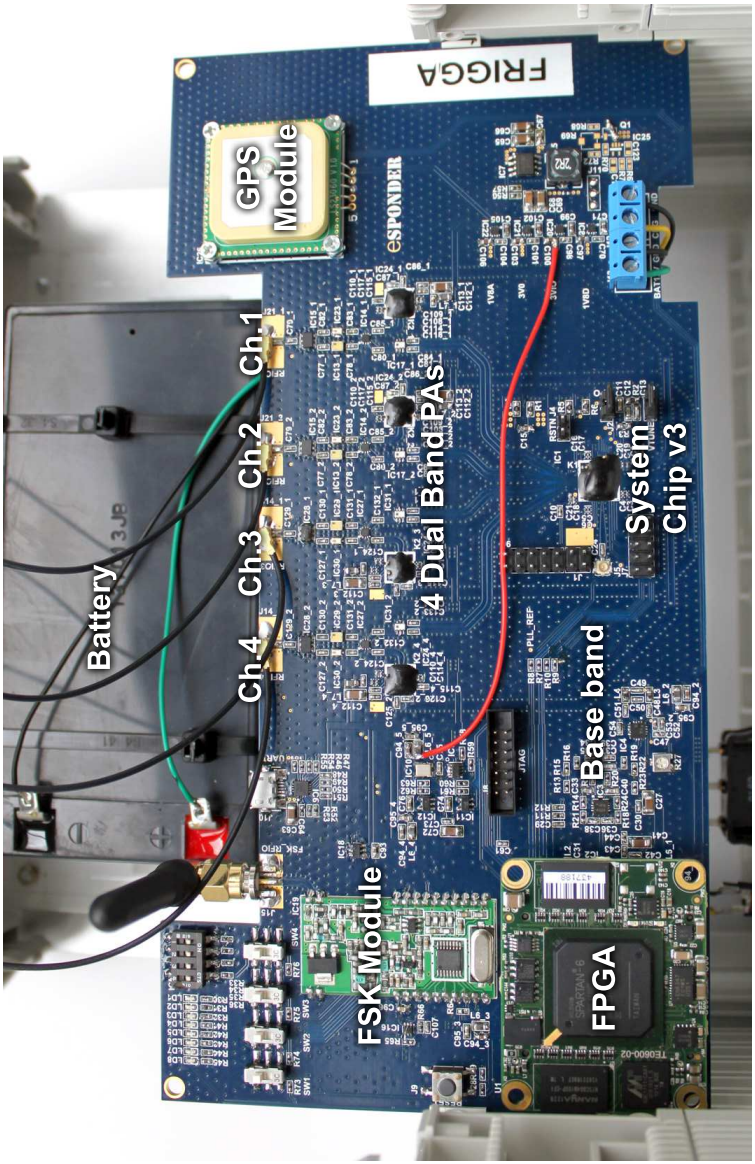

Figure 4.7: Base station inside view

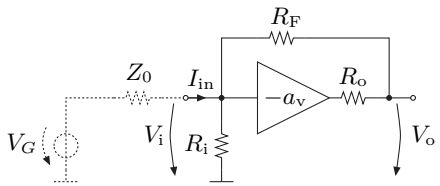

Figure 4.8: Model of amplifier with active matching

4.4 Low-Noise Amplifier and Mixer

4.4.1 Circuit Description

The basic requirements of the front end components LNA and mixer are high gain, low noise figure and suitable input-referred compression point. Furthermore, both ISM bands should be covered with good return loss. To optimize the interface between LNA and mixer and to obtain the characteristics of the complete chain, both blocks were designed and built conjointly. Also, it is beneficial to lay out the circuits differentially to provide robustness against common-mode interferers such as stray signals or power supply variations.

An important design premise was the avoidance of inductors to save chip area which calls for a concept to provide impedance matching to the $Z_0 = 50\,\Omega$ system impedance for both desired ISM bands at the LNA input. This can be done by using a feedback around an inverting amplifier, as modeled in Fig. 4.8. The amplifier is modeled as an ideal dependent voltage source with infinite input resistance and zero output resistance. Resistors R_i, R_o are added to model input and output. Using this prerequisites, the input current can be derived from the nodal equation at the input node, yielding

$$I_{in} - \frac{V_i}{R_i} - \frac{V_i(1 + a_v)}{R_F + R_o} = 0. \tag{4.9}$$

The input resistance is then calculated as

$$R_{in} = \frac{V_i}{I_{in}} = \frac{1}{\frac{1}{R_i} + \frac{1+a_v}{R_F+R_o}}, \tag{4.10}$$

which is a shunt connection between the input resistance and the sum of the feedback and output resistances, scaled by $1 + a_v$.

For the realization of the circuit, a topology using two cascaded differential amplifiers with resistive loads and feedback is used [WME12]. The gain of the chain should be at least 20 dB for the LNA to dominate the noise. It can be set

by selecting the load resistor and the current through the transistor, determining its transconductance g_m. Output resistance should generally be low, but high enough to reach the desired gain without spending too much tail current. A value of around $R_\mathrm{C2} \approx 300\,\Omega$ will be assumed. Usually, the small-signal input resistance is particularly dependent on transistor parameters, e.g. r_BE, which is in the order of $1\,\mathrm{k}\Omega$ for the specified technology and given operating point. Based on these assumptions and using (4.10), the feedback resistor R_F can be calculated, which needs to be set such that $R_\mathrm{in} \overset{!}{=} Z_0$.

$$R_\mathrm{F} = \frac{a_\mathrm{v} r_\mathrm{BE} Z_0 - r_\mathrm{BE}(R_\mathrm{C2} - Z_0) + R_\mathrm{C2} Z_0}{r_\mathrm{BE} - Z_0} \approx 279\,\Omega. \tag{4.11}$$

It is worth noting, that for increasing gain, the feedback resistor also needs to be increased to keep low return loss.

Fig. 4.9(a) shows the schematic of the LNA. The transistor sizes and tail currents were determined after subsequent simulations to provide lowest noise figure. The input pair uses 6 parallel transistors each, having a size of $0.24\,\mu\mathrm{m} \times 10\,\mu\mathrm{m}$. The second differential amplifier also has a local resistive feedback R_F2, which is used to improve gain compression. The overall feedback with R_F sets the input impedance according to the derivation above. Since the open-loop gain of the amplifier is around 22 dB, R_F is increased to $420\,\Omega$. The gain is degraded by about 2 dB because of the feedback, yielding a total gain of 20 dB.

For the mixer, a Gilbert cell has been chosen, which is extended by a multi-tanh structure. The schematic is presented in Fig. 4.9(b). An active mixer topology was selected to increase the gain of the RF chain. The multi-tanh structure helps to keep gain compression low, since it extends the constant g_m region versus input excitation by overlapping multiple shifted g_m versus input voltage curves. The presented hybrid doublet uses two parallel differential amplifiers, which deliberately have offset voltages introduced, on the one hand by the offset resistors R_OF, on the other hand by choosing different areas for the transistors. The gain versus input excitation is very flat, as is the noise, which makes it superior to a purely emitter-degenerated differential amplifier [Gil98]. Simulations show that the mixer stage adds another 6 dB of voltage gain, whereas the noise of the chain is still dominated by the LNA.

Regarding the interface between LNA and mixer, an interesting effect can be exploited. The predominantly capacitive loading of the common-collector stages at the input of the mixer, resulting from the current sources and the large differential pair transistors, leads to a negative, frequency-dependent input resistance. Using simulations, the 1-dB small-signal bandwidth of the LNA alone was determined to approximately 6 GHz, whereas the bandwidth with connected mixer is 11 GHz. This is due to the fact, that the parallel connection of the LNA load resistance with the input resistance of the mixer approaches infinity, when the magnitude

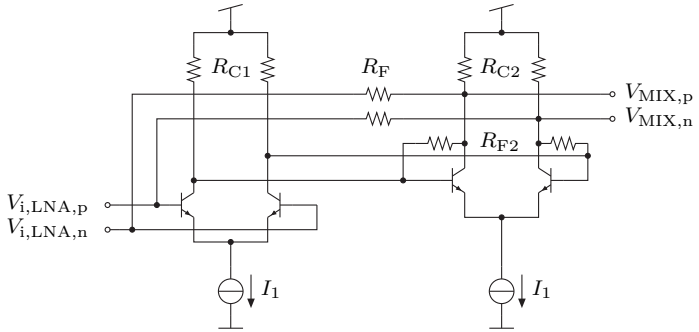

(a) LNA

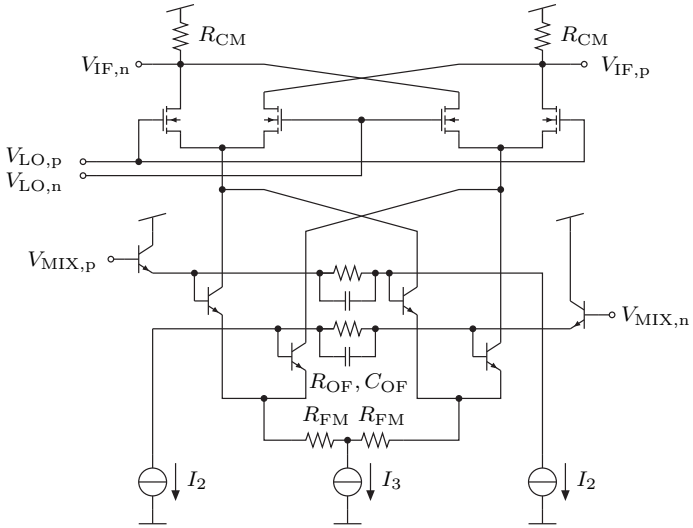

(b) Mixer

$R_{C1} = 755\,\Omega$	$R_{C2} = 309\,\Omega$	$R_F = 420\,\Omega$	$R_{F2} = 254\,\Omega$
$R_{FM} = 17\,\Omega$	$R_{OF} = 65\,\Omega$	$R_{CM} = 112\,\Omega$	$C_{OF} = 3.7\,\text{pF}$
$I_1 = 3\,\text{mA}$	$I_2 = 1.8\,\text{mA}$	$I_3 = 9.6\,\text{mA}$	

Figure 4.9: LNA and mixer schematics

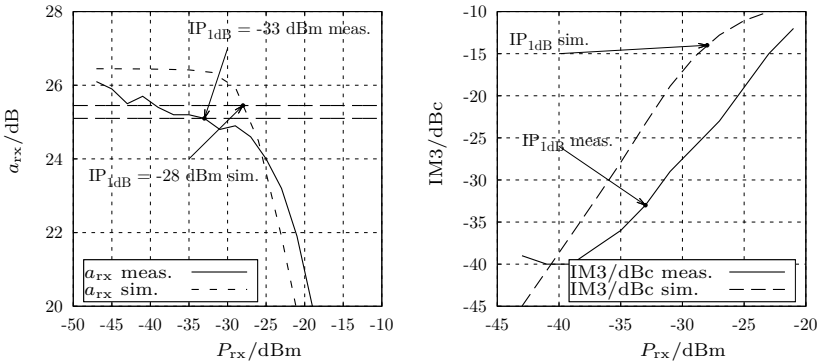

Figure 4.10: Measured and simulated gain and third order intermodulation

of the mixer input resistance is equal to the magnitude of the LNA load, but has opposite sign. According to [TSG10], the equivalent negative resistance calculates as

$$r_{\mathrm{i,mix}}(\omega) = -\frac{2\pi f_{\mathrm{T}}}{\omega^2 C_{\mathrm{L}}}, \tag{4.12}$$

where f_{T} is the transit frequency and C_{L} is the capacitive load at the emitter. Peaking occurs at $\omega = \omega_0$, when $r_{\mathrm{i,mix}} \stackrel{!}{=} -R_{\mathrm{C2}}$, hence

$$\omega_0 = \sqrt{\frac{2\pi f_{\mathrm{T}}}{R_{\mathrm{C2}} C_{\mathrm{L}}}}. \tag{4.13}$$

Using this relation, the capacitive load of the common-collector stage can be tuned, such that peaking occurs at the desired frequency to help enhance the bandwidth of the front end. Of course, this tuning has to be done while considering stability of the circuit at the same time.

4.4.2 Measurement Results

All measurement were carried out with the first version system chip bonded onto a PCB. The complete front end runs with 3 V supply voltage. LNA and mixer are tested together, there is no tap after the amplifier due to the pad-limited design.

Fig. 4.10 shows large signal measurement results, namely voltage gain, compression and intermodulation behaviour. The compression measurement was done at 1 MHz intermediate frequency, using a 5.72 GHz local oscillator and 5.721 GHz for the RF input. The intermodulation distortion measurement uses 900 kHz and

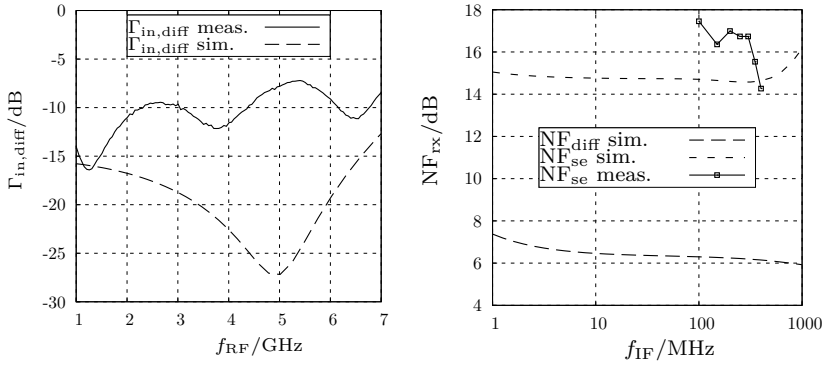

Figure 4.11: Measured and simulated input reflection coefficient and noise figure (single-sideband)

1.1 MHz as intermediate frequencies, down converted from a 5.72 GHz ± 100 kHz RF input. A small difference in gain can be seen between the measurement and simulation results. The simulation shows 1 dB more gain. The measured intermodulation distortion is decreased compared to the simulation. However, in the 1-dB compression point, IM3 ≈ -33 dBc, which is more than sufficient to not affect range resolution of the radar according to section 3.4.2. Furthermore, the measured courses of gain and IM3 for low input powers slightly differ versus simulation, but this is due to difficulties in measuring the very small output signals. Although the results are shown for the 5.8 GHz band, the results are comparable for the 2.4 GHz band. The small-signal unfiltered IF bandwidth was measured to 960 MHz.

The results for the input reflection coefficient and single-sideband noise figure are presented in Fig. 4.11. The input reflection coefficient was measured with the true differential mode of the *Rohde&Schwarz ZVA67* network analyzer. The simulation shows input matching of $\Gamma_{\text{in,diff}} < -10$ dB for the whole bandwidth of 1 GHz to 7 GHz. Return loss increases for higher frequencies, because the capacitive part of the input impedance of the transistor becomes dominant over the active matching using the feedback resistors. The measurement shows some ripple which is probably due to the microstrip traces on the PCB, the SMA edge connectors or the bond interface. Previous tests with a 50 Ω microstrip trace and two SMA edge connectors on a FR4 PCB have shown, that the reflection coefficient only ranges from −15 dB at 1 GHz to −8 dB at 6 GHz, showing a similar rippled course. Therefore, reaching −9.7 dB at 2.4 GHz and −8.3 dB at 5.8 GHz still is a good result considering the realistic test bed.

Stability of the combined LNA and mixer circuit was verified using large signal transient simulations and measurements using a switched harmonic signal to provide a broadband stimulus. No oscillations could be observed.

The noise figure measurement was done with an *Agilent PXA* spectrum analyzer and a *NoiseCom* noise source, which is calibrated starting at 100 MHz, having around 15 dB excess noise ratio (ENR). Therefore, measurements could only be done for intermediate frequencies greater than 100 MHz, for lower frequencies the noise source was not specified. Furthermore, noise figure measurements are possible only in single-ended configuration, since the noise source has only a single output. A balun at the input would degrade the measurement result since it cannot be calibrated using a second-stage correction and it adds attenuation directly after the noise source. The signal chain after the device under test (DUT) consists of a broadband low noise amplifier block to compensate for the drop in gain caused by the 50 Ω termination.

The measurement was carried out in two steps: first, the gain of the DUT was measured. Secondly, the noise figure of the amplifier block and spectrum analyzer was determined. Thirdly, the total noise figure consisting of DUT, amplifier block and spectrum analyzer was measured. Knowing now the total noise figure $\mathrm{NF}_{\mathrm{total}}$, the single-ended power gain $G_{\mathrm{rx,se}}$ of the DUT and the noise figure of the second stage NF_2 consisting of the amplifier block and spectrum analyzer, the noise figure $\mathrm{NF}_{\mathrm{se}}$ of the DUT can be calculated using Friis' noise formula.

$$F_{\mathrm{total}} = F_{\mathrm{se}} + \frac{F_2 - 1}{G_{\mathrm{rx,se}}} \quad \rightarrow \quad F_{\mathrm{se}} = \frac{1 - F_2 + F_{\mathrm{total}} \cdot G_{\mathrm{rx,se}}}{G_{\mathrm{rx,se}}} \tag{4.14}$$

Note that F represents the noise factor and NF the noise figure, which are related by

$$\mathrm{NF} = (10 \log F)\,\mathrm{dB}. \tag{4.15}$$

The measured single-ended noise figure for the LNA and mixer chain is in the region of 14 dB to 17 dB, only slightly higher than in the single-ended simulation, but it matches quite well in the region from 100 MHz to 400 MHz intermediate frequency. Due to the lack of measurement options for the differential case, it has to be deduced that the noise figure in the differential case will also behave similar to the simulation in this case.

4.4.3 Comparison

Table 4.1 shows state-of-the-art combined integrated LNA/mixer front ends. The presented circuit is among those with the highest bandwidths and also largest conversion gain. Unfortunately, the power consumption is also rather high, which is mainly due to the noise requirements (the transistors needed a rather large collector current to reach a good noise figure) and the intended conversion gain of

Ref.	Tech.	Band (GHz)	Gain (dB)	Γ_{in} (dB)	IP_{1dB} (dBm)	IIP_{IM3} (dBm)	NF (dB)	P_{DC} (mW)
[LJS+13*]	180 nm SiGe	0.05-2	3-27	<-10	7	15	5 (SSB)	30
[SHL+11][1]	180 nm CMOS	0.1-1	13.7-19.5	<-9.3	-21	-	3.8-5.3 (DSB)	21
[BKLN08][1]	65 nm CMOS	0.5-7	18	<-10	-	-3	4.5-5.5 (SSB)	16
[AHR07]	90 nm CMOS	0.1-3.85	20	<-10	-12.83	-	8.4-11.5 (SSB)	9.8
[CHWL12]	180 nm CMOS	20.3-25.1	22	<-10	-34.8	-23.8	6-8.49	16.4
This[1]	180 nm SiGe	1-7	28	<-7	-33	-16.5	7 (SSB)	57

1 meas. on PCB

Table 4.1: Comparison with state-of-the-art integrated LNA/mixer circuits

the mixer. The latter could be reduced by half, saving about 20 mW and making the circuit comparable to [LJS+13*]. Compression point and intermodulation intercept point compare well to the other radar transceiver [CHWL12]. In general, it can be stated that the presented receiver is applicable for the use in a FMCW radar system, however for future works, the power consumption should be at least halved.

4.5 Voltage-controlled Oscillator

4.5.1 Design Considerations

To save chip area and power, it would be beneficial to cover both, the 2.4-2.5 GHz and 5.725-5.875 GHz ISM bands with a single VCO. Usually, switched capacitor arrays are used in wideband VCOs [FCL+08, WGS11, Min12] to enhance the tuning range, but the wiring and switches required reduce the quality factor of the varactor and take up space. There are approaches using multiple tuned elements [TKT+08], leading to a more complex circuit, control and design. Also, tunable active inductor VCOs allow a very wide relative tuning range in the order of 100 % [MPY+05, MNR08]. Unfortunately, all those architectures usually show a quite large gain variation over the tuning range, as well as unacceptable phase noise performance. Therefore, a compromise was chosen for this design: The oscillator has to cover the 5.8 GHz band and should also be tunable down to at least 4.8 GHz, reaching the 2.4 GHz band with a standard divide-by-2 circuit.

Furthermore, a linear tuning characteristic with low variations is important to reach stable and predictable behaviour of the PLL in the system over the whole chirp bandwidth, ensuring a good chirp linearity and therefore high accuracy of the radar. The designed VCO uses a differential hyperabrupt varactor to provide continuous frequency tuning without using switches, achieving a wide tuning range while keeping the chip size, complexity and gain variations to a minimum.

The gain of a VCO is the slope of its frequency over tuning voltage characteristic, which is

$$K_{\mathrm{VCO}} = \frac{\partial f(V_{\mathrm{tune}})}{\partial V_{\mathrm{tune}}}. \tag{4.16}$$

The relative gain variation $\varepsilon_{K_{\mathrm{VCO}}}$ can then be defined as the deviation of the actual gain characteristic from an ideal constant gain characteristic. Commonly, it is calculated as [WGS11]

$$\varepsilon_{K_{\mathrm{VCO}}} = \frac{K_{\mathrm{VCO,max}} - K_{\mathrm{VCO,min}}}{K_{\mathrm{VCO,max}} + K_{\mathrm{VCO,min}}}. \tag{4.17}$$

Keeping gain variations of the VCO small helps maintaining the PLL dynamics over the whole system bandwidth. Thereby, the transient response of the loop can be optimized. In FMCW radar systems, where a chirp with greatest possible bandwidth needs to be generated, chirp nonlinearities degrade spatial resolution.

The resonant frequency range of the oscillator can be estimated using

$$f(V_{\mathrm{tune}}) = \frac{1}{2\pi\sqrt{L(C_{\mathrm{var}}(V_{\mathrm{tune}}) + C_{\mathrm{par}})}} \tag{4.18}$$

with $C_{\mathrm{var}}(V_{\mathrm{tune}})$ being the voltage-dependent varactor capacitance and C_{par} the equivalent parasitic capacitance from the wiring, transistors and output load. The dependency of the oscillation frequency from the varactor capacitance as outlined in (4.18) is nonlinear, therefore a matching $C - V$ characteristic of the used varactor is important to minimize the gain variation. A model for estimating the junction capacitance of a reverse-biased hyperabrupt varactor is given as [CB92]

$$C_{\mathrm{var}}(V_{\mathrm{tune}}) = \frac{C_{j0}}{\left(1 - \frac{-V_{\mathrm{tune}}}{V_j}\right)^m}. \tag{4.19}$$

The parameters of the equation can be matched to the hyperabrupt varactor, which is available in the employed IBM SiGe technology, with $C_{j0} \approx 1.69\,\mathrm{pF}$, $V_j \approx 2.5\,\mathrm{V}$ and $m \approx 1.5$. A value of $m > 0.5$ indicates a hyperabrupt junction. Inserting (4.19) in (4.18) yields an estimate for the tuning characteristic of the VCO, which is depicted along with the corresponding gain in Fig. 4.15. The results are discussed in the following sections.

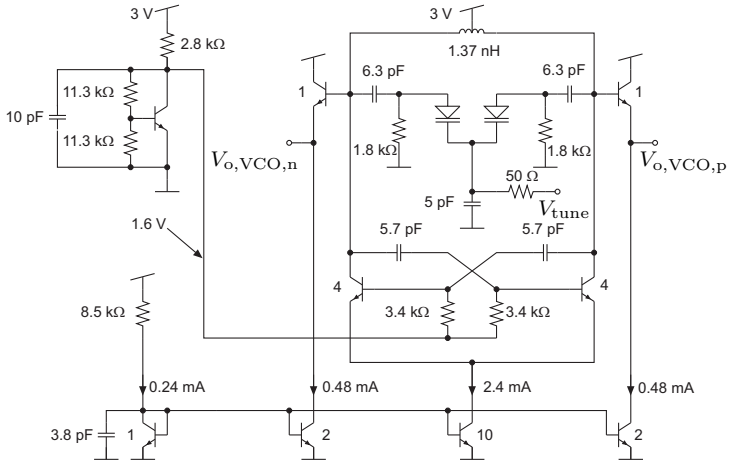

Figure 4.12: VCO core circuit diagram (BJT emitter areas 0.25 µm×2.5 µm, multiplier given)

4.5.2 Circuit Description

Oscillator Core

The VCO core uses a commonly known differential cross-coupled topology with npn bipolar junction transistors. Simulations of different oscillator topologies with real device models showed a slightly better phase noise performance of the cross-coupled oscillator compared to the common-base or common-collector Colpitts topologies.

The schematic and component values are shown in Fig. 4.12. The oscillator tank consists of an inductor with center tap and differential varactor diodes, which form a parallel resonant circuit. The center tap of the symmetric inductor is connected to the supply voltage and is also used to bias the collector of the cross-coupled BJT pair. The varactor diodes are decoupled by large RF blocking capacitors of 6.3 pF from the collector nodes, because they need to be reverse-biased. Therefore, their anodes are biased to ground using a high-ohmic resistor and the cathodes are connected together to form the input for the tuning voltage, including a *RC* low pass filter.

The varactors consist of an array of 16 diodes, each having 2 anodes. It allows for a large capacitance change for a given voltage change. The relative capacitance change of the used varactor is about 3.3:1 (or 1.69 pF to 520 fF absolute) single-ended for a voltage change from 0 to 3 V.

The quality factor Q of a varactor or inductor can be expressed as the ratio of its reactance X to its resistance R.

$$Q = \frac{X}{R} \tag{4.20}$$

For the used varactor, a differential Q of about 15 to 20 was simulated at 5 GHz, depending on the tuning voltage. Since the varactor array is quite large and therefore involves increased wiring effort, the quality factor is slightly lower than in narrowband VCOs, where 20 to 30 is common. On the other hand, the differential Q of the employed inductor was simulated to be 17 at 5 GHz, which is a good value.

The effective inductance L for calculating the oscillation frequency is half of the used differential inductance of 1.37 nH. Simulations showed that $C_{\mathrm{par}} \approx 250\,\mathrm{fF}$ resulting from the wiring and the parasitics of the cross-coupled pair and output buffer transistors. The calculation using the hyperabrupt varactor model from the previous subsection then yields a tuning range from 4.37 GHz to 6.94 GHz with a maximum gain variation of 16 % below 6 GHz and 27 % for the whole bandwidth, which is a promising result and indicates that the varactor is applicable for wideband linear VCOs.

To decouple the tank from the output stage and frequency divider, small common-collector buffers are employed, which add only little parasitic capacitance to the critical collector nodes. The bases of the cross-coupled pair are biased via resistors by a V_{BE} multiplier. Simulations showed that this biasing scheme is advantageous to a simple resistor divider in terms of phase noise.

The tail current sources for the core and output buffers are biased resistively rather than using a transistor current source. Low frequency flicker noise of such a current source would translate into phase noise in the oscillator core, degrading the performance at offset frequencies in the kilohertz range. To face this problem, the transistor widths of the current source could be made very large. However, in order to save area, a small bias resistor provides superior noise performance.

Frequency Divider

The employed frequency divider consists of two cascaded latches in emitter-coupled logic (ECL) architecture. Those latches form a delay flip-flop, where the inverted data output is fed back to the data input, thus halving the applied clock frequency. To allow switching the frequency divider, the buffered oscillator output and the divider output both are open-collector and operate on a common resistive load. Therefore, the divider can be activated and deactivated by switching the tail current sources of the involved differential amplifiers. The divider can also be bypassed completely, saving its contribution of 26 mW to the total power budget.

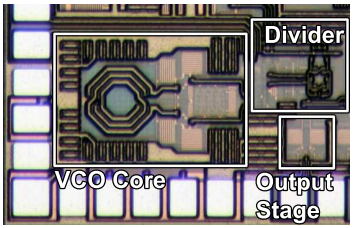

Figure 4.13: VCO chip micrograph

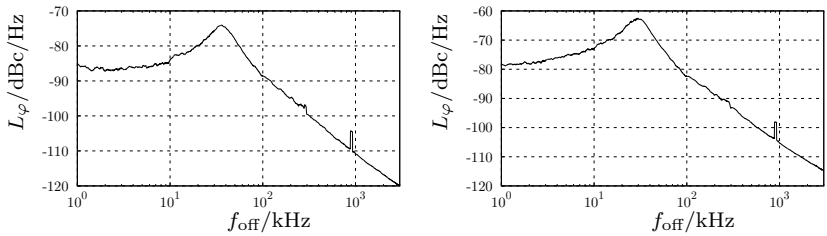

(a) 2.4 GHz (b) 5.725 GHz

Figure 4.14: Measured phase noise plot of the VCO within a PLL with 150 kHz loop bandwidth at 2.4 GHz and 5.725 GHz oscillation frequency

4.5.3 Measurement Results

The VCO was manufactured in an IBM 180 nm SiGe BiCMOS technology with a maximum transit frequency of 60 GHz. Fig. 4.13 shows a chip micrograph of the VCO integrated into the first version transceiver chip together with the frequency divider by 2 and a totem-pole output stage [WWE12]. Its core area amounts to $0.5\times0.4\,\text{mm}^2$, the divider area is $0.3\times0.2\,\text{mm}^2$.

All measurements were done with the transceiver chip bonded onto a PCB. The chip is connected to an external PLL to be able to control the frequency of the VCO. The phase noise measurement was done in the application system and using the PLL, which has 150 kHz loop bandwidth. The result is presented in Fig. 4.14.

Because of the large gain, the oscillation frequency is very susceptible to noise and interference, making phase noise measurements of the free-running oscillator with fixed control voltage inaccurate. Instead, the PLL filters out the interference below 150 kHz to reach a stable frequency output and the measurement then was done using a Rhode&Schwarz FSU-67 spectrum analyzer with phase noise

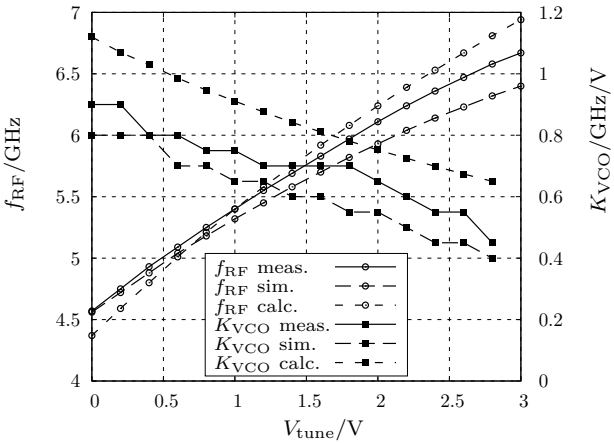

Figure 4.15: Calculated, simulated and measured VCO tuning characteristic and gain

measurement software option. The phase noise at 1 MHz offset from the carrier, which lies out of band of the PLL, amounts to −110 dBc/Hz at 2.4 GHz or −105 dBc/Hz at 5.725 GHz oscillation frequency. Phase noise at offset frequencies below the PLL bandwidth is mainly determined by the other components of the PLL rather than the VCO.

The gain of the oscillator at low tuning voltages is about 900 MHz/V. The gain variation amounts to only 12.5 % from 4.57 GHz up to 6 GHz, which is the frequency range for use in the ISM bands, and 33.3 % for the whole tuning range up to 6.7 GHz. The calculated, measured and simulated tuning curves are shown in Fig. 4.15 along with the gain. It can be seen, that the model calculation gives a good estimate of the oscillation frequency and gain variations to be expected. At low oscillation frequencies up to 6 GHz, the simulated and measured values match well. At higher frequencies, the simulated curve is more flat than the measured one, showing 200 MHz less tuning range. This may be due to the fact, that the used standard parasitic extraction does not include parasitic inductances. Since the hyperabrupt varactor is specified up to 6 V of reverse bias voltage, the frequency could be increased further, e.g. to 7 GHz at 4 V. However, the supply voltage of the system is specified to be 3 V and an additional voltage source would then be needed to supply the PLL charge pump. Besides, the tuning curve becomes flat in the region above 3 V, increasing the gain variation.

Ref.	Tech.	Tuning Range (GHz)	Phase Noise 1 MHz offset (dBc/Hz)	Gain Variation (%)	Core area (mm^2)	Supply power (mW)
[WGS11]	65 nm CMOS	1.51-3.06 (67.8 %)	-115 to -120	49.5	0.39	1
[Min12]	65 nm CMOS	0.75-1.5 (66.7 %)	-125.8	-	0.7	2.25
[MPY+05]	SiGe	1.7-5.2 (101.4 %)	-94 to -103	-	0.5	3.7
[MNR08]	180 nm CMOS	3.8-7.4 (64.3 %)	-75 to -92	-	-	29
This [JWE13a*]	SiGe	4.57-6.69 (37.6 %)	-110 to -105	33.3 12.5 <6 GHz	0.26 with divider	12 VCO 26 divider

Table 4.2: Comparison with state-of-the-art integrated wideband VCOs

4.5.4 Comparison

Table 4.2 compares key parameters of current wideband VCOs with the designed oscillator. There are only some isolated publications of wideband VCOs covering the 4-6 GHz range, mostly using multiple tuned elements or tuned inductors [MPY+05, MNR08]. Gain variations of those types can be in the order of 50 % and above with tuning curves shaped after exponential or tanh functions. Furthermore, phase noise performance is degraded by those approaches. Of the referenced publications, the gain variation of the presented VCO is among the lowest with respect to oscillation frequency and tuning range.

4.6 Phase-locked Loop

4.6.1 System Overview

This section presents a fractional-N PLL for the use in FMCW radar systems. It supports division ratios from 59 to 4091 with a maximum RF input frequency of 7 GHz, covering the 2.39 GHz to 3.28 GHz and 4.79 GHz to 6.55 GHz bands using the previously described dual-band VCO with a frequency resolution of 0.6 Hz. This corresponds to a large relative bandwidth of more than 31 %. Reference spur levels are lower than −65 dBc while phase noise is at −103 dBc/Hz at 1 MHz offset frequency. A key feature for radar applications is the automatic chirp waveform generation. The complete circuit including the VCO consumes less than 122 mW.

The task of the PLL in a FMCW radar system is to generate the chirp. It translates a stable, but low reference frequency, e.g. from a crystal, to an unstable

high frequency oscillator, typically a VCO. To achieve good radar performance, the PLL has to be optimized for large possible chirp bandwidth, gradient and linearity. Range resolution of a FMCW radar system increases with increasing chirp bandwidth. Furthermore, it should be able to handle a large frequency range at the RF input to allow operation in several bands. In-band phase noise and spurious emissions must be low. Discrete frequency steps for chirp generation have to be small enough, such that the resulting chirp after filtering in the loop is smooth and linearity errors are reduced. Consequentially, the PLL has to use a fractional-N frequency divider. The divider has to be programmable to select different channels and include automatic frequency stepping to generate the chirp. For the use in LPS, the coverage range of the system should be high, which calls for using frequency bands below 10 GHz, namely the ISM bands targeted in this thesis.

There are FMCW PLLs available which are designed for the use in radar distance sensors and concentrate on operation in one band, mostly around 77 GHz [MSM+12, NFF+13] with relative bandwidths below 10 %. Some sub-10 GHz ISM wide-band PLLs have also been presented primarily for the use in communications systems [BSL07, RDCR05], which show good phase noise performance, but are not optimized for bandwidth, small frequency steps or modulation capabilities like chirp generation. This section therefore presents a design combining a wide-band architecture with chirp generation capability suitable for FMCW LPS. Furthermore, special attention has to be paid to isolation between digital and analogue blocks, which is also investigated in the following subsections.

A block diagram is shown in Fig. 4.16. It is a basic charge pump PLL architecture, which is commonly used in communications today. The reference frequency f_{ref} and the frequency at the divider output f_{div} are compared by a phase frequency detector, which generates pulses proportional to the phase difference between the two input signals. If f_{div} lags f_{ref}, UP pulses are generated and current is injected into the loop filter, increasing the tuning voltage V_{tune} and thus frequency f_{RF}. If f_{div} leads f_{ref}, DN pulses are generated and consequently f_{RF} is decreased.

4.6.2 Frequency Divider Overview

The frequency divider is one of the most complex blocks in the system. It consists of a full-custom dual-modulus prescaler running at f_{RF}, semi-custom integer divider running at the divided RF clock f_{pre} and sigma delta modulator (SDM). The programmable prescaler divides the RF frequency before the integer divider. The integer divider is implemented with digital standard cells. With the specified semiconductor technology, the maximum frequency of a synthesized divider was determined to approximately 400 MHz.

Using a programmable modulus P in the prescaler enables the PLL to process

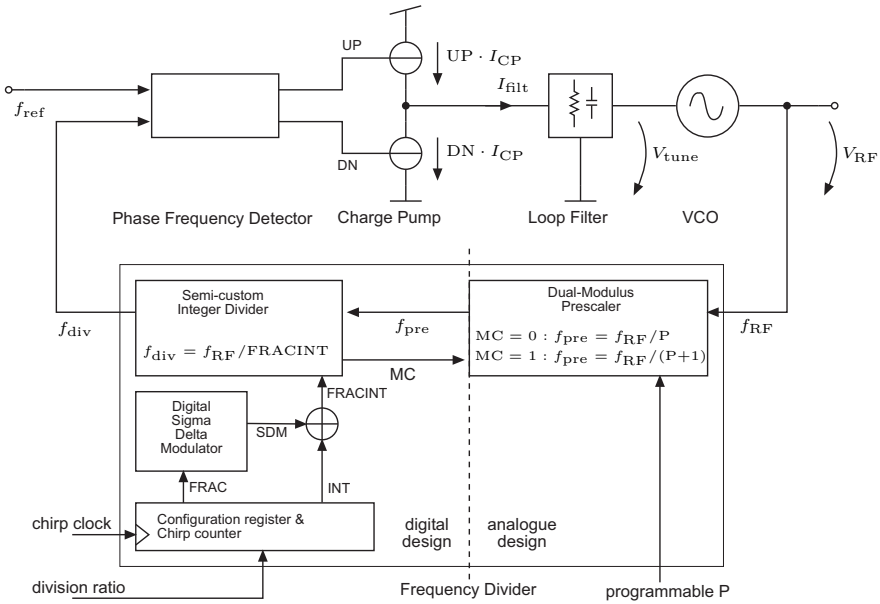

Figure 4.16: PLL block diagram

RF frequencies of both ISM bands. The modulus control signal MC controlled by the integer divider is used to switch the division ratio of the prescaler between P and $P+1$. The prescaler output frequency then results in

$$f_{\mathrm{pre}} = \begin{cases} f_{\mathrm{RF}}/P & \mathrm{MC} = 0 \\ f_{\mathrm{RF}}/(P+1) & \mathrm{MC} = 1 \end{cases} . \tag{4.21}$$

Any integer division ratio can be reached by dividing a certain number of cycles of f_{pre} by P and another number by $P+1$, which is done by the integer divider through switching of the MC signal. An in-depth explanation is presented in section 4.6.4. To extend the divider to fractional operation, a SDM is used to map the fractional frequency control word FRAC to a number stream, whose average over time lies between 0 and 1. The SDM value is then added to the integer part of the frequency control word INT, resulting in FRACINT, which represents the total division ratio. Consequentially, the division ratio is changing with every cycle, providing the fractional value through averaging in the loop. The output of the frequency divider block which is fed to the phase frequency

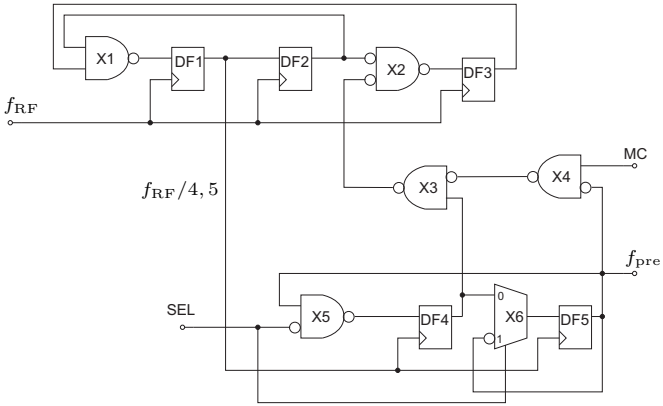

Figure 4.17: Dual modulus prescaler

detector then calculates as

$$f_{\mathrm{div}} = f_{\mathrm{RF}}/\mathrm{FRACINT}. \tag{4.22}$$

Two basic chirp waveforms (triangular or sawtooth-shaped) can be programmed using an externally clocked up/down counter, which increments or decrements FRACINT by a previously programmed value, allowing different chirp gradients. Furthermore, by using an external clock for this counter, synchronization issues with the rest of the radar system can be avoided, since the start of the chirp becomes deterministic.

4.6.3 Dual-Modulus Prescaler

A schematic of the dual-modulus prescaler is depicted in Fig. 4.17. Since this block has to process high frequencies directly from the VCO, standard CMOS gates cannot be used with the specified technology. Thus, it is implemented with custom-designed ECL gates using bipolar transistors. Furthermore, all signals are laid out differentially.

The prescaler is an extension of the design from [KOH+97] and it is composed of two parts: a synchronous 4/5 divider based on a Johnson counter consisting of the flip-flops DF1, DF2 and DF3 and a switchable divide-by-2 or divide-by-4 using DF4 and DF5.

The Johnson counter includes a pulse stretcher circuit consisting of X2 and DF3, which is controlled by the modulus control signal MC. If enabled, the chain divides f_{RF} by 5, otherwise by 4. The divided frequency is then passed to the

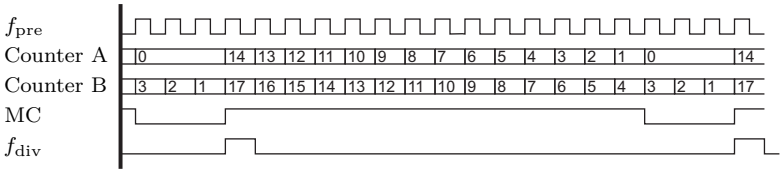

Figure 4.18: Integer-N divider with two counters waveform

second divider circuit represented by DF4 and DF5. The SEL signal determines the modulus, which can be $P = \{8, 16\}$. When the SEL signal is set to 0, the multiplexer X6 connects DF4 and DF5, forming a divide-by-4 circuit. The lower divider is also connected to the pulse stretcher via X3 and X4, such that the total division factors can be 8, 9, 16 or 17, depending on SEL and MC. Consequently,

$$P = \begin{cases} 16 & \text{SEL} = 0 \\ 8 & \text{SEL} = 1 \end{cases} . \tag{4.23}$$

The output signal f_{pre} is fed via an ECL-to-CMOS level shifter to the CMOS semi-custom part of the frequency divider.

4.6.4 Pulse-Swallow Counter

The pulse-swallow counter is a basic form to implement an integer-N divider. It consists of two down-counters, A and B, which are clocked by f_{pre}. Both counters can be pre-programmed with a starting value. Counter A has a smaller bit width than counter B. An example timing diagram is shown in Fig. 4.18. In the example, counter A is loaded with $A = 14$, counter B is loaded with $B = 17$. Both counters start counting down simultaneously. When counter A reaches zero, the MC signal is reset, switching the prescaler to P division ratio. Otherwise MC stays set, corresponding to a division ratio of $P+1$ in the prescaler. When counter B reaches one, both counters are reset to their pre-programmed values and the cycle starts again. Furthermore, a pulse on f_{div} is generated, which represents the divided frequency to be fed to the phase detector. In this context it also becomes clear, that it is advantageous to implement the counters as down counters. When the counters have finished a cycle, a comparison with a fixed value can be done (zero or one), thus simplifying the needed comparator and increasing possible clock frequency of the divider.

Related to the example, it means that the prescaler divides by $P+1$ for 14 cycles and by P for 3 cycles. Assuming $P = 16$, the division ratio of the whole frequency

divider would be 286. Thus, in general, the division ratio N is calculated as

$$N = (B - A) \cdot P + A \cdot (P + 1) = B \cdot P + A. \tag{4.24}$$

There is a lower bound for N, which is of practical relevance. For the pulse-swallow division principle to work, it is required that $B \geq A$. When contiguous division ratios are desired, the minimum value for B is limited to $P - 1$. Thus, minimum N is reached when B equals $P - 1$ and $A = 0$. Hence,

$$N \geq P \cdot (P - 1). \tag{4.25}$$

Starting from the lower limit, all achievable division ratios are contiguous. This condition is required for the SDM principle to work, which is described in the following section. N is upper bounded only by the implementable bit width of both counters.

The presented implementation uses a 12 bit frequency control word for the integer divider. The lower 4 bit are mapped to counter A, the remaining upper 8 bit to counter B. The minimum and maximum integer division ratios are 56 and 2055 for $P = 8$ and 240 and 4095 for $P = 16$.

4.6.5 Sigma Delta Modulator

Sigma delta modulation for the use in fractional-N frequency synthesis was first published by [RCK93]. Since then, several enhanced architectures have been presented, including the now popular all-digital multi-stage noise shaping (MASH) SDM with efficient dithering [GDGAFVM10].

The principle of fractional-N division is shown in Fig. 4.19 with the help of another example timing diagram. Compared to Fig. 4.18, the scale is increased to show several cycles of f_{div}. The counters A and B are only plotted with their pre-programmed values A and B. Furthermore, the modulus control signal MC, the set integer division ratio INT, the SDM output and the summation of both, FRACINT, are plotted. It can be seen, that the SDM adds a stream of signed numbers to INT, changing the values A and B of the pulse-swallow counter with every cycle of f_{div}. This is the reason why the SDM needs contiguous division ratios in the integer divider to work properly. The SDM output follows a pseudo-random sequence with a certain run length, depending on its order and the fractional frequency control word FRAC. The average of the SDM sequence is equal to $\text{FRAC}/2^m$, with the modulus m. Thus the frequency step Δf of the PLL calculates as

$$\Delta f = \frac{f_{\text{ref}}}{2^m}. \tag{4.26}$$

To achieve fine frequency stepping, a large modulus is necessary.

In the case of the example, the sequence consists of $(-3, 2, -1, 3, -3, 1, 0, 3)$.

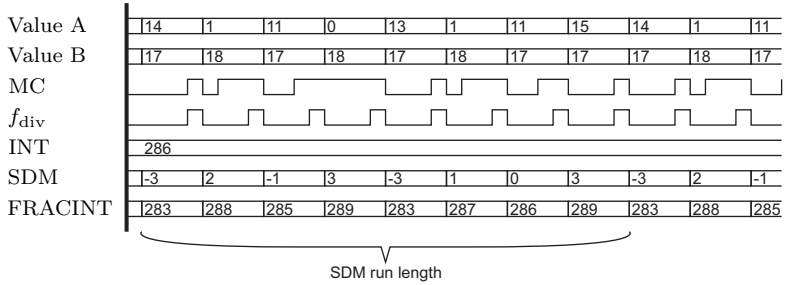

Figure 4.19: Fractional-N SDM divider waveform

The run length is 8, thus the sequence averages to 0.25. As a result, FRACINT averages to 286.25, implementing a fractional division ratio. The fact that the sequence is pseudo-random and, if long enough, approximately aperiodic, has the advantage that the generation of spurious frequencies is suppressed [Cra08].

The chosen three-stage MASH SDM is presented in Fig. 4.20. It consists of three cascaded m bit accumulators, forming the summation stage, and a differentiator stage using the overflow bits from the accumulators as inputs. Annotations in the differentiator stage indicate the values, that can occur at that particular net. The output bit width o is three, which is equal to the number of accumulator stages. The output is signed and represents the number added to the integer division ratio with every clock cycle. The block at the output encodes the 8 levels produced by the modulator (-3 to 4 with a length of 3 bit) to a standard 4 bit signed two's complement number. It should be noted, that the minimum division ratio calculated in (4.25) increases by the magnitude of the smallest number added by the SDM.

The critical path of a digital circuit is the path with the longest latency from input to output. The design goal is to reduce its length to allow clocking the circuit at higher frequencies. A common method to achieve this goal is to apply pipelining to the circuit. The process of pipelining adds registers to a circuit, such that the circuit is divided into different processing stages, hence cutting through the critical path. When data is transferred from one stage to the next, new data can already be processed in the previous stage, resulting in a significant speed-up through parallelization. However, it has to be noted that the actual output is delayed by one clock cycle for every added stage.

Using plain unpipelined accumulators by describing just a summation in *Verilog* the length of the critical path increases with the modulus m. Furthermore, as shown in Fig. 4.20, the direct path through the differentiation stage adds to the critical path since it contains no registers. Pipelining the accumulators is a lengthy

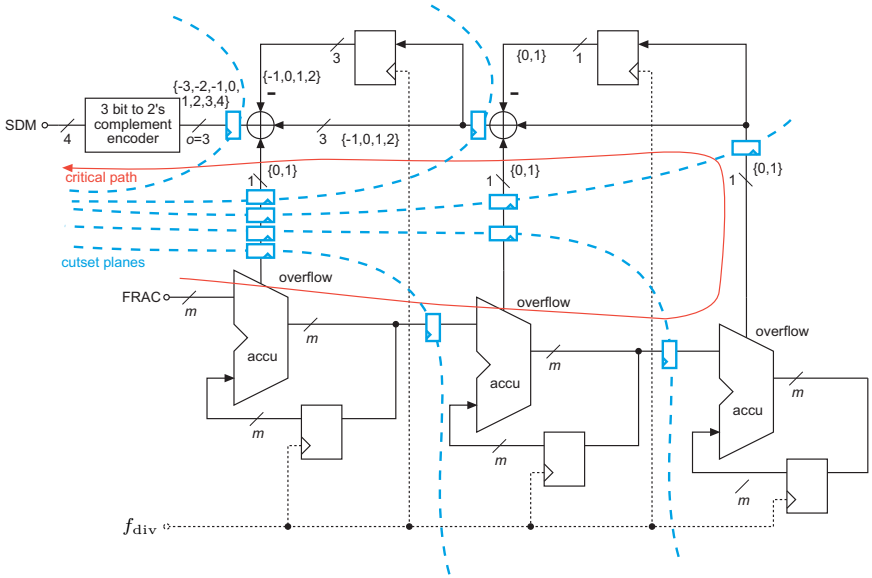

Figure 4.20: MASH 1-1-1 sigma delta modulator with critical path and cutset pipelining

process, since they would have to be custom-built and the delayed output would have to be considered in the remaining circuit. As a compromise, everything but the accumulators is pipelined, which still allows a significant increase of the clock frequency, while decreasing design time.

Pipelining can be done by using the cutset rule, which uses a directed graph representation of the circuit [Kha11]. In case of a pure feed-forward network as the SDM without the accumulators the rule states, that the graph can be cut by cutset planes under the condition that every signal path has to point in the same direction when cut by a plane. At every point where the plane cuts an edge of the graph, a register is added and the outputs of the graph are delayed by one clock cycle. The cutset planes are also sketched in Fig. 4.20. By adding five cutset planes and 11 registers, the circuit is fully pipelined. The critical path is reduced to only one summation operation.

The presented design uses accumulators with $m = 25$ bit, reaching $\Delta f \approx 0.6$ Hz. The SDM is clocked by f_{div}. Due to pipelining it can be clocked with frequencies of more than 30 MHz, even though the modulus is very large. Since the SDM output ranges from -3 to 4, minimum and maximum division ratios have to be adapted.

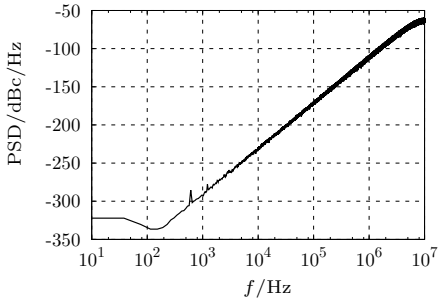

Figure 4.21: Power spectral density of SDM output sequence for input $1/2^{25}$

They reduce to 59 and 2043 for $P = 8$ and 243 and 4091 for $P = 16$. Furthermore, dithering is applied as suggested by [GDGAFVM10]. Thus, the least significant bits in the second and third accumulator are replaced by a pseudo-random bit stream from a linear feedback shift register. Using this architecture avoids the generation of spurious frequencies for certain SDM input words, which would otherwise result in short sequence lengths.

The simulated power spectral density of the SDM output sequence for the input word corresponding to $1/2^{25}$ is plotted in Fig. 4.21. It depicts the wanted noise shaping, shifting the SDM quantization noise towards high frequencies with a slope of 60 dB per decade, corresponding to a third order modulator. Moreover, only two very small spurious tones around 1 kHz can be observed.

4.6.6 Phase-Frequency Detector

As phase frequency detector (PFD), the basic architecture consisting of two flip flops as shown in Fig. 4.22 is used [Raz11]. A delay of around 3 ns is added to the reset line of both flip flops. Without the delay, in the locked state when f_{ref} and f_{div} are equal, the detector would produce very narrow pulses at its UP and DN outputs, which may not be processed correctly by the following gates in the charge pump. This would result in a lower open-loop gain of the PLL and therefore alter loop dynamics. The delay shifts the transfer characteristic of the PFD away from its dead zone.

4.6.7 Charge Pump

Overview

This subsection presents a compensated charge pump for the use in PLLs, which reaches several of the desired design goals for this type of circuit: The measured

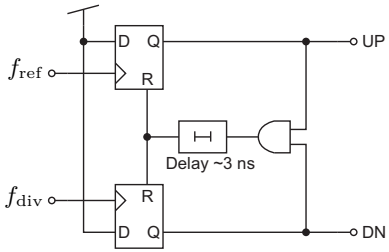

Figure 4.22: Basic flip-flop-based phase/frequency detector

mismatch between source and sink currents is below 2.1 % for a large output voltage headroom of 83.3 % of the supply, while still having a high output resistance of 140 kΩ. This behavior is reached with a novel dual compensation method.

The task of the charge pump in a PLL is to inject or remove current from the loop filter to implement integrating behavior. One of the major challenges of the design is the minimization of current mismatch between the injected and removed currents, i.e. current sink and current source. Mismatch will eventually lead to static phase offsets and reference spurs, because the loop is periodically trying to equalize the offset.

Another design issue, especially in wide band PLLs, is the output voltage headroom of the current sources used to implement the charge pump. To achieve the largest possible frequency range, the output voltage ideally has to range from ground to the supply rail to make maximum use of the oscillator's tuning range, while still maintaining current source behavior and current constancy, i.e. high output resistance, and low current mismatch between source and sink.

The basic compensation method used in literature uses one operational amplifier comparing the reference potential with the output potential and regulating either source or sink [LJC+00]. This approach reduces mismatch, but still suffers from the current variation versus output voltage. Another approach uses adaptive body biasing [LSJH12], which may pose a problem when the charge pump has to be isolated from switching noise in a separate well. A dual compensation method was presented in [HKJ09] showing current mismatch below 3 % with 67 % usable output swing, but the design was only verified by simulations. In [JB13], a very good source and sink current matching is reached, however, the output resistance is low.

The charge pump presented in this thesis uses a novel compensation method employing three rail-to-rail operational amplifiers to compensate for current mismatch. Furthermore, a high output resistance is achieved without using cascode current mirrors leading to a large output dynamic range.

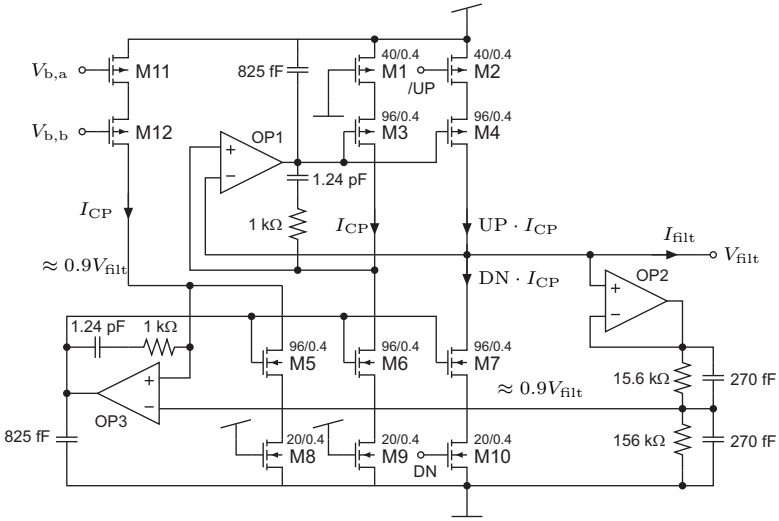

Figure 4.23: High-swing charge pump schematic (transistor sizes given in µm)

Circuit Design

The schematic of the proposed charge pump is presented in Fig. 4.23. The schematic of the employed operational amplifier is shown in Fig. 4.24.

The amplifier is based on a design presented in [Hui11]. The input stage is rail-to-rail and keeps a constant transconductance versus excitation by current source saturation control. It uses two main current sources with 40 µA and two compensation current sources with 20 µA, such that the total tail current at any input voltage level equals 20 µA and the transconductance is kept constant. Using maximum headroom for voltage sensing in the regulation loops within the charge pump also yields maximum headroom for the charge pump output voltage.

The charge pump uses two regulation loops, one for the PMOS current source consisting of M3 and M4 and the other for the NMOS current sink, composed of M5, M6 and M7. Amplifier OP1 provides the well-known basic mismatch compensation method by equalizing the drain potentials of the reference branch M3, M6 carrying I_{CP} and the output branch with the switched current through control of the PMOS current mirror gate bias.

However, there is another source of mismatch, which is the difference between the drain potentials of the reference branch and the input branch, where I_{CP} is fed to M5. Amplifier OP3 is used to equalize those potentials. The problem here is,

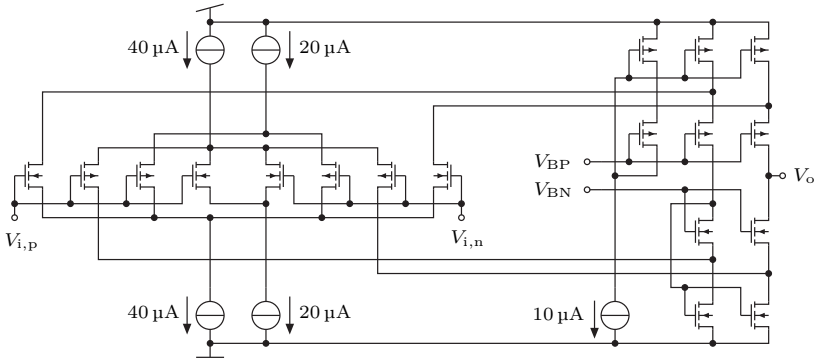

Figure 4.24: Rail-to-rail input operational amplifier

that for rising output voltage, the potential at the reference input would equally rise, thus eventually cutting off the source M11, M12 delivering I_{CP}.

To solve this problem, amplifier OP2 buffers the output voltage of the charge pump and the following voltage divider reduces it to about 90 %. This reduced voltage is now used for the regulation of the input branch, leaving a minimum, but sufficient headroom of 10 % of the supply voltage for the cascode current mirror M11 and M12 delivering I_{CP}, while still keeping the drain potentials of M3, M6 and M4, M7 close enough to avoid a large current mismatch.

Another advantage of regulating both the source and sink is that the output resistance of the charge pump increases and therefore dependency of the absolute current value on the output potential decreases. The common way to achieve this would be the implementation of cascode current mirrors, but those would in turn reduce the voltage headroom.

Switching of the currents is achieved by transistors M2 and M10 in series with the output current source and sink. To keep variations low, dummy versions of the switching transistors M1, M8 and M9 with fixed gate voltage are added to the reference branch and input branch. It is worth noting, that the presented compensation method even works when using short channel devices for the current sources to achieve high switching speeds, since the regulation loop equalizes any nonidealities.

A major concern when designing such control loops is stability. Since the design involves two concurrent loops, stability investigations using Nyquist's stability criterion and examining phase margin are not meaningful. Hence, stability was investigated using transient simulations. A pulse source was connected to the output generating a voltage step. Then, both loops were examined for ringing or

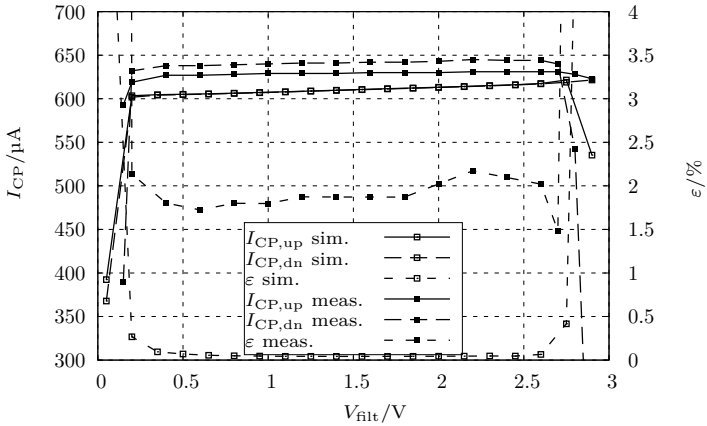

Figure 4.25: Measured and simulated source and sink current and mismatch

excessive overshoot. The Miller compensation networks composed by the series connection of 1 kΩ and 1.24 pF around OP1 and OP2 from the output to the positive input were then optimized accordingly.

Measurement

The PLL can be configured to disconnect the phase detector inputs from the loop and connect it to digital pads. On this basis, it is possible to test the charge pump separated from the rest of the system.

The measured and simulated source and sink currents $I_{CP,up}$ and $I_{CP,dn}$ together with the percentaged mismatch ε are plotted in Fig. 4.25. The nominal current was set to $I_{CP} = 600\,\mu A$. The measurement shows an increase of about 30 µA, which results from the limited accuracy and positive temperature coefficient of the used 10 µA reference current source. The measured current characteristic is very flat versus output voltage indicating a high output resistance of around 140 kΩ.

The measured current mismatch stays below 2.1 % for an output voltage range of 0.2 V to 2.7 V, which is 83.3 % of the 3 V supply. Since the simulation shows a mismatch below 0.5 % for this range, it can be concluded that mismatches in the layout of the circuit are causing the higher error, especially ones leading to current mirror transistor mismatch or offset voltages in the operational amplifiers. Table 4.3 compares the results of the designed circuit to recent publications.

Ref.	CMOS Tech. (nm)	Current mismatch (%)	Voltage range (V,%)	Supply voltage (V)
[LSJH12][1]	180	≤ 0.9	0.2-1 66.6	1.2
[HKJ09][1]	130	≤ 1.7	0.2-1 66.6	1.2
[JB13][1]	130	[2]≤ 1	[2]0.1-0.48 76	0.5
This [JWE14*]	180	≤ 2.1	0.2-2.7 83.3	3

1 simulated
2 estimated

Table 4.3: State-of-the-art compensated PLL charge pumps

4.6.8 Isolation Concept

Since this PLL is a mixed-signal design containing sensitive analogue blocks like charge pump and VCO together with a digital frequency divider on a single chip, an isolation concept has to be devised. It was decided to place the charge pump and digital dividers into separate isolated p-wells, which allows isolating their grounds from each other and from the VCO. The different grounds are then connected off-chip to a low-impedance ground plane. This prevents switching noise from entering the analogue blocks, which would eventually lead to increased spur and noise level. This procedure however brings up the problem of crossing with signals between circuits with different grounds.

The key to solving this problem is to sense the signals always differentially on the receiving side and rejecting the common-mode part. The proposed circuit to translate from CMOS to ECL signals is shown in Fig. 4.26. The pseudo-differential CMOS input signal is buffered by inverters and reduced in swing by the resistor network to accommodate to the following differential pair stage. High-frequency common mode disturbances are shunted to ground by the capacitor. The differential amplifier buffers the signal again and translates the levels to ECL for the prescaler. This circuit is used to translate the SEL and MC signals.

The circuit translating from ECL to CMOS is presented in Fig. 4.27. It consists of a differential pair input stage, followed by a common-drain stage as level shifter and two CMOS inverters used for signal shaping. The voltage at the input of the CMOS inverters has to be set such that they are always biased in the vicinity of their switching threshold. Hence, they will amplify the still small signal swing from the differential amplifier. To set the switching threshold to the desired value, e.g. DVDD/2, one half of the input stage is replicated and a regulation loop is

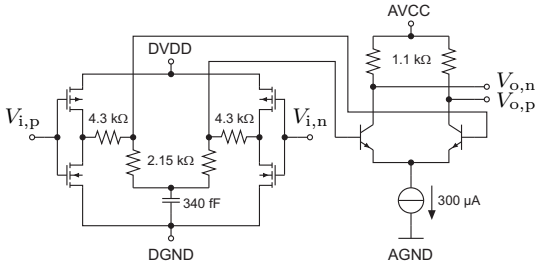

Figure 4.26: CMOS to ECL converter

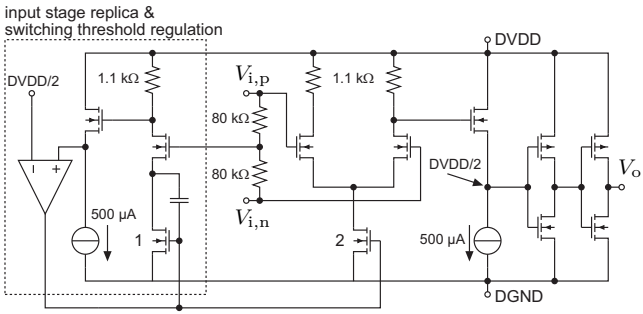

Figure 4.27: ECL to CMOS converter

added, which sets the tail current of the replica and the input stage to achieve DVDD/2 also at the inverter inputs. The circuit works at frequencies higher than 400 MHz and is therefore used to translate the prescaled clock f_{pre}.

4.6.9 Loop Filter

A passive third-order loop filter as printed in Fig. 4.28(a) was chosen and implemented off-chip for increased flexibility. According to the system specifications, the loop bandwidth has to be set to more than 50 kHz. To increase safety margin and reach a good chirp linearity even with fast consecutive chirps, a bandwidth of 130 kHz is set. The charge pump was designed for a nominal current of $I_{\mathrm{CP}} = 600\,\mu\mathrm{A}$. Furthermore, VCO gain is assumed to be $K_{\mathrm{VCO}} \approx 700\,\mathrm{MHz/V}$. A comprehensive guide to calculating the loop filter elements under the condition of maximum phase margin at minimum settling time is provided by [Ihl13]. The calculated loop filter values are shown in Fig. 4.28(b).

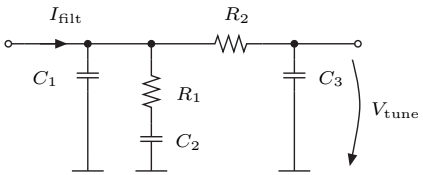

(a) Schematic

Parameter	Value
f_{loop}	130 kHz
φ_{m}	45°
C_1	470 pF
C_2	6.2 nF
C_3	130 pF
R_1	590 Ω
R_2	2.2 kΩ

(b) Parameters

Figure 4.28: Passive third-order loop filter

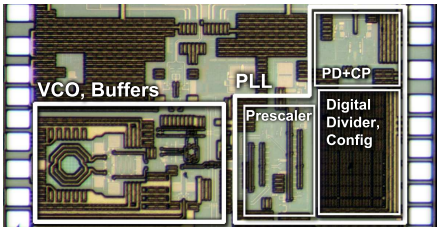

Figure 4.29: PLL and VCO micrograph, PLL area amounts to 0.65 mm^2.

4.6.10 Measurement Results

The PLL was measured in-system bonded onto a circuit board. A micrograph of all involved blocks is presented in Fig. 4.29. The area of the PLL without VCO and buffers amounts to 0.65 mm^2.

Fig. 4.30 shows the phase noise in the two ISM bands. The reference source was a signal generator with −120 dBc/Hz. In-band phase noise is less than −75 dBc/Hz and is dominated by the loop filter, PFD and charge pump. Out-of-band phase noise is below −103 dBc/Hz at 1 MHz offset for both bands, which is about 5 dB worse than that of the VCO alone, indicating a small contribution from the SDM.

The spectral performance is shown in Fig. 4.31 and was recorded with a real-time spectrum analyzer. Due to the large modulus of the SDM and dithering, fractional spurs fade into broadband noise. There are some spots with slightly increased signal power at 5 MHz, 10 MHz and 20 MHz offsets, indicating two fractional spurs at −49 dBc and −58 dBc and a reference spur at −69 dBc for the 5.725 GHz carrier. For the 2.4 GHz band, the spurs are less prominent.

The modulation capabilities were verified and the measured tuning voltages

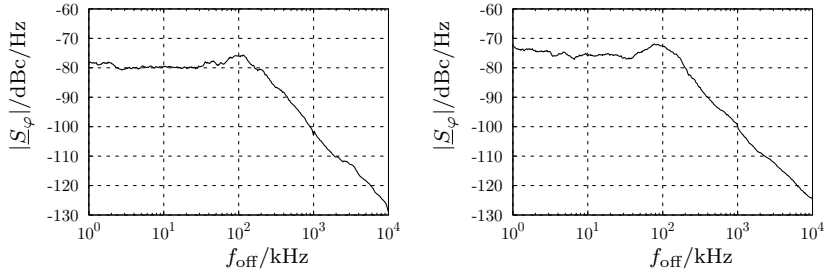

(a) 2.4 GHz (b) 5.725 GHz

Figure 4.30: Measured phase noise of the PLL in the two bands

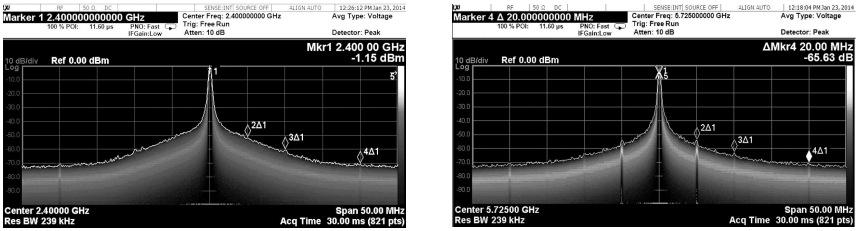

1	2.4 GHz	−1.15 dBm
2Δ1	5 MHz	−50.71 dBc
3Δ1	10 MHz	−59.43 dBc
4Δ1	20 MHz	−69.63 dBc

(a) 2.4 GHz

1	5.725 GHz	−5.02 dBm
2Δ1	5 MHz	−49.18 dBc
3Δ1	10 MHz	−57.69 dBc
4Δ1	20 MHz	−65.63 dBc

(b) 5.725 GHz

Figure 4.31: Measured spectral performance of the PLL in the two bands

are depicted in Fig. 4.32. Since the VCO has a very linear tuning characteristic, the chirps can be directly observed at its control node. The chirp counter was clocked by an external signal from a FPGA test bed. There are four basic chirp generation schemes. The basic ones are a single burst, returning to zero, and a staircase burst staying high after finishing. Moreover, there are two continuous chirp modes, sawtooth and triangular-shaped.

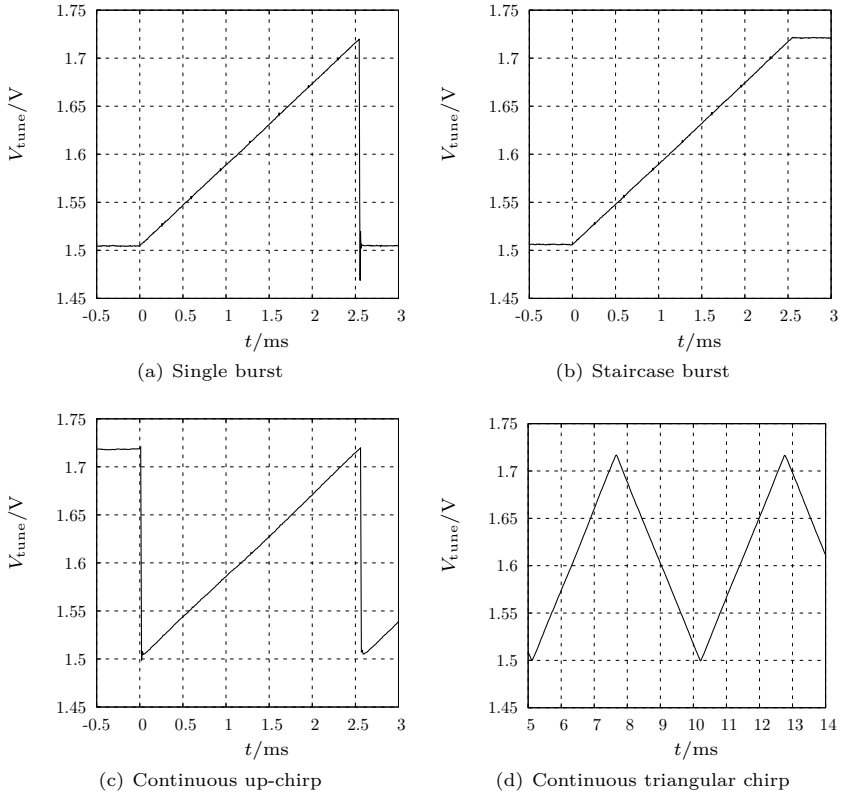

Figure 4.32: Measured tuning voltages for different chirp generation modes in the 5.8 GHz band

4.6.11 Comparison

Table 4.4 compares the presented PLL to recent publications of sub-10 GHz PLLs. The current work, although having worse phase noise performance, is among the ones with a largest relative bandwidth of more than 31 % in two bands with a very small frequency step size. Furthermore, it implements various chirp modulation waveforms. The circuit can be applied not only for radar applications but also multi-standard communications.

Ref.	Tech.	Freq. range (GHz)	Rel. band-width (%)	Freq. step (Hz)	In-band phase noise (dBc/Hz)	Out-of-band phase noise (dBc/Hz)	P_{DC} (mW)
[LC10]	130 nm CMOS	2.3-2.8	19.6	-	-83 at 10 kHz	-135 at 10 MHz	4.2
[TLL08]	180 nm CMOS	2.2-2.6	16.6	4.88 k	-81 at 100 kHz	-	22
[VLH+12]	90 nm CMOS	1.7-2.5	38	-	-	-115 at 1 MHz	1.13
[BSL07]	130 nm CMOS	2.17-2.95, 4.35-5.9	30.4	<1 k	<-90 at 100 kHz	<-108 at 1 MHz	51
[RDCR05]	500 nm SiGe	2.4, 4.9-5.8	16.8	781 k, 468 k	-98 at 10 kHz	<-120 at 1 MHz	99
This [JLWE14*]	180 nm SiGe	2.29-3.34, 4.57-6.69	31	0.6	<-75	-103 at 1 MHz	<122 (incl. VCO)

Table 4.4: Comparison with sub-10 GHz state-of-the-art integrated Fractional-N PLLs

4.7 Power Amplifier

4.7.1 Specification

For the design of a dual band power amplifier for FMCW radar systems, the frequencies of operation correspond to the specified ISM band frequencies at

$$f_1 = 2.4\,\text{GHz}, \tag{4.27}$$

$$f_2 = 5.8\,\text{GHz}. \tag{4.28}$$

The output power P_o is specified with maximum 20 dBm at 2.4 GHz and maximum 14 dBm at 5.8 GHz to comply with the regulations. Since FMCW only uses frequency modulation, it is possible to operate the amplifier in the compression region. A linear amplifier topology is specified rather than a switch-mode topology, since it allows a flexible design of the transistor load and matching networks.

A supply voltage of $V_{CC} = 3.3\,\text{V}$ is chosen as a common voltage supplied by voltage regulators available in the system. The power amplifier was developed as a separate chip and is not integrated with the rest of the components. The reason for this is the high expected power dissipation and radiated power.

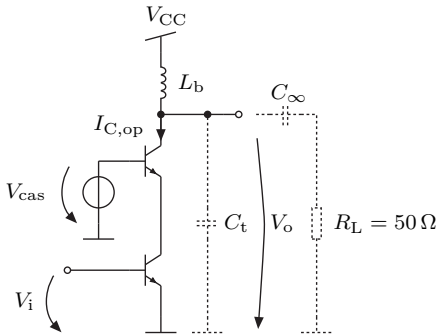

Figure 4.33: Basic schematic of a cascode power amplifier

For the circuit design, a cascode stage is the topology of choice. Especially for the rather large specified output powers, the transistor size will have to be large to handle the current and the input capacitance is expected to be in the picofarad range. The reduced Miller effect of the cascode stage will help to reduce current in the driver circuit and thus increase efficiency.

The basic cascode amplifier used for the presented design is shown in Fig. 4.33. The load is decoupled by a DC blocking capacitor C_∞ of sufficient size to not influence the matching network.

Using the above specifications, the operating point current of an inductively biased Class-A amplifier can then be calculated as

$$I_{C,op} = \frac{2P_o}{V_{CC} - V_{sat}} \tag{4.29}$$

Assuming $V_{sat} \approx 0.5\,\text{V}$ and using 18 dBm output power as a compromise between large bias current (and therefore a large transistor array with a very capacitive input) and power requirements, then $I_{C,op} \approx 45\,\text{mA}$.

4.7.2 Dual Band Matching Network

Impedance matching networks with multiple elements can efficiently transform impedances for multiple frequencies. The purpose of an output matching network in a power amplifier is to transform the real $50\,\Omega$ load to the optimum load resistance for the transistor and compensate for reactive portions of the transistor's output impedance. When the transistor is driving its optimum load resistance, it delivers maximum output power. The matching network has to perform this task for the two design frequencies f_1 and f_2. It should also be noted that the

optimum load resistance of the transistor depends on frequency.

As a first design step, the optimum load impedance $\underline{Z}_{\mathrm{opt}}(f)$ of an ideally biased cascode stage is determined using load-pull simulations. The simulation yields for both design frequencies

$$\underline{Z}_{\mathrm{opt}}(f_1) \approx (37 + \mathrm{j}16)\,\Omega, \tag{4.30}$$

$$\underline{Z}_{\mathrm{opt}}(f_2) \approx (12.5 + \mathrm{j}27.7)\,\Omega. \tag{4.31}$$

The simulation result represents a series equivalent circuit for the optimum load impedance. But, based on the circuit shown in Fig. 4.33, in small-signal domain the impedance needed at the output of the transistor is a parallel connection of L_{b} and C_{t}. Therefore, it is beneficial to transform $\underline{Z}_{\mathrm{opt}}(f)$ to a parallel equivalent circuit, which consists of a resistor and inductor.

$$\underline{Z}_{\mathrm{opt}}(f_1) \rightarrow 44\,\Omega||6.7\,\mathrm{nH} \tag{4.32}$$

$$\underline{Z}_{\mathrm{opt}}(f_2) \rightarrow 74\,\Omega||915\,\mathrm{pH} \tag{4.33}$$

It can be seen that the real part of $\underline{Z}_{\mathrm{opt}}(f)$ is close to the desired real load of $R_{\mathrm{L}} = 50\,\Omega$. That means, that a compromise for the implementation of a dual band power amplifier will be to select an operating point current of the transistor to get $\Re(1/\underline{Z}_{\mathrm{opt}}(f)) \approx 1/50\,\Omega$ at the desired frequencies. As a result, the matching network does not need to transform the real part, but just compensate for the reactive part at the two design frequencies. Consequently, instead of a single inductor L_{b}, a more complex network with impedance Z can be connected to the collector, which fulfills the following conditions:

$$\begin{aligned} Z(f_1) &\rightarrow \infty, \\ Z(f_2) &\rightarrow \infty, \\ Z(0) &= 0. \end{aligned} \tag{4.34}$$

At the design frequencies, the impedance has to reach infinity so that the transistor only sees the real load, which is close to the real part of the optimum load. At DC, the impedance needs to be zero to provide a bias current to the transistor.

The parasitic transistor capacitance C_{t} at the different frequencies can now be calculated using the resonance criterion, where the inductive part of $\underline{Z}_{\mathrm{opt}}(f)$ is considered to be L_{b}.

$$C_{\mathrm{t}} = \frac{1}{(2\pi f)^2 L_{\mathrm{b}}} \tag{4.35}$$

The calculation for the design frequencies results in

$$C_{\mathrm{t}}(f_1) \approx 656\,\mathrm{fF}, \tag{4.36}$$

$$C_{\mathrm{t}}(f_2) \approx 822\,\mathrm{fF}. \tag{4.37}$$

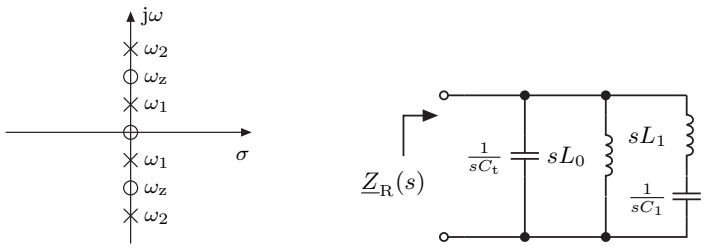

(a) Pole-zero diagram

(b) Matching network schematic

Figure 4.34: Pole-zero diagram and shunt circuit representation of the purely reactive one-port

To determine the structure and components of the matching network, one has to observe that the conditions of (4.34) can be fulfilled with a purely reactive one-port. The pole-zero plot and a schematic of a suitable implementation are shown in Fig. 4.34. The complex conjugate poles at ω_1 and ω_2 and the zero at $\omega = 0$ follow from the conditions (4.34). The complex conjugate zero at ω_z has to be added to ensure realizability as a circuit. The zero is chosen as the geometric mean of ω_1 and ω_2, which is

$$\omega_z = \sqrt{\omega_1 \omega_2}. \tag{4.38}$$

For the design frequencies f_1, f_2, the zero would be at $f_z = 3.73\,\text{GHz}$. Depending on the quality factor, the transfer function will get a dip with a certain bandwidth around the zero, which can help to attenuate harmonics when the amplifier is operating in the low band and in saturation.

In general, the impedance $\underline{Z}_R(s)$ then calculates as

$$\underline{Z}_R(s) = K \cdot \frac{s(s \pm j\omega_z)}{(s \pm j\omega_1)(s \pm j\omega_2)}, \tag{4.39}$$

where K denotes a scaling coefficient. Network synthesis procedures can deliver different circuit representations from this general impedance description. For the power amplifier, a shunt circuit representation is useful, since it already contains a parallel connection of L and C between the terminals. Thus, during the further course, the admittance description $\underline{Y}_R(s)$ will be used.

To determine the component values, a partial fraction expansion of $\underline{Y}_R(s)$ is done.

$$\underline{Y}_R(s) = 1/\underline{Z}_R(s) = \frac{s}{K} + \frac{\omega_1^2 \omega_2^2}{K {\omega_z}^2 s} + \frac{s\left(\omega_1^2 + \omega_2^2 - \frac{\omega_1^2 \omega_2^2}{{\omega_z}^2} - {\omega_z}^2\right)}{K(s^2 + {\omega_z}^2)} \tag{4.40}$$

The values of C_t and L_0 can be directly transcribed from the first two terms of (4.40).

$$C_\mathrm{t} = 1/K \tag{4.41}$$

$$L_0 = \frac{K{\omega_\mathrm{z}}^2}{\omega_1^2\omega_2^2} \tag{4.42}$$

The last term is a LC series resonant circuit. Rewriting it results in

$$\frac{s\left(\omega_1^2+\omega_2^2-\frac{\omega_1^2\omega_2^2}{{\omega_\mathrm{z}}^2}-{\omega_\mathrm{z}}^2\right)}{K(s^2+{\omega_\mathrm{z}}^2)} = \frac{1}{\frac{Ks}{\left(\omega_1^2+\omega_2^2-\frac{\omega_1^2\omega_2^2}{{\omega_\mathrm{z}}^2}-{\omega_\mathrm{z}}^2\right)}+\frac{K{\omega_\mathrm{z}}^2}{s\left(\omega_1^2+\omega_2^2-\frac{\omega_1^2\omega_2^2}{{\omega_\mathrm{z}}^2}-{\omega_\mathrm{z}}^2\right)}}. \tag{4.43}$$

Now the values for L_1 and C_1 can also be transcribed.

$$L_1 = \frac{K}{\left(\omega_1^2+\omega_2^2-\frac{\omega_1^2\omega_2^2}{{\omega_\mathrm{z}}^2}-{\omega_\mathrm{z}}^2\right)} \tag{4.44}$$

$$C_1 = \frac{\left(\omega_1^2+\omega_2^2-\frac{\omega_1^2\omega_2^2}{{\omega_\mathrm{z}}^2}-{\omega_\mathrm{z}}^2\right)}{K{\omega_\mathrm{z}}^2} \tag{4.45}$$

Using (4.41), K can now be calculated, since C_t is known from the load-pull simulation.

$$K = \frac{1}{C_\mathrm{t}} \tag{4.46}$$

As a result, C_t is already represented by a parasitic of the transistor and does not have to be implemented separately.

4.7.3 Circuit Description

The schematic of the driver and output stage is shown in Fig. 4.35. It consists of the above described cascode power stage with dual band matching network and a totem pole driver circuit [WWE12, JWE13b*].

Moreover, there is also a dual band inter-stage matching network, which is designed using the same procedure as for the output network. The inter-stage network helps to compensate for the large input capacitance of the power stage, which was determined by simulations to approximately 5 pF. This approach helps to save current in the totem pole driver. This network is also reused to bias the output stage using L_2 and a scaled replica of the cascode. The cascode voltage is generated by a V_BE multiplier.

The operating point current $I_\mathrm{C,op}$ was reduced to 38.5 mA while still fulfilling the output power requirements. This is because of the expansion characteristic

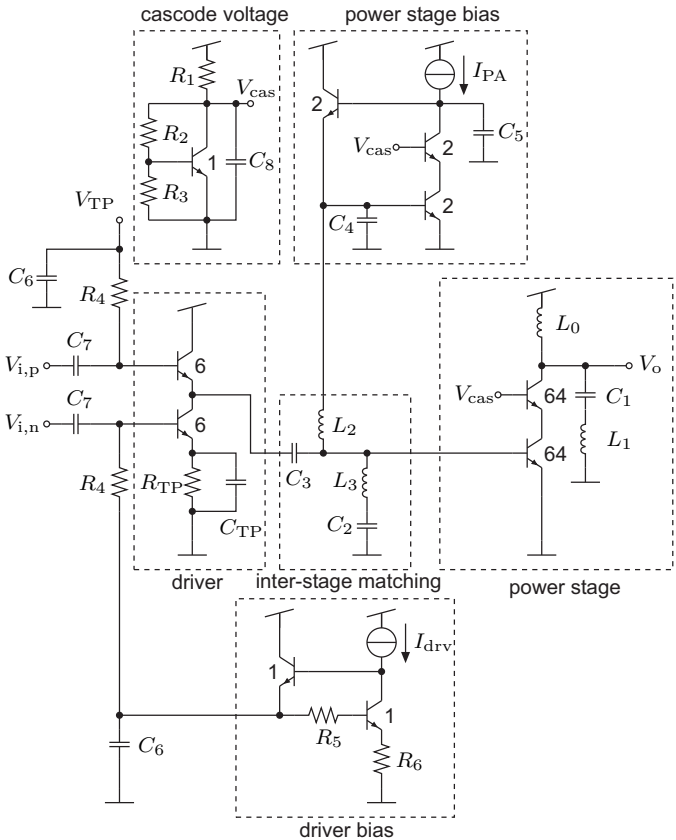

$C_1 = 411\,\text{fF}$	$C_2 = 4.67\,\text{pF}$	$C_3 = 13.3\,\text{pF}$	$C_4 = 96\,\text{pF}$
$C_5 = 40\,\text{pF}$	$C_6 = 12\,\text{pF}$	$C_7 = 15.8\,\text{pF}$	$C_8 = 74\,\text{pF}$
$R_1 = 508\,\Omega$	$R_2 = 3.6\,\text{k}\Omega$	$R_3 = 4.5\,\text{k}\Omega$	$R_4 = 2.3\,\text{k}\Omega$
$R_5 = 13.8\,\text{k}\Omega$	$R_6 = 194\,\Omega$	$R_{TP} = 32\,\Omega$	$C_{TP} = 432\,\text{fF}$
$L_0 = 1.84\,\text{nH}$	$L_1 = 3.19\,\text{nH}$	$L_2 = 318\,\text{pH}$	$L_3 = 384\,\text{pH}$
$I_{PA} = 1.2\,\text{mA}$	$I_{drv} = 1.3\,\text{mA}$	$V_{cas} = 1.6\,\text{V}$	$V_{TP} = 2.48\,\text{V}$

Figure 4.35: Schematic of the dual-band power amplifier and driver

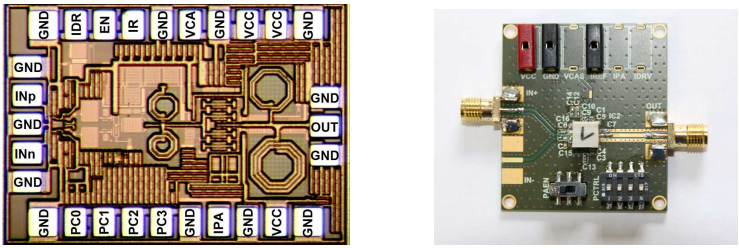

Figure 4.36: Power amplifier chip micrograph and test PCB

of the output stage, which leads to increasing current with increasing excitation.

It is worth noting that the totem pole driver needs a properly designed load network at the emitter of the lower transistor consisting of R_{TP} and C_{TP}. This network needs to be designed to match the load of the driver to ensure that both transistors of the totem pole configuration equally contribute current to the load. This is the case, when the emitter current of the upper transistor equals the collector current of the lower transistor in phase and magnitude for the specified operation frequencies. R_{TP} and C_{TP} were determined using small-signal simulations including the inter-stage matching network.

The complete power amplifier circuit furthermore includes a limiting amplifier stage at the input consisting of three cascaded differential amplifiers, which is not shown for the sake of clarity. Since the amplifier is used for FMCW operation, amplitude information is not needed and the signal can be clipped in the output stage to reach maximum output power and efficiency. Through the gain of the limiting amplifier, output power can be controlled by a 4 bit current digital-to-analog converter (DAC).

Stability was investigated using Rollett's stability factor K [Rol62]. During the design optimization, it was observed that $\mathrm{K} < 1$ for certain frequencies when tuning both, the output and inter-stage matching networks to the exact operating frequencies f_1, f_2. To ensure stability, it was necessary to slightly de-tune the inter-stage matching network, which resulted in a decrease of efficiency in the order of $< 5\,\%$ for both bands.

4.7.4 Measurement Results

The power amplifier was measured bonded onto a PCB to get the most realistic results regarding later use in the system. A chip micrograph and PCB photo is presented in Fig. 4.36. The chip area amounts to $1.2{\times}0.8\,\mathrm{mm}^2$. The input of the amplifier can be driven differentially or single-ended by terminating one of the inputs. The 4 bit power control can be set by the DIP switch and gives a maximum

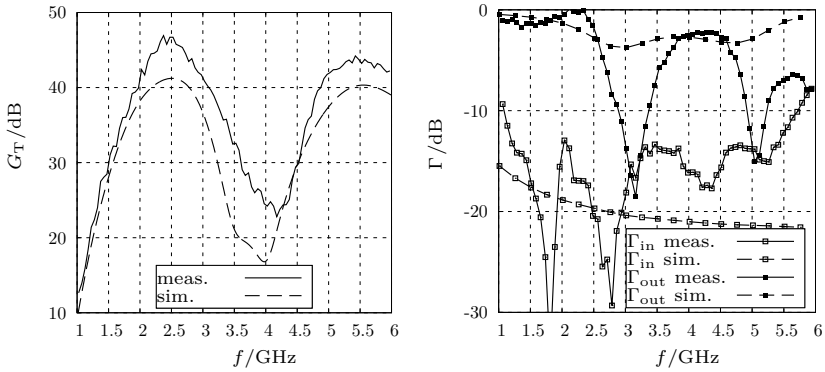

Figure 4.37: Measured and simulated transducer gain and input and output reflection coefficients

attenuation of about 8 dB. For the measurement, power was set to maximum and the input was driven single-ended. Output power was measured using a spectrum analyzer, which underwent a power calibration with a power meter before, thereby eliminating any cables and adapters in the signal path. Since the calibration plane is at the board connectors, all the measured characteristics still include the connectors, lines and blocking capacitors on the PCB, which can be considered as a major reason for mismatches to the simulated results.

Fig. 4.37 shows the small-signal measurement results. It has to be noted that the significance of those results for a power amplifier in general and for the limiting amplifier in this case is limited, since the default operating condition is large signal operation or even operation in saturation.

The transducer gain G_T is in the order of 45 dB for the 2.4 GHz band and 43 dB for the 5.8 GHz band. The high gain results from the limiting amplifier input stage of the circuit. The measured gain is 3 dB higher than what was simulated, but this can be a result of the difficult S-parameter calibration at low input powers to prevent saturation of the circuit. The run of the curve versus frequency matches well with simulations and clearly shows the zero in the region of 4 GHz and both poles at the design frequencies.

The input reflection coefficient Γ_{in} is below -8 dB for the whole frequency range. Input matching is achieved by a 50 Ω resistor. The output reflection coefficient Γ_{out} shows two spots of good matching which are in the area of 3 GHz and 5 GHz. The simulated curve also has those spots, but the magnitude of the return loss is much higher for the measurement. A possible explanation could

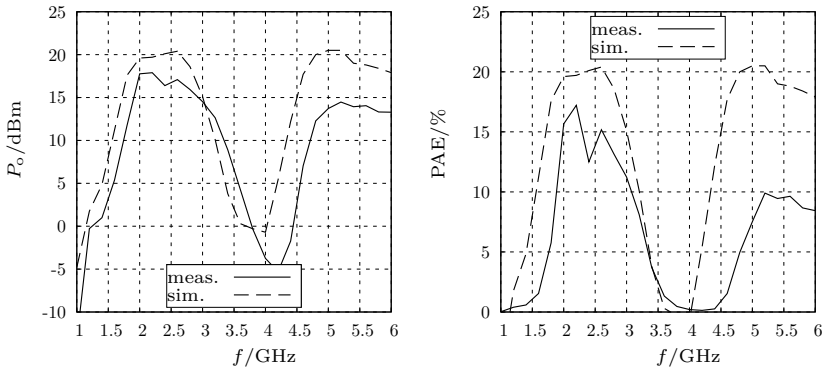

Figure 4.38: Measured and simulated output power and power added efficiency

be the influence of the bond interface, which adds additional series inductance to the output, thereby changing the return loss. However, since the following large signal measurements show that the circuit is capable of delivering the specified power to a 50 Ω load at the design frequencies and within a system consisting of long microstrip lines and cables, in the author's opinion output return loss is a negligible parameter for power amplifiers.

The measured and simulated results for output power and efficiency are presented in Fig. 4.38. Also here, the measured curves follow the simulated ones well, showing again the designed zero and poles. However, the measured output power in the 2.4 GHz band is about 3 dB below the simulated one, resulting in a drop of efficiency of about 7 %. In the 5.8 GHz band, output power drops about 4 dB with an efficiency penalty of about 10 %. The reasons for the loss of 3 to 4 dB are on the one hand the bond interface, blocking capacitor, board trace and SMA connector at the output, on the other hand the accuracy of the transistor models for operation in saturation region, especially for frequencies above 5 GHz. However, the circuit is still suitable for the use in the FMCW system, because the given output power specifications were met.

4.7.5 Comparison

Most of the up to date dual band power amplifier publications present designs using discrete components, usually with large filter networks containing lots of inductors. IC designers usually try to keep the inductor count low, since the number of inductors determines the size of an integrated circuit. Hence, Table 4.5 shows selected concurrent dual band power amplifiers, which were designed as an

Ref.	Tech.	Frequency (GHz)	Max. Power (dBm)	Max. PAE (%)	Area (mm^2)	Supply voltage (V)
[HN13]	180 nm SiGe	25.5 37	16 13	10.6 4.9	0.88	3
[GB09][1]	130 nm SiGe	2.4 3.5	18	43	1.56	1.5
[EL04]	180 nm CMOS	2.4 5.2	9.7 19.5	15.3	1.26	-
[LH05]	InGaP/ GaAs	2.4 5.2	25 18	40 50	1.26	3.5
[MO07]	180 nm CMOS	2.4 5.2	13 8.7	16.2 10.8	0.48	1.8
This[2] [JWLE14*]	180 nm SiGe	1.8-3.2 4.8-6	18.3 14.9	15.2 9.5	1.02	3.3

1 simulated
2 meas. on PCB

Table 4.5: Comparison with state-of-the-art integrated concurrent dual band power amplifiers

integrated circuit. The size of the presented design is roughly in the middle of all selected publications.

Regarding output power and PAE, the current design fits well to the other circuits published in similar frequency bands. However, one difference is the large possible bandwidth and spacing of the two operating frequencies allowed by the topology of the dual band matching network. The other published circuits will work inside the bandwidth of the specified communications standards, which is usually in the order of several 10 MHz. For the current work the 3 dB bandwidth of the output power related to the design frequencies was measured, achieving very large values of 1.4 GHz for the lower band and 1.2 GHz for the upper band.

As a conclusion, it can be stated that the power amplifier can be used in high resolution FMCW radars using wide band frequency chirps because of the large possible bandwidths. However, during design optimization it could also be seen that the output power specification especially for the 5.8 GHz band was already very demanding for the chosen topology in the given semiconductor technology. To increase efficiency, using a technology with higher transit frequency could be beneficial, because it would reduce the capacitive load of the output stage and thereby reduce driver current.

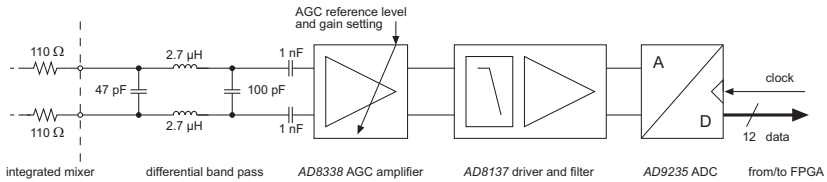

Figure 4.39: Base band signal processing chain of the dual band system

4.8 Post-Processing

4.8.1 Base Band

The base band processing chain of the dual band system follows the one described in the test system in section 3.5 with minor changes. It is depicted in Fig. 4.39. The complete signal path is fully differential, which helps rejecting common-mode interference. After the mixer, the down converted signal is band pass filtered using an off-chip passive LC filter. The lower cut-off frequency is in the order of 100 kHz to filter any DC offsets and low frequency noise. The upper cut-off frequency is at 3 MHz, working as part of the anti-aliasing filter. The filter is followed by the 0 dB to 80 dB VGA *AD8338*, whose gain can be set manually or an AGC feature can be enabled. The AGC amplifier is followed by the fully differential ADC driver *AD8137*, which is connected to form a dual feedback low pass filter. It forms the second part of the anti-alias filter. The differential 12-bit ADC *AD9235* is then used to sample the filtered and amplified base band signal for further digital processing in the FPGA.

4.8.2 Digital Signal Processing

The digital processing chain is completely implemented in the FPGA using fix point arithmetic. It consists of a sampler, Hamming window block, FFT core and peak detector as well as the CPU core presented in section 3.5. The sampler generates the 10 MHz sampling clock for the ADC and feeds the samples to the windowing block. There the signal is multiplied with a Hamming window stored in FPGA block RAM and is written to DDR memory. The FFT block uses a transform length of 65536 and is implemented using a Radix-2 architecture. Its latency for one transformation is approximately 6.5 ms, while running at an internal clock frequency of 100 MHz. The result of the transformation is also written to DDR memory, so both the time domain and frequency domain representations of the signal are available for later analysis. During the process of writing the FFT results to memory, the index with the highest amplitude, corresponding to the

base band beat frequency, is also stored. This value as well as the transformation result is then used in the CPU as input for the position estimation algorithm.

4.8.3 Position Estimation

For the sake of simplicity, the following section reduces the position calculation problem to a two-dimensional problem, assuming all stations are in a plane with constant height. Furthermore, a RToF positioning scheme is assumed with only one mobile station and a dual band measurement, i.e. one measurement value for each band.

In a RToF scheme, the system measures distances from the mobile station to every base station. The problem of position estimation is to find the most likely location of the mobile station from those distances. It can be considered a non-linear minimization problem. There are several approaches to find a solution:

- The problem can be solved directly numerically using the well-known Newton's method or the Gauss-Newton algorithm.
- Search algorithms like iterative grid search [Gie10] can be applied, which are easy to implement in embedded systems or directly in hardware because no or only few complex calculations are required and memory requirements are low.
- Tracking algorithms like the particle filter can be used. The particle filter algorithm attains the CRLB asymptotically for a large number of particles [Gus10]. However, with an increasing number of particles, the number of required calculations increases as well as memory consumption.

For measurement verification in this work, the iterative grid search algorithm was chosen because of its simplicity, both in implementation effort and in calculation complexity. The algorithm steps can be summarized as follows.

1. Generate a coarse grid with equidistant points spanning the area where the mobile station is located. In the simplest case, the area is a rectangle formed by at least three base stations.
2. Iterate through every grid point. Calculate the distance between this point and every base station. Calculate a cost function for each grid point, including the ideal distance vector and the measured distance vector from the LPS. Save the index of the grid point with the smallest cost function.
3. Generate a new grid with double the density of the old one centered around the saved grid index from step 2. Continue with step 2 until the grid granularity has the desired resolution.

The cost function is a metric, which states the accuracy of the tested point. It is given by [Gie10]

$$\mathcal{C}(\underline{m}) = \|\underline{d}_{\mathrm{B}} - \underline{d}_{\mathrm{m}}\|_2^2, \tag{4.47}$$

which is the squared Euclidean norm of the difference between the distance vector $\underline{d}_{\mathrm{B}}$ of the current grid point $\underline{m}$ to every base station and the distance vector $\underline{d}_{\mathrm{m}}$ measured by the system. The dimension of the vectors is N_{B}, which is the number of base stations.

To benefit from dual band measurements, it is necessary to incorporate distance measurements of both bands into the algorithm. A simple yet promising method is to check the statistical spread of a number of measured distances of both bands in the past. Then, the distances from the band with the lowest spread are taken for the position estimation. In the measurements of chapter 5 it is observed that sometimes measurements for certain stations in certain bands are unstable. The reasons can be bad antenna orientation, high signal attenuation due to obstacles or interference. The proposed algorithm should be capable to mitigate these problems. However, it has to be noted that the number of past measurements to consider has to be chosen in accordance with the expected dynamics of the target movements. A close-to-implementation description of the algorithm for the dual band system can be found in Listing 4.1. It also includes simple outlier filtering for estimated positions outside of the area spanned by the base stations.

```
% inputs:
%   N: number of measurements
%   N_B: number of base stations
%   RX, RY: vector of x and y coordinates of base stations
%   DIST_L,
%   DIST_H: distances for low and high band, matrices with size N x N_B
%   res: wanted resolution of the result in meters
%   num_x, num_y: starting number of grid points in x and y direction
%   stdnum: number of past measurements to consider
% outputs:
%   x_e, y_e: estimated x and y coordinate vectors of mobile station

% iterate through all measurements starting from stdnum
for num = stdnum:1:N

  % calculate spread of last measurements
  std_vect_24 = std(DIST_L(num-stdnum+1:num,:));
  std_vect_58 = std(DIST_H(num-stdnum+1:num,:));

  % select the ranges with lowest spread
  best = std_vect_24 > std_vect_58;

  % compile dual band distance vector
  % the entries in 'best' with true value use high band
  DB = DIST_L(num,:).*(~best) + DIST_H(num,:).*best;

  % initialize parameters of starting grid
  grid_x = (max(RX)-min(RX))/num_x;
  grid_y = (max(RY)-min(RY))/num_y;
  min_x = min(RX);
  max_x = max(RX);
  min_y = min(RY);
  max_y = max(RY);

  % iterate until the wanted resolution is reached
  while (grid_x > res) || (grid_y > res)

    x_grid_real = min_x:grid_x:max_x;
```

```
    y_grid_real = min_y:grid_y:max_y;
    num_x = length(x_grid_real);
    num_y = length(y_grid_real);

    % iterate through every grid point
    cost = Infinity;
    for x = 1:1:num_x
      for y = 1:1:num_y
        for k = 1:1:N_B
          % calculate distance between each grid position and base station
          dist(k) = sqrt((x_grid_real(x)-RX(k))^2 +
                         (y_grid_real(y)-RY(k))^2);
        end
        % calculate the new cost function
        cost_new = sum((dist-min(DB)).^2);
        % new cost function is smaller than previous one?
        if(cost_new < cost)
          x_idx = x;
          y_idx = y;
          cost = cost_new;
        end
      end
    end

    % initialize a new grid with double density
    min_x = x_grid_real(x_idx)-grid_x;
    max_x = x_grid_real(x_idx)+grid_x;
    min_y = y_grid_real(y_idx)-grid_y;
    max_y = y_grid_real(y_idx)+grid_y;

    grid_x = grid_x/2;
    grid_y = grid_y/2;

  end

  % resulting position at grid point index with smallest cost function
  x_e(num-stdnum+1) = x_grid_real(x_idx);
  y_e(num-stdnum+1) = y_grid_real(y_idx);

  % outlier detection
  % (set position to negative infinity and filter later)
  if ( x_e(num-stdnum+1) > max(RX) ) |
     ( x_e(num-stdnum+1) < min(RX) ) |
     ( y_e(num-stdnum+1) > max(RY) ) |
     ( y_e(num-stdnum+1) < min(RY) )
    x_e(num-stdnum+1) = -Infinity;
    y_e(num-stdnum+1) = -Infinity;
  end
end

x_e = x_e(x_e>-Infinity);
y_e = y_e(y_e>-Infinity);
```

Listing 4.1: Grid search algorithm for dual band 2D position estimation

5 Verification

5.1 Overview

The following sections present results from ranging and positioning with the designed LPS in indoor and outdoor scenarios using the single 2.4 GHz or 5.8 GHz bands and dual band signal processing. As a positioning scheme, RToF is employed.

There are several performance measures as outlined in section 2.3 which characterize a LPS. Many of them can only be defined scientifically for a very confined application or scenario. Therefore the characterization of the presented system is limited to precision and accuracy of distance and position measurements in different scenarios. Furthermore, it has to be noted that the results are only significant in the scenario in which they were obtained. Due to the complexity of the system and influence of the surroundings, even small changes in the scenario can drastically change the results. Moreover, it is almost impossible to characterize all outside influences. Especially for radio frequency systems, disturbances from omnipresent cellular networks or wireless access points cannot be eliminated, unless the measurements are done in shielded areas. Thus, a fair comparison with other systems is hard to achieve, also because the manufacturers of commercial systems usually do not disclose the complete test conditions for their results or use different and unknown definitions for system parameters such as accuracy and precision.

5.2 Reference Systems

For obtaining the true values for distances or positions of the stations, reference systems are necessary which must have accuracy and precision much better than what will be expected from the system under test. According to specifications, the system should be more accurate than one meter with a precision in the order of ten centimeters. For the reference system, it means that accuracy should be best in the millimeter range with sub-millimeter precision. In addition, the reference system should be transportable and useable in indoor and outdoor scenarios, which rules out mechanical positioning. Consequently, only optical position measurement systems qualify for this task.

A simple optical measurement device is a hand-held laser distance meter, which was already used to characterize the test system in section 3.7. It is the *Bosch*

(a) Laser distance meter

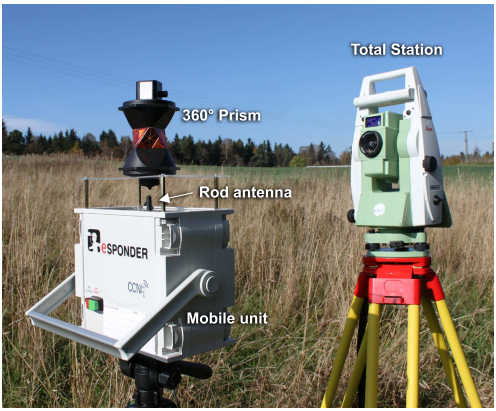

(b) Total station setup

Figure 5.1: Laser distance meter and total station setup

GLM 250 VF, with stated accuracy of ±1 mm, lowest indication unit of 0.1 mm and maximum range of 250 m. Because of its handiness, it is used to quickly verify distance measurements. Verification of position measurements is more cumbersome, because several distances have to be measured for each point.

To allow quick position measurements, a geodesic surveying tool is used, which is the *Leica TS15I* total station. It measures direction, elevation angle and distance to a target and calculates the position. The target can either be any surface or a special reflector. In this work a 360° prism is used. It allows to be targeted by the total station from any direction. Furthermore the total station can lock on and track the prism, saving the time of manually targeting each position. The maximum range without prism is stated with 1000 m, with prism it is 2000 m. The accuracy for distance measurements is stated as 1 mm ± 1.5 ppm.

Both reference systems are depicted in Fig. 5.1. The prism was mounted on top of the station used as mobile. The planar monopole antenna was changed to a rod antenna, which is mounted in the same axis as the prism.

5.3 Ranging and Synchronization Performance

In this section, the system is tested in basic scenarios to evaluate the ranging and therefore synchronization performance. The setup consists of only two stations. Firstly, two-way ranging is done in an anechoic chamber. Then the system is characterized under the exclusion of clock drift and synchronization errors by

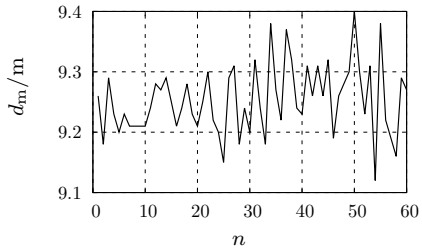

(a) Series

Parameter	Value
N	60
d_0/m (laser)	4.963
$\overline{d_m}$/m	9.254
d_e/m	4.291
σ_p/m	0.060

(b) Results

Figure 5.2: Two-way ranging measurement series and results in anechoic chamber

using a single stable reference frequency source for both stations and a synchronization cable. Lastly, two-way ranging is done in an outdoor scenario to evaluate accuracy, precision and maximum range in an environment with low multipath propagation.

Anechoic chamber Anechoic chambers are usually used for antenna characterization. For the ranging system, the measurement is done to rule out multipath effecs. Wireless two-way ranging distance measurements are performed with two base stations at 5.8 GHz. The reference distance between both stations was determined with the laser distance meter to 4.963 m. The series consisted of 60 single distance measurements, exhibiting a mean value of 9.254 m. This is due to a biased distance measurement as discussed in section 3.7.1. It was observed that the bias is different for every station and band, but always in the order of 4 m. The interesting result from this series is the precision of 6 cm, which is a good result. It can be used as the best possible benchmark value for the comparison with other scenarios.

Cable synchronization This measurement series was performed indoors on a desk with one base station and one tag. The reference frequency of 20 MHz for both units was supplied from a single frequency generator. Furthermore, the synchronization signal is sent via cable rather than using the FSK module. It allows benchmarking of the system precision with exclusion of clock drift or synchronization uncertainty, e.g. induced by the FSK module or synchronization algorithm. Also, signal processing like FFT and peak estimation was done on a computer with much higher numerical precision than in the hardware implementation.

A series with 50 one-way measurements was carried out. The signals were transmitted by the base station and received by the tag. The series yields a precision of 13 cm. Without the outlier at $n = 25$, precision reaches 10 cm. The

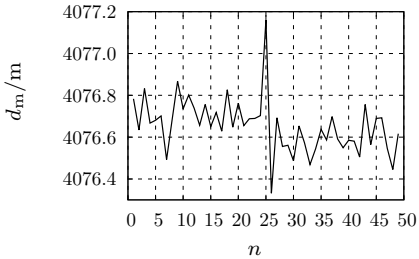

(a) Series

Parameter	Value
N	50
d_0/m (laser)	0.687
σ_p/m	0.130

(b) Results

Figure 5.3: One-way ranging measurement series and results indoors with synchronization by cable

mean is in the order of 4077 m. This high number results from the intentional time bias in the secondary station to shift the base band beat frequency to a useful band, as discussed in section 3.5.1. During two-way ranging, this bias would be canceled out.

Compared to the wireless two-way ranging in the anechoic chamber, the value for precision is approximately doubled. This leads to the conclusion that system precision is greatly influenced by the channel, which does not only include fading effects like multipath propagation but also interferers. Moreover, it can be concluded that the proposed wireless two-way synchronization algorithm works well, allowing precisions in the centimeter range. Lastly it can be stated that the numerical accuracy of the hardware FFT and parabolic spectrum estimation is good enough to not influence precision.

Outdoor ranging The outdoor test scenario was done to determine precision, accuracy and maximum range with wireless two-way ranging. Measurements were carried out on a large rectangular field, approximately 250 m in length. The reference distances were measured with the total station and the prism as target. The setup consisted of two stations, where the mobile with the prism was moved away from the fixed station and total station. The station height was always approximately $h = 1.4$ m. The total station was controlled remotely from the mobile station to avoid long walking paths. It is noteworthy, that the remote control uses a long range version of a *Bluetooth* radio at 2.4 GHz to communicate with the total station, which acts as narrow band interferer for the radar system. The distance of the transmitter to the mobile station was around 70 cm. Distance measurements were again biased differently in both bands, which was determined to 5.39 m at 2.4 GHz and 4.60 m at 5.8 GHz. For every distance, at least 100 single measurements were done in each band.

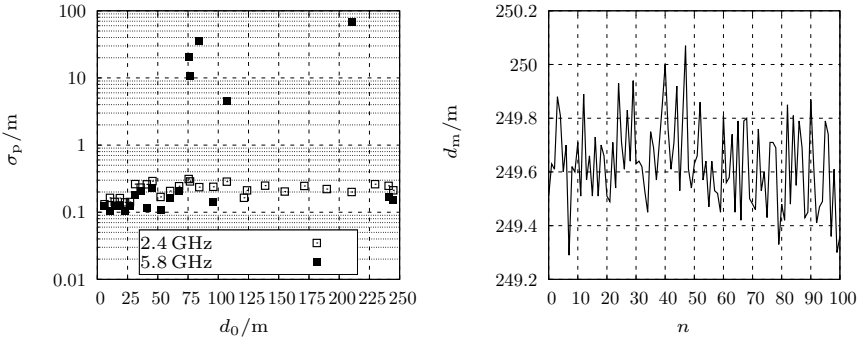

(a) Precision

(b) Biased 5.8 GHz series, $d_0 = 244.746$ m

Figure 5.4: Precision for outdoor distance measurements in both bands

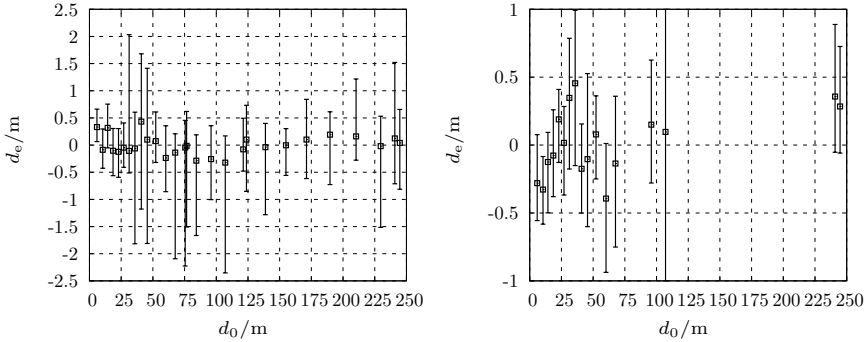

(a) 2.4 GHz

(b) 5.8 GHz

Figure 5.5: Measured distance error for outdoor scenario in both bands

Precision and accuracy are presented in Fig. 5.4 and Fig. 5.5, respectively. Precision in the 5.8 GHz band is slightly better for low ranges than in the 2.4 GHz band, probably due to the higher bandwidth and therefore less susceptibility to multipath signals. Also a jump in precision of around 8 cm can be observed at a distance of 25 m. For smaller distances, precision is around 16 cm at 2.4 GHz and 12 cm at 5.8 GHz.

Moreover, starting from 75 m, there is an increasing number of far outliers in the measurements at 5.8 GHz, whereas the precision in the 2.4 GHz band stays

similar for the whole distance range. In the range of 121 m to 230 m no useful results could be obtained in the high band. However, experiments at the last two distance measurement points with the inclination and orientation of the mobile station have shown that it is indeed possible to obtain stable results for the 5.8 GHz band, even at larger distances. This leaves as a conclusion, that antenna directivity might be an issue. Hence, for operating the system in larger areas, it could be beneficial to use less directive antennas.

The mean precision for the low band over all distances is $\overline{\sigma_{\mathrm{p,r,2.4}}} \approx 21.9\,\mathrm{cm}$, for the high band with distances lower than 75 m, $\overline{\sigma_{\mathrm{p,r,5.8}}} \approx 14.7\,\mathrm{cm}$. Precision is comparable to the indoor ranging with cable synchronization.

Accuracy of the measurement results is strongly dependent on bias, which was also observed for the test system from section 3.7. For the current scenario, the bias was determined from the mean of all measured distances subtracted by the values from the reference system. The graphs show the maximum, minimum and mean error versus the real distance with subtracted bias. The mean error in the 2.4 GHz band is bounded within $-0.32\,\mathrm{m}$ and $0.43\,\mathrm{m}$, in the 5.8 GHz band it amounts to $-0.39\,\mathrm{m}$ and $0.46\,\mathrm{m}$ (using the distances below 75 m).

The error bounds are similar in both bands, although the course of the error versus distance appears more stable in the low band. RMS accuracy for the series in low band amounts to $\sigma_{\mathrm{a,r,2.4}} \approx 8.2\,\mathrm{cm}$, in the high band again for distances lower than 75 m, $\sigma_{\mathrm{a,r,5.8}} \approx 8.6\,\mathrm{cm}$.

A noticeable result from this measurement series is the verification of a quite large range of around 245 m which goes well with the specified $d_{0,\max} = 300\,\mathrm{m}$. Unfortunately, the size of the test area was limited and higher distances could not be verified. Since for this scenario accuracy is better than precision, system performance can be enhanced by using filtering methods, in the simplest case averaging. Already here, it can also be observed that adding redundancy by dual band measurements can prove advantageous by switching to the other band when precision is above a certain threshold or no signal was received.

5.4 Outdoor Environment

For verification of the complete dual band positioning system, an outdoor and indoor scenario were set up. The outdoor measurements were done in a large sports arena with a size of approximately 80 m by 60 m. The influence of multipath propagation in this scenario is expected to be low. Four base stations were distributed in the corners of the area. RToF measurements were done with a base station used as a mobile. The total station together with the prism target was used as a reference system. A drawing and photograph of the area is presented in Fig. 5.6.

The northing of the reference coordinate system is defined by base stations 1

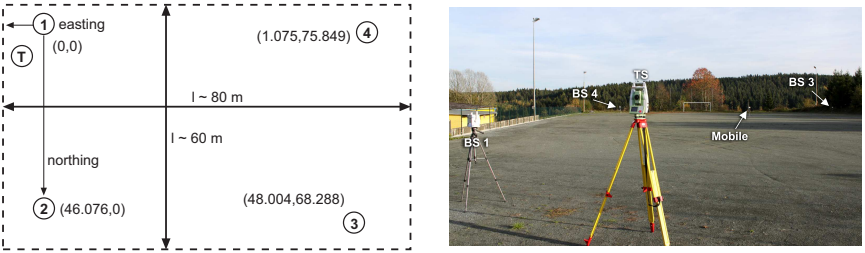

(a) Drawing (b) Photograph

Figure 5.6: Outdoor measurement setup in sports arena

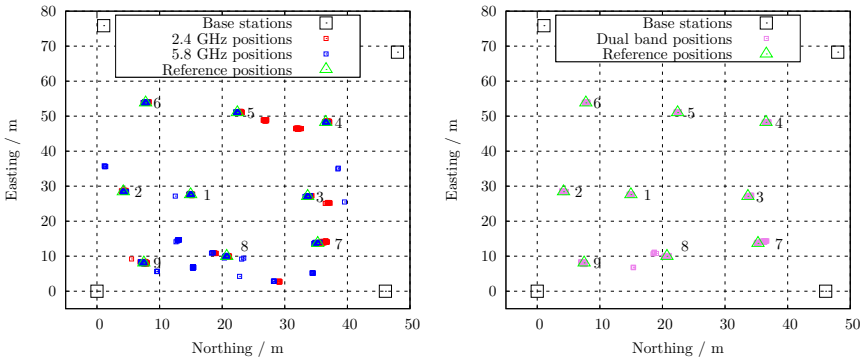

(a) Single band positions (b) Dual band positions

Figure 5.7: Single band and dual band test positions in outdoor scenario

and 2. Easting is exactly perpendicular to this line. Note that easting has been inverted for the evaluation to get only positive coordinates. To prevent disturbing the LPS, the total station was operated directly without remote control. A total of 9 positions were measured with the reference system and the LPS in both bands. For each position, the dual band grid search algorithm from section 4.8.3 was performed. At least 100 measurements per location were done in each band.

The measured positions along with the anchor coordinates are depicted in Fig. 5.7. The single band results generally follow the reference positions, however also a significant number of outliers can be observed. These are caused by instability in one or more of the RToF distance measurements, e.g. due to bad antenna

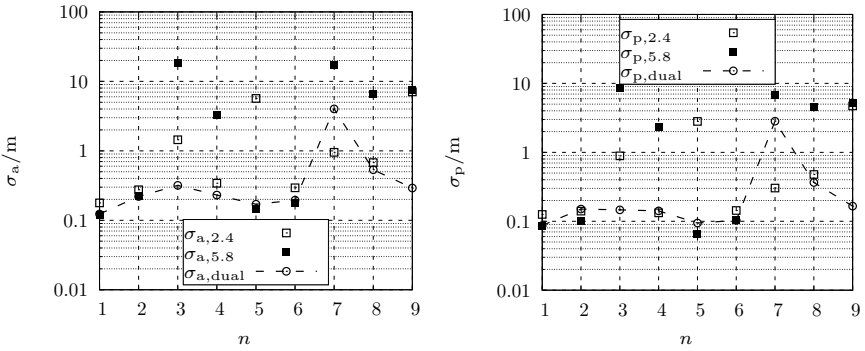

(a) Accuracy (b) Precision

Figure 5.8: Accuracy and precision of positions in outdoor scenario

orientation of the mobile to a particular base station. Sometimes the measured distance is also stable for some short time and then changes to another slightly different stable value. This indicates that there are multiple spectral components in the base band signal which are detected randomly. It is shown in the diagram as clustering of measured positions, e.g. near test points 3 or 5.

When performing the dual band grid search algorithm, the outliers almost reduce to none. Also the clustering effect is greatly mitigated. The improvement of the dual band processing is also witnessed by accuracy and precision figures as presented in Fig. 5.8. The outliers still visible in the dual band results belong to position 7, degrading the performance for this point. The dual band grid search used the last 6 measurements for estimation of the spread. Increasing this number enhances the results even further, getting rid of remaining outliers. However, the ability of the system to track dynamic movements decreases at the same time.

Accuracy with dual band processing is better than the best single band result in 78 % of the cases, while in 66 % of the cases, dual band precision is better.

Mean accuracy for the series amounts to $\overline{\sigma_{\mathrm{a,o},2.4}} \approx 1.88\,\mathrm{m}$ at 2.4 GHz, $\overline{\sigma_{\mathrm{a,o},5.8}} \approx 5.93\,\mathrm{m}$ at 5.8 GHz, while mean accuracy in the dual band case is as good as $\overline{\sigma_{\mathrm{a,o,dual}}} \approx 0.68\,\mathrm{m}$. The accuracy improvement with dual band processing in this scenario is by a factor of 2.8 at 2.4 GHz and a factor of 8.7 at 5.8 GHz.

Mean precision is $\overline{\sigma_{\mathrm{p,o},2.4}} \approx 1.08\,\mathrm{m}$ at 2.4 GHz, $\overline{\sigma_{\mathrm{p,o},5.8}} \approx 3.09\,\mathrm{m}$ at 5.8 GHz and only $\overline{\sigma_{\mathrm{p,o,dual}}} \approx 0.45\,\mathrm{m}$ in the dual band case. The poor precision in the single band case is due to a large number of outliers. The precision improvement with dual band processing in this scenario is by a factor of 2.4 at 2.4 GHz and a factor of 6.7 at 5.8 GHz.

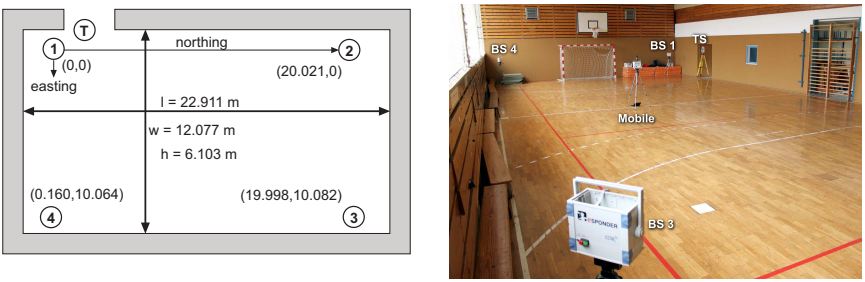

(a) Drawing

(b) Photograph

Figure 5.9: Indoor measurement setup in gymnasium

5.5 Indoor Environment

The indoor measurements were done in a small gymnasium with the dimensions of 22.9 m by 12.1 m and height of 6.1 m. Multipath propagation is expected to be moderate. The base station setup and total station setup is equal to the outdoor scenario. Fig. 5.9 shows a drawing and photograph of the setup. A total of 15 positions were measured with at least 100 measurements per position and band.

The measured positions for single and dual band cases are presented in Fig. 5.10. Compared to the outdoor scenario, a substantially higher amount of outliers and clustering is observed. Mostly the positions determined with the high band are more precise, which is explained by the higher chirp bandwidth and therefore better range resolution in the presence of multipath propagation. With dual band processing, the outliers are again diminished greatly, although their number is larger compared to the outdoor scenario. Also a small amount of clustering is still visible, but the determined positions follow the references very well. In this scenario, again the last 6 measurements are taken for estimation of the spread in the dual band grid search.

Accuracy and precision for all measured positions in the indoor scenario are shown in Fig. 5.11. Precision and accuracy for the high band is superior to the low band in most of the cases as already observed from the position diagram. However, mean accuracy and mean precision is degraded compared to the low band, because outliers in the high band are larger. Accuracy with dual band processing is equal or better than the best single band result in 53 % of the cases, dual band precision is better in 33 % of the cases. Compared to the outdoor scenario, the improvements are less imposing. On the other hand, the larger number of outliers justifies the result. Further improvements can again be achieved by using more measurements in the dual band grid search for spread estimation.

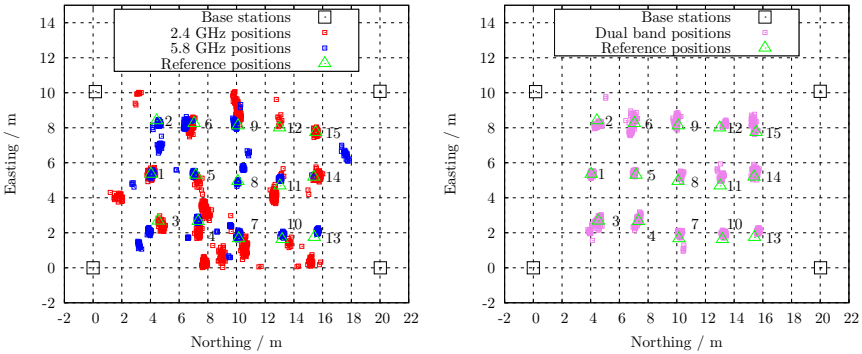

(a) Single band positions

(b) Dual band positions

Figure 5.10: Single band and dual band test positions in indoor scenario

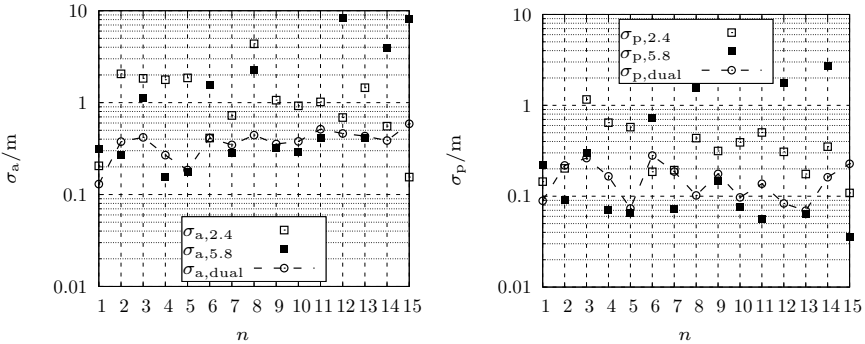

(a) Accuracy

(b) Precision

Figure 5.11: Accuracy and precision of positions in indoor scenario

Mean accuracy for the complete series amounts to $\overline{\sigma_{a,i,2.4}} \approx 1.27\,\text{m}$ at 2.4 GHz and $\overline{\sigma_{a,i,5.8}} \approx 1.86\,\text{m}$ at 5.8 GHz. Dual band processing enhances mean accuracy to $\overline{\sigma_{a,i,dual}} \approx 0.38\,\text{m}$. This corresponds to an accuracy improvement by a factor of 3.3 at 2.4 GHz and a factor of 4.9 at 5.8 GHz.

Mean precision yields $\overline{\sigma_{p,i,2.4}} \approx 0.38\,\text{m}$ at 2.4 GHz and $\overline{\sigma_{p,i,5.8}} \approx 0.53\,\text{m}$ at 5.8 GHz. The dual band precision results in a very good $\overline{\sigma_{p,i,dual}} \approx 0.16\,\text{m}$. The precision improves by a factor of 2.4 at 2.4 GHz and a factor of 3.3 at 5.8 GHz.

Scenario	Description	Symbol	Value
Anechoic chamber	Best ranging precision	$\sigma_{\mathrm{p,min}}$	6 cm
Outdoor ranging	Range	$d_{0,\mathrm{max}}$	$\geq$245 m
	Precision, low band	$\overline{\sigma_{\mathrm{p,r,2.4}}}$	21.9 cm
	Precision, high band	$\overline{\sigma_{\mathrm{p,r,5.8}}}$	14.7 cm, $d_0 < 75$ m
	Accuracy, low band	$\sigma_{\mathrm{a,r,2.4}}$	8.2 cm
	Accuracy, high band	$\sigma_{\mathrm{a,r,5.8}}$	8.6 cm, $d_0 < 75$ m
Outdoor positioning	Precision, low band	$\overline{\sigma_{\mathrm{p,o,2.4}}}$	1.08 m
	Precision, high band	$\overline{\sigma_{\mathrm{p,o,5.8}}}$	3.09 m
	Precision, dual band	$\overline{\sigma_{\mathrm{p,o,dual}}}$	0.45 m
	Accuracy, low band	$\overline{\sigma_{\mathrm{a,o,2.4}}}$	1.88 m
	Accuracy, high band	$\overline{\sigma_{\mathrm{a,o,5.8}}}$	5.93 m
	Accuracy, dual band	$\overline{\sigma_{\mathrm{a,o,dual}}}$	0.68 m
Indoor positioning	Precision, low band	$\overline{\sigma_{\mathrm{p,i,2.4}}}$	0.38 m
	Precision, high band	$\overline{\sigma_{\mathrm{p,i,5.8}}}$	0.53 m
	Precision, dual band	$\overline{\sigma_{\mathrm{p,i,dual}}}$	0.16 m
	Accuracy, low band	$\overline{\sigma_{\mathrm{a,i,2.4}}}$	1.27 m
	Accuracy, high band	$\overline{\sigma_{\mathrm{a,i,5.8}}}$	1.86 m
	Accuracy, dual band	$\overline{\sigma_{\mathrm{a,i,dual}}}$	0.38 m

Table 5.1: Summary of verified key system parameters

5.6 Summary

Table 5.1 summarizes the measured system parameters for different scenarios. Precision and accuracy of the system have been verified. Especially the enhancement of the system performance with dual band processing is remarkable, reaching improvements of at least factor 2.4 in precision and factor 2.8 in accuracy. The mean positioning accuracy is between 0.38 m and 0.68 m, which exceeds the project specification of less than one meter. The mean positioning precision can be as low as 0.16 m in the small-scale indoor scenario and 0.45 m in the large-scale outdoor scenario. The range between two base stations was verified up to 245 m, which is close to the specification of 300 m set by the application.

In conclusion, it can be stated that the set goal of improving system performance with information from multiple frequency bands has been achieved. Due to the verified performance fitting to the project specifications and the added dual band redundancy the developed LPS is ready to be tested within the E-SPONDER system.

6 Conclusion and Outlook

This work described the modeling, design and verification of a novel dual band local positioning system. It improves the state of the art with the following aspects:

- Models were derived for system imperfections occurring in FMCW radar systems. Relevant literature investigates the influence of thermal noise, phase noise and chirp linearity on the radar performance. This work models effects which are equally important, such as compression and intermodulation, the influence of automatic gain control, blockers and spurious emissions. The models are used to derive a specification set for the circuit design of a LPS based on the FMCW radar approach.
- A complete LPS prototype was designed consisting of base stations and tags encapsulating most of the RF and analogue signal processing in integrated circuits. This design approach allowed to reduce size and power consumption compared to a hybrid system, which was also designed during the course of this work. Key components were implemented using concepts, which support operation in multiple frequency bands, namely, the receiver consisting of LNA and mixer, the frequency synthesizer with broadband chirp generation capabilities and a dual band power amplifier.
- Since the system uses dual band or broad band components, it is possible to obtain ranging data using multiple bands. Using dual band processing, positioning accuracy in an indoor scenario was measured to 0.38 m which is an improvement by at least a factor of 3.3 compared to a single band system. In a large outdoor scenario accuracy attained 0.68 m, which is an improvement by a factor of at least 2.8. Outliers are filtered effectively and the added redundancy makes the system more robust.
- An enhanced version of the grid search algorithm for position estimation has been developed, which makes use of data from multiple frequency bands or, in general, any data source. The algorithm can be easily implemented in embedded systems.

Due to the multi disciplinary nature of local positioning systems, there are also several directions for further research. Concerning channel modeling and signal propagation theory, the following further work could be done.

- Modeling effort on different multipath signals could be performed, e.g. by using channel models for different environments [MCC+06], to design strategies for mitigation of multipaths or their detection.

- Research on antennas can be carried out to determine suitable characteristics for ranging and localization.

A major part of every localization system is the post-processing of data, which includes algorithms for synchronization, ranging or position estimation as well as the art of performing numeric calculations within the confined borders of an embedded system.

- The applicability of spectral estimation algorithms other than peak detection could be investigated to reach a better range calculation in the presence of multipath propagation. Such algorithms may use neural networks [GWW09].
- More work on tracking and position estimation algorithms could help to use all benefits of the system to the full possible extent, e.g. by exploiting the multi channel option.
- The current system has to be analyzed for optimization potential regarding its update rate by the optimization of post-processing algorithms for speed or parallelism. This would also allow the application in real-time environments, e.g. highly accurate car tracking.

Finally, an important class of further research includes the hardware and circuit design, which directly affects the processing of analogue data and which is the foundation of every electronic system.

- In the circuit design domain, there is also potential for increasing the system update rate, e.g. by investigating and optimizing the settling behaviour of circuits like PLL or power amplifier.
- As shown in this thesis, ranging variation is largely influenced by the hardware implementation. Concepts can be investigated to improve noise like thermal or phase noise with the goal of reaching a better precision. Optimization potential also lies within the PLL-based chirp generator and deterministic clock domain synchronization strategies to provide a more deterministic chirp generation.
- Circuits can be optimized for power consumption to target also applications where limited weight and size is necessary and therefore battery capacity is limited.
- Steps can be performed which are necessary for a higher level of integration, e.g. by also integrating the additional FSK transceiver for protocol handling.
- Additional hardware could be added to the system to aid position estimation like inertial measurement units. In this regard, an approach towards heterogeneous localization systems can be investigated.

References

[AHR07] A. Amer, E. Hegazi, and H. Ragaie, "A 90-nm Wideband Merged CMOS LNA and Mixer Exploiting Noise Cancellation," *IEEE Journal of Solid-State Circuits*, vol. 42, no. 2, pp. 323–328, Feb 2007.

[Ana13] Analog Devices, "Direct Modulation/Waveform Generating, 6.1 GHz Fractional-N Frequency Synthesizer ADF4158," Oct. 2013. [Online]. Available: http://www.analog.com/static/imported-files/data_sheets/ADF4158.pdf

[ARUS+03] P. Ali-Rantala, L. Ukkonen, L. Sydanheimo, M. Keskilammi, and M. Kivikoski, "Different kinds of walls and their effect on the attenuation of radiowaves indoors," in *IEEE Antennas and Propagation Society International Symposium*, vol. 3, june 2003, pp. 1020 – 1023 vol.3.

[Atm13] Atmel, "8-bit AVR Instruction Set," Oct. 2013. [Online]. Available: http://www.atmel.com/images/doc0856.pdf

[BFH+96] D. Borkowski, H. Fung, H. Habal, K. Chao, S. Kai, and D. Robert, "Cellular network-based location system," United States Patent US5 519 760A, 1996.

[BKLN08] S. Blaakmeer, E. Klumperink, D. Leenaerts, and B. Nauta, "The Blixer, a Wideband Balun-LNA-I/Q-Mixer Topology," *IEEE Journal of Solid-State Circuits*, vol. 43, no. 12, pp. 2706–2715, Dec 2008.

[BSL07] A. Bonfanti, C. Samori, and A. Lacaita, "A multistandard Σ-Δ fractional-N frequency synthesizer for 802.11a/b/g WLAN," in *33rd European Solid State Circuits Conference (ESSCIRC)*, Sept 2007, pp. 480–483.

[CB92] V. I. Cojocaru and T. J. Brazil, "A Large-Signal Equivalent Circuit Model for Hyperabrupt P-N Junction Varactor Diodes," in *22nd European Microwave Conference*, vol. 2, sept. 1992, pp. 1115–1121.

[CHWL12] Y.-C. Chen, C. Hsuan Wang, and Y.-S. Lin, "Low-power 24 GHz CMOS receiver front-end using isolation enhancement technique for automatic radar systems," *Microwave and Optical Technology Letters*, vol. 54, no. 6, pp. 1471–1476, 2012.

[Cra08] J. Crawford, *Advanced phase-lock techniques*, ser. Artech House Microwave Library. Artech House, 2008.

[DS03] T. Deasy and W. Scanlon, "Stepwise refinement algorithms for prediction of user location using receive signal strength indication in infrastructure WLANs," in *High Frequency Postgraduate Student Colloquium*, Sept 2003, pp. 116–119.

[DSS06] J. Dominguez, S. Sancho, and A. Suarez, "VCO Linearization Using Harmonic Balance," in *IEEE MTT-S International Microwave Symposium Digest*, June 2006, pp. 864–867.

[EL04] Y. Eo and K. Lee, "A 2.4GHz/5.2GHz CMOS power amplifier for dual-band applications," in *IEEE MTT-S International Microwave Symposium Digest*, vol. 3, 2004, pp. 1539–1542 Vol.3.

[Ele13] Electronic Communications Committee, "ERC Recommendation 70-03," Oct. 2013. [Online]. Available: http://www.erodocdb.dk/Docs/doc98/official/pdf/Rec7003e.PDF

[Ell07] F. Ellinger, *Radio Frequency Integrated Circuits and Technologies*. Berlin: Springer, 2007.

[ESV12] R. Ebelt, D. Shmakov, and M. Vossiek, "The effect of phase noise on ranging uncertainty in FMCW secondary radar-based local positioning systems," in *9th European Radar Conference (EuRAD)*, Oct 2012, pp. 258–261.

[FCL+08] K. Fu, Z. Cheng, J. Li, Y. Zhou, and X. Zhou, "Design of wideband LC VCO with small Kvco fluctuation for RFID synthesizer application," in *11th IEEE International Conference on Communication Technology, ICCT.*, nov. 2008, pp. 286 –289.

[Fed14] Federal Communications Commission, "Part 18," Jan. 2014. [Online]. Available: http://www.gpo.gov/fdsys/pkg/CFR-2010-title47-vol1/pdf/CFR-2010-title47-vol1-part18.pdf

[Fri46] H. Friis, "A Note on a Simple Transmission Formula," *Proceedings of the IRE*, vol. 34, no. 5, pp. 254–256, 1946.

[GB09] M. Ghajar and S. Boumaiza, "Concurrent dual band 2.4/3.5GHz fully integrated power amplifier in 0.13um CMOS technology," in *European Microwave Integrated Circuits Conference, EuMIC*, 2009, pp. 375–378.

[GDGAFVM10] V. Gonzalez-Diaz, M. Garcia-Andrade, G. Flores-Verdad, and F. Maloberti, "Efficient Dithering in MASH Sigma-Delta Modulators for Fractional Frequency Synthesizers," *IEEE Transactions on Circuits and Systems I: Regular Papers*, vol. 57, no. 9, pp. 2394–2403, Sept 2010.

[Gie10] R. Gierlich, *A Reconfigurable MIMO System for High-Precision FMCW Radiolocation.* Dr. Hut, 2010.

[Gil98] B. Gilbert, "The multi-tanh principle: a tutorial overview," *IEEE Journal of Solid-State Circuits*, vol. 33, no. 1, pp. 2–17, Jan 1998.

[Gus10] F. Gustafsson, "Particle filter theory and practice with positioning applications," *IEEE Aerospace and Electronic Systems Magazine*, vol. 25, no. 7, pp. 53–82, July 2010.

[GWW09] A. Goetz, B. Waldmann, and R. Weigel, "Short multipath mitigation technique using feedforward neural networks," in *German Microwave Conference*, March 2009, pp. 1–4.

[Har78] F. Harris, "On the use of windows for harmonic analysis with the discrete Fourier transform," *Proceedings of the IEEE*, vol. 66, no. 1, pp. 51–83, 1978.

[HH79] E. Hewitt and R. E. Hewitt, "The Gibbs-Wilbraham phenomenon: An episode in fourier analysis," *Archive for History of Exact Sciences*, vol. 21, no. 2, pp. 129–160, 1979.

[HKJ09] M.-S. Hwang, J. Kim, and D.-K. Jeong, "Reduction of pump current mismatch in charge-pump PLL," *Electronics Letters*, vol. 45, no. 3, pp. 135–136, 2009.

[HN13] C. Huynh and C. Nguyen, "New technique for synthesizing concurrent dual-band impedance-matching filtering networks and 0.18um sige bicmos 25.5/37-ghz concurrent dual-band power amplifier," *IEEE Transactions on Microwave Theory and Techniques*, vol. 61, no. 11, pp. 3927–3939, Nov 2013.

[Hui11] J. Huijsing, *Operational Amplifiers*, 2nd ed. Dodrecht: Springer, 2011.

[IBM13] IBM, "BiCMOS 7WL," Sep. 2013. [Online]. Available: www.ibm.com/chips/techlib/techlib.nsf/products/BiCMOS_7WL

[IEE08] IEEE, "IEEE Standard Definitions of Physical Quantities for Fundamental Frequency and Time Metrology - Random Instabilities," *IEEE STD 1139-2008*, Feb 2008.

[Ihl13] D. Ihle, "Entwurf eines Hybridaufbaus für eine 60 GHz Fractional-N Phasenregelschleife," Studienarbeit, Technische Universität Dresden, Germany, 2013.

[JB13] M. Jalalifar and G.-S. Byun, "Near-threshold charge pump circuit using dual feedback loop," *Electronics Letters*, vol. 49, no. 23, pp. 1436–1438, Nov 2013.

[Kha11] S. Khan, *Digital Design of Signal Processing Systems: A Practical Approach*. Wiley, 2011.

[KOH+97] Y. Kado, T. Ohno, M. Harada, K. Deguchi, and T. Tsuchiya, "An ultralow power CMOS/SIMOX programmable counter LSI," *IEEE Journal of Solid-State Circuits*, vol. 32, no. 10, pp. 1582–1587, Oct 1997.

[KQ99] S. Kingsley and S. Quegan, *Understanding Radar Systems*. Mendham: SciTech Publishing, Inc., 1999.

[LC10] W. Lee and S. Cho, "A 2.4-GHz reference doubled fractional-N PLL with dual phase detector in 0.13-um CMOS," in *Proceedings of 2010 IEEE International Symposium on Circuits and Systems (ISCAS)*, May 2010, pp. 1328–1331.

[Lei15] Leica, "Viva GS25," Jan. 2015. [Online]. Available: http://www.leica-geosystems.com/en/Leica-Viva-GS10-GS25_105545.htm

[LGM+09] Y. Liu, D. Goshi, K. Mai, L. Bui, and Y. Shih, "Linearity study of DDS-based W-band FMCW sensor," in *IEEE MTT-S International Microwave Symposium Digest. MTT '09.*, June 2009, pp. 1697–1700.

[LH05] C.-C. Lin and Y.-C. Hsu, "Single-chip dual-band WLAN power amplifier using InGaP/GaAs HBT," in *European Microwave Conference*, vol. 3, 2005, pp. 4 pp.–.

[LJC+00] J. S. Lee, W. K. Jin, D. M. Choi, B.-W. Lee, and S. Kim, "A wide range PLL for 64X speed CD-ROM and 10X speed DVD-ROM," in *International Conference on Consumer Electronics, ICCE, Digest of Technical Papers.*, 2000, pp. 98–99.

[LSJH12] P. Liu, P. Sun, J. Jung, and D. Heo, "PLL charge pump with adaptive body-bias compensation for minimum current variation," *Electronics Letters*, vol. 48, no. 1, pp. 16–18, 2012.

[LT09] V. Lakafosis and M. Tentzeris, "From single-to multihop: The status of wireless localization," *IEEE Microwave Magazine*, vol. 10, no. 7, pp. 34–41, Dec 2009.

[MAG14] MAGELLAN, "European Integration Project," Oct 2014. [Online]. Available: http://www.magellanproject.eu/

[Man12] C. Man, "Quantization Noise: An Expanded Derivation of the Equation SNR=6.02N+1.76dB," *Analog Devices*, no. MT-229, 2012.

[Max04] Maxim Integrated, "Application Note 3359," Dec 2004.

[MCC+06] A. Molisch, D. Cassioli, C.-C. Chong, S. Emami, A. Fort, B. Kannan, J. Karedal, J. Kunisch, H. Schantz, K. Siwiak, and M. Win, "A comprehensive standardized model for ultrawideband propagation channels," *IEEE Transactions on Antennas and Propagation*, vol. 54, no. 11, pp. 3151–3166, Nov 2006.

[Min12] Z. Mingzhu, "A low phase noise wideband VCO in 65nm RF CMOS for low power applications," in *International Conference on Microwave and Millimeter Wave Technology (ICMMT)*, vol. 1, may 2012, pp. 1–4.

[MNR08] M. Mehrabian, A. Nabavi, and N. Rashidi, "A 4-7GHz ultra wideband VCO with tunable active inductor," in *IEEE International Conference on Ultra-Wideband, ICUWB.*, vol. 2, sept. 2008, pp. 21–24.

[MO07] H. Magnusson and H. Olsson, "A Compact Dual-Band Power Amplifier Driver for 2.4GHz and 5.2GHz WLAN Transmitters," in *IEEE Radio Frequency Integrated Circuits (RFIC) Symposium*, 2007, pp. 83–86.

[MPY+05] R. Mukhopadhyay, Y. Park, S. Yoon, C.-H. Lee, S. Nuttinck, J. Cressler, and J. Laskar, "Active-inductor-based low-power broadband harmonic VCO in SiGe technology for wideband and multi-standard applications," in *IEEE MTT-S International Microwave Symposium Digest*, june 2005, pp. 1349–1352.

[MSM+12] H. Matsumura, M. Sato, A. Mineyama, T. Suzuki, and N. Hara, "Ultra-low phase noise 76-81 GHz PLL synthesizer for FMCW radar in 65 nm CMOS," in *Asia-Pacific Microwave Conference Proceedings (APMC)*, Dec 2012, pp. 649–651.

[Nan14] Nanotron, "nanoLOC," Sep 2014. [Online]. Available: http://www.nanotron.com/EN/PR_ic_modules.php

[NAV14] NAVSTAR, "Global Positioning System," Sep 2014. [Online]. Available: http://www.gps.gov/systems/gps/

[NFF+13] H. Ng, A. Fischer, R. Feger, R. Stuhlberger, L. Maurer, and A. Stelzer, "A DLL-Supported, Low Phase Noise Fractional-N PLL With a Wideband VCO and a Highly Linear Frequency Ramp Generator for FMCW Radars," *IEEE Transactions on Circuits and Systems I: Regular Papers*, vol. 60, no. 12, pp. 3289–3302, Dec 2013.

[PA04] H. Pan and A. Abidi, "Spectral spurs due to quantization in nyquist adcs," *IEEE Transactions on Circuits and Systems I: Regular Papers*, vol. 51, no. 8, pp. 1422–1439, Aug 2004.

[Raz11] B. Razavi, *RF Microelectronics*, ser. Prentice Hall Communications Engineering and Emerging Technologies. Prentice Hall PTR, 2011.

[RB74] D. Rife and R. Boorstyn, "Single tone parameter estimation from discrete-time observations," *IEEE Transactions on Information Theory*, vol. 20, no. 5, pp. 591–598, 1974.

[RCK93] T. Riley, M. Copeland, and T. Kwasniewski, "Delta-sigma modulation in fractional-N frequency synthesis," *IEEE Journal of Solid-State Circuits*, vol. 28, no. 5, pp. 553–559, May 1993.

[RDCR05] J. Rogers, F. Dai, M. Cavin, and D. Rahn, "A multiband $\Delta\Sigma$ fractional-N frequency synthesizer for a MIMO WLAN transceiver RFIC," *IEEE Journal of Solid-State Circuits*, vol. 40, no. 3, pp. 678–689, March 2005.

[Rol62] J. M. Rollett, “Stability and Power-Gain Invariants of Linear Twoports,” *IRE Transactions on Circuit Theory*, vol. 9, no. 1, pp. 29–32, 1962.

[San99] W. Sansen, “Distortion in elementary transistor circuits,” *IEEE Transactions on Circuits and Systems II: Analog and Digital Signal Processing*, vol. 46, no. 3, pp. 315–325, 1999.

[SE11] A. Strobel and F. Ellinger, “An active pulsed reflector circuit for FMCW radar application based on the switched injection-locked oscillator principle,” in *Semiconductor Conference Dresden (SCD)*, 2011, pp. 1–4.

[Sha49] C. Shannon, “Communication in the Presence of Noise,” *Proceedings of the IRE*, vol. 37, no. 1, pp. 10–21, 1949.

[SHL+11] J. Sun, L. Huang, H. Liu, D.-P. Chen, and F. Lin, “A 0.18 um mixer merged with LNA exploiting noise cancellation,” in *IEEE International Symposium on Radio-Frequency Integration Technology (RFIT)*, Nov 2011, pp. 25–28.

[SNK13] V. Sadeghi, H. Naimi, and M. Kennedy, “The Role of Charge Pump Mismatch in the Generation of Integer Boundary Spurs in Fractional-N Frequency Synthesizers: Why Worse Can Be Better,” *IEEE Transactions on Circuits and Systems II: Express Briefs*, vol. 60, no. 12, pp. 862–866, Dec 2013.

[SSJ+08] S. Scheiblhofer, S. Schuster, M. Jahn, R. Feger, and A. Stelzer, “Performance analysis of cooperative FMCW radar distance measurement systems,” in *IEEE MTT-S International Microwave Symposium Digest*, June 2008, pp. 121–124.

[STHW+11] Z. Stamenkovic, K. Tittelbach-Helmrich, M. Wickert, J. Ibanez, S. Ruiz, and G. Dimosthenous, “Implementation, integration, and verification of MIMAX WLAN modem,” in *6th International Workshop on Reconfigurable Communication-centric Systems-on-Chip (ReCoSoC)*, June 2011, pp. 1–8.

[Str13] A. Strobel, “Geschaltete Oszillatoren für Hochfrequenz-Entfernungsmesssysteme,” Dissertation, Technische Universität Dresden, 2013.

[Sym14] Symeo, “Positionierungssystem LPR-2D,” Sep 2014. [Online]. Available: http://www.symeo.com/Deutsch/Produkte/Positionsbestimmung/Produkte-Positionsbestimmung.html

[TKT+08] M. Tsuru, K. Kawakami, K. Tajima, K. Miyamoto, M. Nakane, K. Itoh, M. Miyazaki, and Y. Isota, "A Triple-Tuned Ultra-Wideband VCO," *IEEE Transactions on Microwave Theory and Techniques*, vol. 56, no. 2, pp. 346–354, feb. 2008.

[TLL08] C.-L. Ti, Y.-H. Liu, and T.-H. Lin, "A 2.4-GHz fractional-N PLL with a PFD/CP linearization and an improved CP circuit," in *IEEE International Symposium on Circuits and Systems (ISCAS)*, May 2008, pp. 1728–1731.

[TSG10] U. Tietze, C. Schenk, and E. Gamm, *Halbleiter-Schaltungstechnik*, 13th ed. Heidelberg: Springer, 2010.

[Ubi14] Ubisense, "RTLS Hardware," Sep 2014. [Online]. Available: http://de.ubisense.net/en/products-and-services/rtls-products.html

[VGC+10] D. Vassiliadis, A. Garbi, G. Calarco, M. Casoni, A. Paganelli, R. Morera, C.-M. Chen, and M. Wodczak, "Wireless networks at the service of effective first response work: The E-SPONDER vision," in *5th IEEE International Symposium on Wireless Pervasive Computing (ISWPC)*, may 2010, pp. 210 –214.

[VLH+12] M. Vidojkovic, Y.-H. Liu, X. Huang, K. Imamura, G. Dolmans, and H. de Groot, "A fully integrated 1.7-2.5GHz 1mW fractional-N PLL for WBAN and WSN applications," in *IEEE Radio Frequency Integrated Circuits Symposium (RFIC)*, June 2012, pp. 185–188.

[VWG+03] M. Vossiek, L. Wiebking, P. Gulden, J. Wieghardt, C. Hoffmann, and P. Heide, "Wireless local positioning," *IEEE Microwave Magazine*, vol. 4, no. 4, pp. 77–86, Dec 2003.

[Wal09] Walt Kester, "Analog Devices Tutorial MT-008," 2009.

[WGS11] Y. Weng, H. Gao, and L. Sun, "A 1.5-3.0GHz wideband VCO with low gain variation," in *IEEE Electrical Design of Advanced Packaging and Systems Symposium (EDAPS)*, dec. 2011, pp. 1–4.

[WiG14] WiGLE.net, "Wireless Geographic Logging Engine," Oct 2014. [Online]. Available: https://wigle.net/

[WLS09] W. Wu, J. Long, and R. Staszewski, “A digital ultra-fast acquisition linear frequency modulated PLL for mm-wave FMCW radars,” in *IEEE International Symposium on Radio-Frequency Integration Technology, RFIT 2009.*, Jan 2009, pp. 32–35.

[WME12] M. Wickert, U. Mayer, and F. Ellinger, “802.11a Compliant Spatial Diversity Receiver IC in 0.25um BiCMOS,” *IEEE Transactions on Microwave Theory and Techniques*, vol. 60, no. 4, pp. 1097–1104, April 2012.

[WWE12] M. Wickert, R. Wolf, and F. Ellinger, “Analysis of totem-pole drivers in SiGe for RF and wideband applications,” *International Journal of Microwave and Wireless Technologies*, vol. 4, no. 2, pp. 245–255, april 2012.

[Zig14] ZigPos, “eeRTLS Technology,” Sep 2014. [Online]. Available: http://www.zigpos.net/zigpos/

Publications

[AQEJE14*] B. Al-Qudsi, E. Edwan, N. Joram, and F. Ellinger, "INS/FMCW Radar Integrated Local Positioning System," in *Inertial Sensors and Systems - Symposium Gyro Technology*, 2014, p. on CD.

[CSK+13*] M. Casoni, D. Saladino, A. Karagiannis, D. Komnakos, S. Sagkriotis, J. Wagner, N. Joram, and F. Ellinger, "An Ad-hoc Emergency Network for Crisis Events," in *Future Network and Mobile Summit (FUNEMS)*, 2013, p. on CD.

[EBJ+14*] E. Edwan, M. Bourimi, N. Joram, B. Al-Qudsi, and F. Ellinger, "NFC/INS integrated navigation system: The promising combination for pedestrians' indoor navigation," in *International Symposium on Fundamentals of Electrical Engineering (ISFEE)*, Nov 2014, pp. 1–5.

[EJW+11*] R. Eickhoff, N. Joram, J. Wagner, A. Strobel, and F. Ellinger, "Design space exploration and hardware aspects of local positioning systems," in *8th Workshop on Positioning Navigation and Communication (WPNC)*, 2011, pp. 131–136.

[EMW+10*] F. Ellinger, U. Mayer, M. Wickert, N. Joram, J. Wagner, R. Eickhoff, I. Santamaria, C. Scheytt, and R. Kraemer, "Integrated Adjustable Phase Shifters," *IEEE Microwave Magazine*, vol. 11, no. 6, pp. 97–108, 2010.

[ESJE15*] M. El-Shennawy, N. Joram, and F. Ellinger, "Fractional-N PLL optimization for highly linear wideband chirp generation for FMCW radars," in *German Microwave Conference (GeMiC)*, March 2015, pp. 248–251.

[JAQW+13*] N. Joram, B. Al-Qudsi, J. Wagner, A. Strobel, and F. Ellinger, "Design of a multi-band FMCW radar module," in *10th Workshop on Positioning Navigation and Communication (WPNC)*, 2013, pp. 1–6.

[JBK+11a*] N. Joram, A. Barghouthi, C. Knochenhauer, F. Ellinger, and C. Scheytt, "Fully integrated 50 Gbit/s half-rate linear phase de-

tector in SiGe BiCMOS," in *IEEE MTT-S International Microwave Symposium Digest (MTT)*, 2011, pp. 1–1.

[JBK+11b*] N. Joram, A. Barghouthi, C. Knochenhauer, F. Ellinger, and C. Scheytt, "Logic framework for high-speed serial links in SiGe BiCMOS," in *Semiconductor Conference Dresden (SCD)*, 2011, pp. 1–4.

[JLWE14*] N. Joram, B. Lindner, J. Wagner, and F. Ellinger, "Integrated Multi-band Fractional-N PLL for FMCW Radar Systems at 2.4 and 5.8 GHz," in *10th Conference on Ph.D. Research in Microelectronics and Electronics (PRIME)*, 2014, p. on CD.

[JMEE09*] N. Joram, U. Mayer, R. Eickhoff, and F. Ellinger, "Fully integrated active CMOS vector modulator for 802.11a compliant diversity transceivers," in *IEEE International Conference on Microwaves, Communications, Antennas and Electronics Systems (COMCAS)*, 2009, pp. 1–4.

[JWE13a*] N. Joram, R. Wolf, and F. Ellinger, "A SiGe Wideband VCO and Divider MMIC with Low Gain Variation for Multi-band Systems at 2.4 and 5.8 GHz," in *9th Conference on Ph.D. Research in Microelectronics and Electronics (PRIME)*, 2013, p. on CD.

[JWE13b*] N. Joram, R. Wolf, and F. Ellinger, "Performance Evaluation of Broadband Drivers for Radio Frequency Applications," in *IEEE International Conference on Microwaves, Communications, Antennas and Electronics Systems (COMCAS)*, 2013, p. on CD.

[JWE14*] N. Joram, R. Wolf, and F. Ellinger, "High swing PLL charge pump with current mismatch reduction," *Electronics Letters*, vol. 50, no. 9, pp. 661–663, April 2014.

[JWLE14*] N. Joram, R. Wolf, B. Lindner, and F. Ellinger, "Concurrent 2.4 and 5.8 GHz Dual Band Power Amplifier for FMCW Radar Systems," in *IEEE International Symposium on Intelligent Signal Processing and Communication Systems*, 2014, p. on CD.

[JWSE12a*] N. Joram, J. Wagner, A. Strobel, and F. Ellinger, "5.8 GHz demonstration system for evaluation of FMCW ranging," in *9th Workshop on Positioning Navigation and Communication (WPNC)*, 2012, pp. 137–141.

[JWSE12b*] N. Joram, J. Wagner, A. Strobel, and F. Ellinger, "Distance Measurement and Time Synchronization using Frequency-Modulated Continuous Wave (FMCW) Radar," *Embedded Projects Journal (EPJ)*, no. 15, pp. 26–31, 2012.

[JWSE15*] N. Joram, J. Wagner, E. Sobotta, and F. Ellinger, "Fully Integrated Wideband sub-10 GHz Radio Frequency Front End with Active Matching," in *11th Conference on Ph.D. Research in Microelectronics and Electronics (PRIME)*, 2015, p. on CD.

[LJS+13*] B. Lindner, N. Joram, A. Strobel, U. Yodprasit, and F. Ellinger, "Broadband Receiver Frontend with High Dynamic Range for Multistandard Digital Radio," in *IEEE International Conference on Microwaves, Communications, Antennas and Electronics Systems (COMCAS)*, 2013, p. on CD.

[LWJ+14*] B. Lindner, J. Wagner, N. Joram, U. Yodprasit, and F. Ellinger, "Reconfigurable complex gm-c band-pass filter with high linearity for multi-standard radio receivers," in *International Symposium on Intelligent Signal Processing and Communication Systems (ISPACS)*, Dec 2014, pp. 287–290.

[RSJ+14*] A. Richter, A. Strobel, N. Joram, F. Ellinger, L. Göpfert, and R. Marg, "Tunable Interface for Piezoelectric Energy Harvesting," in *11th International Multi-Conference on Systems, Signals and Devices (SSD)*, 2014, p. on CD.

[SJE15*] M. Schulz, N. Joram, and F. Ellinger, "Design of a common-base Colpitts switched injection-locked oscillator at 2.45 GHz for a FMCW radar system," in *IEEE 16th Annual Wireless and Microwave Technology Conference (WAMICON)*, April 2015, pp. 1–5.

[SSJE14*] M. Schulz, A. Strobel, N. Joram, and F. Ellinger, "Design of a switched injection-locked oscillator at 2.45 GHz for a local positioning system," in *9th European Microwave Integrated Circuit Conference (EuMIC)*, Oct 2014, pp. 116–119.

[STG+14*] E. Sdongos, A. Tsertou, N. Georgakopoulos, K. Loupos, A. Amditis, N. Joram, F. Ellinger, B. Lindner, E. Edwan, A. Ehlerding, S. Camarinopoulos, V. Kallidromitis, D. Bairaktaris, E. Bairaktaris, J. Naundrup, N. Kerle, M. Gerke, K. Vierhuß-Schloms, and M. Markus, "A Novel and Practical Approach to Structural Health Monitoring - The RECONASS Vision / Local Positioning, Sensor

Networks, Secure Communications and Remote Sensing at the service of Structural Monitoring to Assess Construction Damage and Related Needs," in *IEEE Workshop on Environmental, Energy, and Structural Monitoring Systems (EESMS)*, 2014, p. on CD.

[WJAQ+14*] J. Wagner, N. Joram, B. Al-Qudsi, F. Ellinger, R. Gentsch, L. Caldani, R. Paradiso, K. Maliatsos, A. Marousis, A. Karagiannis, D. Karamitros, and A. Bartzas, "Sensor networks for the first responder of the future," in *11th Italian Networking Workshop*, 2014, p. online.

[WJWE15*] J. Wagner, N. Joram, R. Wolf, and F. Ellinger, "Broadband inductorless vector modulator IC for localisation and communication systems," *Electronics Letters*, vol. 51, no. 10, pp. 767–769, 2015.

[WMW+13*] J. Wagner, U. Mayer, M. Wickert, R. Wolf, N. Joram, A. Strobel, and F. Ellinger, "X-type Attenuator in CMOS with novel control linearization, very low phase variations and automatic matching," in *European Microwave Week*, 2013, p. on CD.

[WSJ+11*] J. Wagner, A. Strobel, N. Joram, R. Eickhoff, and F. Ellinger, "FMCW system aspects for multipath environments," in *8th Workshop on Positioning Navigation and Communication (WPNC)*, 2011, pp. 89–93.

[WWJE14*] J. Wagner, R. Wolf, N. Joram, and F. Ellinger, "0.5-9 GHz CMOS Variable Gain Amplifier with control linearization, low phase variations and self-matching," in *European Microwave Week*, 2014, p. on CD.

Definitions

The rectangular window function is defined as follows.

$$\operatorname{rect}(t) := \begin{cases} 1, & -\frac{1}{2} < t < \frac{1}{2} \\ \frac{1}{2}, & |t| = \frac{1}{2} \\ 0 & \text{otherwise} \end{cases} \tag{1}$$

The sinc function is defined as follows.

$$\operatorname{si}(t) := \frac{\sin t}{t} \tag{2}$$

The convolution of two functions f and g is defined as follows.

$$(f * g)(t) := \int_{-\infty}^{\infty} f(\tau) g(t - \tau) d\tau \tag{3}$$

List of Abbreviations

ADC	Analog-to-digital Converter
AGC	Automatic Gain Control
AoA	Angle Of Arrival
BJT	Bipolar Junction Transistor
BPF	Band-pass Filter
CRLB	Cramér-Rao Lower Bound
DAC	Digital-to-analog Converter
DDR	Double Data Rate
DDS	Direct Digital Synthesis
DFT	Discrete Fourier Transform
DUT	Device Under Test
ECL	Emitter-coupled Logic
EIRP	Equivalent Isotropically Radiated Power
ENR	Excess Noise Ratio
EOC	Emergency Operations Control Center
FFT	Fast Fourier Transform
FMCW	Frequency-modulated Continuous Wave
FPGA	Field-programmable Gate Array
FRU	First Responder Unit
FSK	Frequency Shift Keying
GPS	Global Positioning System
ISM	Industrial Science Medical
LNA	Low Noise Amplifier
LOS	Line Of Sight
LPS	Local Positioning System
MASH	Multi-stage Noise Shaping
MEOC	Mobile Emergency Operations Control Center
MIM	Metal Insulator Metal
MIMO	Multiple Input Multiple Output
PA	Power Amplifier
PCB	Printed Circuit Board
PFD	Phase Frequency Detector
PLL	Phase-locked Loop
PTAT	Proportional To Absolute Temperature
RF	Radio Frequency

RToF	Round Trip Time Of Flight
SDM	Sigma Delta Modulator
SFDR	Spurious Free Dynamic Range
SNR	Signal-to-noise Ratio
SPI	Serial Peripheral Interface
SRD	Short Range Device
TDoA	Time Difference Of Arrival
ToA	Time Of Arrival
ToF	Time Of Flight
USB	Universal Serial Bus
UWB	Ultra Wideband
VCO	Voltage-controlled Oscillator
VC-TCXO	Voltage-controlled Temperature-compensated Crystal Oscillator
VGA	Variable Gain Amplifier
WLAN	Wireless Local Area Network

List of Symbols

Symbol	Description
a	voltage gain
A	amplitude
B_{fm}	chirp bandwidth
c	propagation speed, in air $\approx 3 \cdot 10^8$ m/s
C	arbitrary capacitance
C_{par}	parasitic capacitance
C_{t}	parasitic transistor capacitance
C_{var}	varactor capacitance
C_{TP}	totem pole stage emitter capacitance
C_{∞}	blocking capacitance with large size
$\mathcal{C}$	cost function
d_0	distance to target
$\underline{d}_{\mathrm{B}}$	distances to base stations vector
d_{e}	distance or position measurement error
d_{m}	measured distance to target
$\underline{d}_{\mathrm{m}}$	measured distances vector
d_{refl}	distance of reflection path (non line-of-sight)
Δr	distance bin size
Δt	(synchronization) time offset
ΔR	range resolution
d	differential operator
$\delta(\cdot)$	Dirac delta function
$\frac{\partial}{\partial \cdot}$	first partial dervivative operator
$\frac{\partial^2}{\partial \cdot^2}$	second partial dervivative operator
e	Euler's number, ≈ 2.71828182845

$\varepsilon_{\mathrm{lin}}$	chirp linearity error
$\varepsilon_{K_{\mathrm{VCO}}}$	VCO gain error
f	arbitrary frequency
f_0	chirp starting frequency
f_{div}	PLL divider output frequency
f_{D}	base band beat frequency
f_{g}	cut-off frequency
f_{loop}	PLL loop bandwidth
f_{off}	offset frequency in phase noise measurements
f_{pre}	PLL prescaler frequency
f_{ref}	PLL reference frequency
f_{s}	sampling frequency
f_{RF}	PLL RF frequency
f_{T}	transit frequency
$f_{\mathrm{T,max}}$	maximum transit frequency
FSPL	free space path loss
F	noise factor
$\mathcal{F}\{\cdot\}$	Fourier transform operator
φ	arbitrary phase
φ_{m}	phase margin
g_{m}	transistor transconductance
G	arbitrary power gain
G_{T}	transducer gain
Γ	reflection coefficient
I	arbitrary current
I_{drv}	PA driver bias current
I_{filt}	PLL loop filter current
I_{CP}	charge pump current
$I_{\mathrm{C,op}}$	operating point current in PA
I_{PA}	PA output stage bias current
IM3	3rd order intermodulation ratio
$\mathrm{IP}_{\mathrm{1dB}}$	input-referred 1-dB compression point
$\mathrm{IIP}_{\mathrm{IM3}}$	input-referred 3rd order intermodulation intercept point
j	imaginary unit

J	jitter
$\mathcal{J}$	Fisher information
k	Boltzmann constant, $\approx 1.38065 \cdot 10^{-23}$ J/K
K	Rollett's stability factor
K_{VCO}	VCO gain
L_{b}	PA bias inductor
L_{φ}	phase noise single sideband spectrum
$\underline{m}$	vector of measured mobile position
μ	chirp gradient
μ'	chirp gradient in conjunction with angular frequency
NF	noise figure
NFFT	number of points for FFT
N_{B}	number of base stations
$\mathrm{OP}_{\mathrm{1dB}}$	output-referred 1-dB compression point
$\mathrm{OIP}_{\mathrm{IM3}}$	output-referred 3rd order intermodulation intercept point
ω	arbitrary angular frequency
ω_0	angular chirp starting frequency
ω_{g}	angular cut-off frequency
ω_{z}	zero point frequency
ω_{D}	angular base band beat frequency
P	arbitrary power
P_{nrx}	received noise power
P_{nq}	quantization noise power
P_{o}	PA output power
P_{rx}	received power
P_{tx}	transmitted power
P_{DC}	DC power consumption
PAE	power added efficiency
PSD	power spectral density
$\underline{r}$	vector of measured reference position
r	arbitrary small-signal resistance
r_{BE}	base emitter resistance

$\mathrm{rect}\,(\cdot)$	rectangle function in time domain
R	arbitrary resistance
$\mathrm{Rect}\,(\cdot)$	rectangle function in frequency domain
R_{L}	load resistance
R_{TP}	totem pole stage emitter resistor
$s(\cdot)$	arbitrary time-domain signal
$\mathrm{si}\,(\cdot)$	unnormalized cardinal sine function
$\mathrm{std}(\cdot)$	standard deviation operator
$S(\cdot)$	arbitrary frequency-domain signal
$\underline{S}_{\varphi}$	phase noise profile in dBc/Hz
SNR	arbitrary signal-to-noise ratio
SSR	signal-to-side lobe ratio
σ_{a}	accuracy
σ_{p}	precision
t_{FSK}	non-deterministic FSK transmit/receive delay
t_{upd}	update time
T_{fm}	chirp duration
T_{packet}	packet time slot for two-way synchronization
T_{pp}	pre and post chirp delay
T_{rx}	noise temperature of receiver
T_{s}	sampling rate
τ	time-of-flight from transmission to reception in reflective radar
$\tau_{\text{one-way}}$	time-of-flight from transmission to reception in one-way radar
θ	pseudo time of flight in two-way synchronization
$\mathrm{var}(\cdot)$	variance operator
V	arbitrary voltage
V_{c}	control voltage in AGC
V_{cas}	cascode bias voltage
V_{env}	envelope voltage in AGC
V_{filt}	charge pump output voltage in PLL
V_{i}	arbitrary input voltage
$V_{\mathrm{i,p}}$	input voltage at positive terminal in differential circuit
$V_{\mathrm{i,n}}$	input voltage at negative terminal in differential circuit
V_{o}	arbitrary output voltage

V_{sat}	generic saturation voltage (e.g. of a complete cascode circuit)
V_{tune}	VCO tuning voltage
V_{BE}	base emitter voltage
V_{CC}	supply voltage
$V_{\mathrm{CE,sat}}$	collector emitter saturation voltage
V_{TP}	totem pole stage bias voltage
x_{m}	measured x coordinate
y_{m}	measured y coordinate
$\underline{Y}_{\mathrm{R}}(s)$	admittance of a purely reactive one-port
z_{m}	measured z coordinate
$\underline{Z}_{\mathrm{opt}}(\cdot)$	optimum load impedance as function of a parameter (e.g. frequency)
$\underline{Z}_{\mathrm{R}}(s)$	impedance of a purely reactive one-port

List of Figures

List of Tables